Aging murine peritoneal macrophages undergo female-specific remodeling driven by hormone-dependent and independent mechanisms

Ryan J. Lu[1,2], Shiqi Chen[3], Minhoo Kim[1], Nirmal K. Sampathkumar[1,4], Evelyn H. Lee[1], Amy Christensen[1], Eric E. Wang[1,5], Isabella Y. Lau[1], Shivay Parihar[1,6], Charan K. Ravikumar[1,5], Jane Jung[1], Shelby Brown[1], Alan Xu[1,7], Julio L. Alvarenga[1], Kristen Mehalko[1], Changhan D. Lee[1,8], Helen S. Goodridge[9,10], Bérénice A. Benayoun[1,3,5,8,11,*]

[1] Leonard Davis School of Gerontology, University of Southern California, Los Angeles, CA 90089, USA.

[2] Graduate Program in the Biology of Aging, University of Southern California, Los Angeles, CA 90089, USA.

[3] Cancer Biology Department, USC Keck School of Medicine, Los Angeles, CA 90033, USA.

[4] Present address: Samsara Therapeutics, Headington, Oxford, OX3 8SB, UK.

[5] Molecular and Computational Biology Department, USC Dornsife College of Letters, Arts and Sciences, Los Angeles, CA 90089, USA.

[6]Graduate Program in Geroscience, University of Southern California, Los Angeles, CA 90089, USA.

[7]Thomas Lord Department of Computer Science, USC Viterbi School of Engineering, Los Angeles, CA 90089, USA.

[8] USC Norris Comprehensive Cancer Center, Epigenetics and Gene Regulation, Los Angeles, CA 90089, USA.

[9] Board of Governors Regenerative Medicine Institute, Cedars-Sinai Medical Center, 8700 Beverly Boulevard, Los Angeles, CA 90048, USA

[10]Research Division of Immunology in the Department of Biomedical Sciences, Cedars-Sinai Medical Center, 8700 Beverly Boulevard, Los Angeles, CA 90048, USA

[11]Pharmacology and Pharmaceutical Department, USC Mann School of Pharmacy, Los Angeles, CA 90033, USA.

* correspondence: berenice.benayoun@usc.edu

Abstract

Aging is a complex process characterized by a progressive decline in physiological functions driven by both biological and environmental factors, with notable differences between sexes. Immune function is strongly influenced by biological sex, affecting both innate and adaptive immune responses, including macrophage behavior. In this study, we investigated the effects of age and sex on the immune cell composition within the peritoneal cavity niche and identified macrophages as the most affected cell type. Macrophages, as central components of the innate immune system, play critical roles in maintaining tissue homeostasis and responding to infections. Here, we find that aging induces sex-specific remodeling of murine peritoneal macrophage transcriptomic and epigenomic landscapes. Consistently, peritoneal macrophages undergo sex-specific functional remodeling with aging (*i.e.* female-specific phagocytic decline and metabolic rewiring). Modulation of gonadal hormone signaling showed that changes in circulating estrogen levels likely contribute to aspects of female-specific macrophage age-related changes. Importantly, multi-omic analysis identified candidate transcription factors whose sex-specific age-regulated expression may drive aspects of sex-specific 'omic' remodeling with aging. Specifically, Irf2 downregulation in female macrophages recapitulates distinct transcriptomic and metabolic aspects of macrophage female aging phenotypes. These findings suggest that female-specific age-related functional remodeling arises through hormone-dependent and -independent mechanisms in peritoneal macrophages.

Introduction

Aging is a complex process characterized by a progressive decline in physiological functions, with notable differences between sexes[1]. This decline is driven by a combination of biological factors, and extrinsic factors[2]. Life expectancy of females are on average longer than males[3]. However, despite increased longevity, females tend to experience higher levels of comorbidities and disability than males (*i.e*. the mortality-morbidity paradox)[4-6]. Additionally, females face an elevated risk of developing age-related chronic conditions (*e.g*. coronary heart disease, osteoarthritis, Type 2 diabetes, neurodegenerative disorders)[7]. Chronic sterile inflammation, a mechanism dubbed "inflamm-aging", is a hallmark of aging and is associated to more general immune dysfunction or "immunosenescence"[8,9]. Despite well-documented sex-differences in aging and disease susceptibility, mechanisms driving sex-based aging disparities are poorly understood.

Immune function is heavily shaped by biological sex, influencing both innate and adaptive immune cells[10,11], including macrophages[12]. Females generally exhibit a more robust immune response compared to males (*e.g*. quicker pathogen clearance, higher antibody response, higher cytokine secretion, and less infection-related mortality)[10,11,13-15]. However, females are also more susceptible to autoimmune diseases[16]. During aging, hematopoietic stem cells (HSC) skew production toward myeloid cells (*e.g*. monocytes, neutrophils) at the expense of lymphoid cells (*e.g*. B- and T-cells), a shift more pronounced in males than females, thereby impacting leukemogenesis and hematopoiesis[17,18]. Importantly, lifelong sex differences in immune function can be shaped by differential 'omic' regulation in immune cell types[19-24]. Despite the potential significance of such sex-differences in immune aging, how biological sex shapes the impact of age on 'omic' and functional landscapes of innate immune cells is largely unexplored.

Macrophages are key components of the innate immune system, functioning as both regulatory and effector cells in maintaining tissue homeostasis and responding to infections. Tissue-resident macrophages (*e.g*. large peritoneal macrophages), which originate primarily from embryonic precursors, exhibit specialized, organ-specific functions shaped by the local microenvironment. In contrast, bone marrow-derived macrophages differentiate from circulating monocytes and typically adopt more pro-inflammatory phenotypes during immune responses[25,26]. Macrophages have a repertoire of functions: phagocytosis of pathogens and other foreign materials, clearance of dead/dying and senescent cells, chemotaxis and migration, and cytokine

production[27]. During aging, macrophages have been reported exhibit altered phagocytosis, metabolic changes, and cytokine secretion, leading to poor inflammation control[28-36]. In addition to age-related differences, sex-differences in young macrophages have also been reported[10], where young females exhibited greater phagocytic activity and more efficient antigen presentation[37,38]. Interestingly, microglia, the brain's resident macrophages, undergo a female-specific shift in glycolytic output with age dependent on C3a signaling[39]. While pioneering studies have started to unearth sex-differences in immune aging[40], systematic characterization of such sex-dimorphic phenotypes in aging macrophages and the molecular mechanisms driving them are still missing.

In this study, we employed an unbiased multi-omics approach to profile the transcriptome and epigenome of primary peritoneal macrophages in female *vs*. male mice with aging. Our analyses revealed that macrophages are regulated in a sex-dimorphic manner with aging, potentially influencing numerous macrophage functions. Indeed, single cell transcriptomic profiling of the peritoneal cavity revealed that aging and sex impact macrophages the most in this niche. Consistently, we identified divergent regulation of macrophage 'omic' landscapes using RNA-seq, ATAC-seq, and H3K4me3 CUT&RUN. These analyses revealed that aging significantly alters macrophage function, with distinct patterns observed across multiple parameters. Specifically, our analyses showed that aging macrophages follow sex-dimorphic trajectories, with key phenotypes related to 'omic' pathway changes—namely phagocytosis and metabolic wiring—exhibiting female-specific age-related remodeling. Our experiments suggest that female-specific age-related remodeling of peritoneal macrophages likely occurs through both gonadal hormone-dependent and independent mechanisms.

Results

Macrophages are the immune cell type most impacted by aging in the peritoneal cavity niche

The peritoneal cavity hosts a rich and accessible immune niche, housing B-cells, T-cells macrophages, neutrophils, and monocytes[41]. This immune niche is easily accessible through post-mortem peritoneal lavage[42,43], making it tractable for studies without the need for mechanical tissue dissociation (which compromises both cell viability and phenotypes[44]). We used this niche to better understand how biological sex may impact the mice aging immune system. Specifically, we obtained peritoneal lavage cells from young adult (4-5 months) and old (20-21 months) female and male C57BL/6JNia and C57BL/6J mice (**Figure 1A**). Isolated cells were used for unbiased profiling by single-cell RNA sequencing (scRNA-seq) using the 10xGenomics v2 and v3.1 3' platforms in 3 independent sets of aging mice (see **Methods**; **Figure 1A**).

We robustly identified expected cell types within this niche in our rich dataset: B-cells, macrophages, monocytes, natural killer (NK) cells, and T-cells (**Figure 1B**; 18,805 cells, 10,758 cells, and 14,595 cells for the NIA 10x v2, NIA 10x v3 and JAX datasets, respectively). To determine whether any of these cell types were especially impacted by age and/or sex, we leveraged Augur[45], an algorithm that helps prioritize cell types based on their transcriptional response to biological conditions using machine-learning (**Figure 1C**; **Supplementary Figure S1A-D**). Using Augur area under the curve (AUC) scores, we observed that the transcriptome of macrophages was the most impacted among peritoneal cell types in the combined dataset (0.632; **Supplementary Figure S1E**), as well as each individual dataset (≥ 0.567; **Supplementary Figure S1F-H**).

Another important aspect that can be inferred from scRNA-seq corresponds to relative cell type abundances, especially in the absence of potential dissociation artifacts. Thus, we asked if there were any age- or sex-related changes in the relative abundances of peritoneal cell types, using both sample-specific determination and scProportionTest[46] (**Figure 1D; Supplementary Figure S1I-L**). Interestingly, both methods revealed a significant increase in the relative proportion of B-cells and a significant decrease in the relative proportion of macrophages in the peritoneal cavity with aging, regardless of sex (**Figure 1D; Supplementary Figure S1I-L**), consistent with previous studies[47,48]. In addition, we also observed a male-specific increase in the

relative proportion of T-cells in the peritoneal niche with aging (**Figure 1D; Supplementary Figure S1I-L**). To independently validate these results *in vivo*, we used flow cytometry staining of peritoneal cells using cell surface markers $CD19^+$ (B-cells), $F4/80^+$ (macrophages), and $CD3^+$ (T-cells) (**Figure 1A, E**; **Supplementary Figure S1M**). We confirmed a relative increase in the proportion of B-cells and a relative decrease in the proportion of macrophages in the peritoneal cavity with aging, regardless of sex (**Figure 1E**). However, changes in relative T-cell abundance were not validated, potentially due to high animal-to-animal variability and/or a smaller effect size (**Figure 1E**). We then investigated whether changes in relative abundances of immune cells were accompanied by changes in absolute quantities. Interestingly, we observed that regardless of sex, there were increases of the total number of all 3 immune cell types within the peritoneal cavity with aging, with B-cell increases being most steep, especially in aging females (**Figure 1F**).

Tissue-resident peritoneal macrophages self-renew after acute inflammation[49,50]. Thus, we posited that compromised self-renewal properties may contribute to decreased macrophage proportions with age. For this purpose, we leveraged scRNA-seq data to predict macrophage cell cycle stage across samples, using Seurat 'CellCycleScoring'[51]. Intriguingly, the proportion of macrophages predicted to be in a resting non-cycling state (*i.e.* in G1 phase) was significantly reduced with aging (irrespective of sex), whereas that of macrophages predicted to be actively proliferating (*i.e.* in S, G2 or M phases) tended to increase (**Supplementary Figure S1N**). Our data suggests that despite reduced relative abundance, aged peritoneal macrophages may be in a more proliferative state. Thus, differences in macrophage proportions with aging are unlikely to stem from self-renewal defects. However, age-related changes in peritoneal cavity niche cellular makeup are likely to lead to functional remodeling of these cells.

Together, our analyses suggest that macrophages are most significantly impacted by aging and sex in the peritoneal cavity. Thus, we decided to focus on the peritoneal macrophage compartment to understand potential sex-dimorphic molecular and functional effects with aging.

Peritoneal macrophages show sex-dimorphic 'omic' phenotypes with aging

To better understand the impact of aging and sex on aging peritoneal macrophages, we leveraged a bulk multi-omic profiling approach using MACS-purified macrophages from young adults (4-5 months) and old (20-21 months) female and male C57BL/6JNia mice. We opted to

use a bulk approach due to its increased sensitivity and robustness, especially in the context of purified cells, compared to single cell level profiling. We profiled both transcriptional and epigenomic features, specifically (i) transcriptome profiling by bulk sequencing of ribosomal-RNA depleted RNA (RNA-seq), (ii) chromatin accessibility landscape through the Assay for Transposon-Accessible Chromatin followed by sequencing (ATAC-seq)[52,53], and (iii) promoter activity/priming using CUT&RUN profiling for the H3K4me3 histone post-translational modification[54] (**Figure 2A**). These 'omic' assays were each performed on an independent cohort of C57BL/6JNia animals (n = 5 animals per group; **Supplementary Table S1A**). After accounting for premature death before the experimental day (**Supplementary Table S1A**) and retaining only samples with > 90% macrophage purity (**Supplementary Figure S2A, B**), final sample numbers range from 3-5 per group and 'omic' layer.

We first leveraged Multi-Dimensional Scaling [MDS] to evaluate the main axes of separation of our samples across the 3 'omic' layers (**Figure 2B-D**). Interestingly, MDS revealed clear separation of samples by sex, regardless of age (**Figure 2B-D**). Thus, MDS analysis supports the existence of strong sex-dimorphism in the molecular aging landscape of primary peritoneal macrophages. Interestingly, we also observed a secondary separation of samples by age of the mice, albeit weaker than that by sex (**Figure 2B-D**). Thus, we investigated whether, in addition to baseline differences, aging may impact the 'omic' landscapes of peritoneal macrophage in a sex-dimorphic manner. For this purpose, we compared DESeq2 $\log_2$ fold changes in gene expression (**Figure 2E, Supplementary Figure S2C**), chromatin accessibility (**Figure 2F, Supplementary Figure S2D**) and H3K4me3 signal (**Figure 2G, Supplementary Figure S2E**) for every detected gene/peak in aging female *vs*. male peritoneal macrophages. We reasoned that high rank correlation values would correspond to largely colinear effects of aging on 'omic' landscapes regardless of sex, and that divergent aging trajectories would result in weaker rank correlation values. Using this method, we observed only relatively weak rank correlations between 'omic' aging trajectories of female and male peritoneal macrophages (Genome-wide Spearman Rho = 0.232-0.329; **Figure 2E-G, Supplementary Figure S2C-E**). To further investigate these divergent patterns, we next performed analyzed 'omic' changes with aging separately in females vs. males for each of the 'omic' layers. Specifically, we labelled genes with FDR < 5% in one sex but FDR > 10% in the other sex as significant in one sex only (sex-divergent regulation) and genes with FDR < 5% in both sexes as consistently regulated

(sex-independent regulation; **Supplementary Table S2A-C**). Importantly, although a core set of genes and peaks significantly changed similarly in both sexes with aging (respectively 61, 420 and 244; **Supplementary Figure S2C-E**), we identified many more genes and/or peaks with significant age-related changes in only one sex (respectively 284/234, 1044/2825 and 131/1699 [male-specific/female-specific]; **Figure 2E-M**). Together, these analyses are consistent with the notion of broadly divergent aging 'omic' trajectories in peritoneal macrophages as a function of biological sex.

Sex differences in aging may result from (i) downstream effects of sex hormone signaling (*e.g*. lifelong exposure to an estrogen- or androgen-rich milieu, or (ii) differential impact of sex chromosome karyotypes (*e.g*. XX vs. XY), including through X chromosome inactivation [XCI] escape[40]. Genes and/or peaks with sex-dimorphic aging regulation were distributed across the genome, indicating that autosomal gene dysregulation is a major feature of sex-dimorphism in the aging 'omic' landscapes of macrophages (**Supplementary Figure S2F-H**). To note, gene set enrichment analysis [GSEA] revealed a slight, but significant, trend for downregulation of X-linked genes in females (FDR = 1.4 $x10^{-2}$; **Supplementary Figure S2I**), consistent with a potential role of X chromosome dysregulation in aging female macrophages[55]. Consistently, we observed that one of the top female-specific regulated genes with aging in our bulk RNA-seq dataset was *Xist* (FDR = $5.4x10^{-5}$; **Supplementary Figure S2J**), which encodes a non-coding RNA critical to XCI initiation and maintenance[56,57]. A trend for increased *Xist* expression in peritoneal macrophages was also observed in our 10xGenomics v3.1 single cell RNA-seq datasets (**Supplementary Figure S2K**). Interestingly, upregulation of *Xist*[58] and increased XCI escape[58,59] have been observed across cell types with female brain aging. In contrast, we observed that known XCI escapees were significantly downregulated in aged female macrophages (FDR = $3.6x10^{-3}$; **Supplementary Figure S2I**), consistent with *Xist* upregulation but inconsistent with observations in the aging brain[58,59].

Together, our data reveals strong sex differences in the 'omic' landscapes of primary peritoneal macrophages throughout life and suggest that aging may differentially impact the function of these cells in female *vs*. male mice.

Functional enrichment analysis reveals sex-dimorphic regulation of key immune pathways with aging

We next asked whether sex-specific age-related changes in peritoneal macrophage gene expression regulation, at the transcriptomic and epigenomic levels, were expected to impact downstream functions using protein-protein interaction network construction and functional enrichment analyses (**Figure 3, Supplementary Figure S3; Supplementary Table S3**).

First, we generated predicted networks for female and male age-related changes using NetworkAnalyst 3.0[60] and protein-protein interaction [PPI] information from IMEx/InnateDB data[61], a knowledgebase geared towards innate immunity (**Figure 3A-B**). Our analysis revealed that genes regulated with aging in female vs. male macrophages are part of clear, interconnected PPI networks (**Figure 3A, B**). Interestingly, although some predicted nodes were identified in both sexes (Irf7, Il1r1), there was a majority of sex-specific nodes (*e.g*. Irf2 and Mef2c in females; Irf1 and Rela in males; **Figure 3A, B**). The tight gene interconnectivity within the female and male predicted PPI networks supports the notion that macrophage transcriptional changes with aging are coordinated within each sex, likely leading to differential aging related functional remodeling.

Next, we performed GSEA analysis using high quality gene sets from Gene Ontology (GO; all domains; ENSEMBL v108) and Reactome (MSigDB v2022.1) to evaluate differentially regulated processes in aging peritoneal macrophages at the levels of transcription, chromatin accessibility and H3K4me3 signal, both in a sex-independent (**Supplementary Figure S3A-F; Supplementary Table S3A-F**) and sex-dimorphic manner (**Figure 3C-E, Supplementary Figure S3G-I; Supplementary Table S3A-F**). Importantly, top gene sets that were regulated in a sex-independent manner were consistent with expected immune activation with aging (*e.g*. Gene ontology terms “innate immune response” or “immune system process”, Reactome gene sets “complement pathway” and “neutrophil degranulation”; **Supplementary Figure S3A-C; Supplementary Table S3A-F**). These observations are consistent with widespread observations of age-related immune remodeling or “inflamm-aging”[62], regardless of sex. In addition, we also observed strong sex-dimorphic regulation of GO and Reactome gene sets in aging peritoneal macrophages (**Figure 3C-E, Supplementary Figure S3G-I; Supplementary Table S3A-F**). Most notably, top significant sex-dimorphic aging gene sets revealed several phagocytosis-related gene sets (*e.g*. GO “phagocytosis, recognition”, “endosomes”, Reactome “cross-presentation of soluble exogenous antigens endosomes”), metabolism-related gene sets (*e.g*. GO “proton transmembrane transport”, “mitochondrial respiratory chain complex IV”, Reactome

"respiratory electron transport ATP synthesis by chemiosmotic coupling and heat production by uncoupling proteins") and inflammation-related gene sets (*e.g.* GO "positive regulation of cytokine production involved in inflammatory response", "arachidonic acid epoxygenase activity", Reactome "interleukin 2 family signaling", "defensins"; **Figure 3C-E, Supplementary Figure S3G-I; Supplementary Table S3A-F**).

Since these types of terms reflect potential changes in key pathways relating to macrophage function[63], we decided to complement our analysis using curated gene sets related to these functions to independently validate their sex-specific regulation in the transcriptome of aging peritoneal macrophages via GSEA (**Figure 3F-H, Supplementary Table S4**). Specifically, we (i) curated a list of phagocytosis regulator genes from two phagocytosis CRISPR/Cas9 screens[64,65], (ii) utilized curated lists of genes involved in oxidative phosphorylation and glycolysis from the MSigDB Hallmark gene sets[66], and (iii) identified genes involved in M1-like and M2-like polarization based on a publicly available macrophage RNA-seq dataset[67]. Consistent with our unbiased GO and Reactome GSEA analyses, we observed female-specific downregulation of phagocytosis regulators from CRISPR/Cas9 screens (**Figure 3F; Supplementary Table S2G**) and a male-specific upregulation of curated Hallmarks metabolism related pathways (**Figure 3G; Supplementary Table S2H**). In contrast, both female and male macrophages showed significant upregulation of M1-enriched genes, whereas only male macrophages showed significant upregulation of M2-enriched genes as well (**Figure 3H; Supplementary Table S2I**).

Together, our functional enrichment analyses suggest that several processes key to macrophage function may be regulated in a sex-specific manner: (i) phagocytosis capacity, which is required for pathogen and/or dead cell clearance[68,69], (ii) metabolic preference, which reflects macrophage inflammatory status — with greater reliance on glycolysis being associated to more pro-inflammatory macrophages[63] and (iii) macrophage polarization trends, whereby distinct pro- and anti-inflammatory programs are activated[70].

Peritoneal macrophages undergo female-specific age-related functional decline

Based on our 'omic' analyses (**Figure 3**), we hypothesized that peritoneal macrophages undergo sex-specific functional remodeling in phagocytosis capacity, metabolic preferences and

polarization state with age. Thus, we selected *ex-vivo* assays to evaluate these phenotypes using primary peritoneal macrophages from young and old, female and male mice (**Figure 4A**).

To evaluate potential sex-differences in macrophages phagocytic abilities, we used Alexa Fluor 488-Zymosan bioparticles as cargo to evaluate phagocytosis capacity as a function of age and sex. Specifically, we evaluated the "phagocytosis index", defined as the proportion of macrophages internalizing the labelled cargo in a set amount of time, using 2 complementary approaches based on (i) microscopy, after a day of *ex vivo* culture[71] and (ii) flow cytometry, on freshly isolated macrophages (**Supplementary Figure S4A**; see **Methods**). In line with computational predictions, we observed a significant reduction in phagocytosis capacity specifically in aged female peritoneal macrophages, as demonstrated by both microscopy (p-value = 2.0×10^{-2}; **Figure 4B, C**) and flow cytometry (p-value = 4.7×10^{-2}; **Figure 4D**). Importantly, we observed a consistent trend of decreased phagocytosis in aging female bone marrow-derived macrophages (BMDMs), a distinct primary macrophage population (p-value = 0.07; **Supplementary Figure S4B**), suggesting that female-specific phagocytic remodeling with aging is not niche-specific.

Within the peritoneal cavity, the peritoneal macrophage population can be comprised of both large peritoneal macrophages (LPM; expressing high levels of F4/80) and small peritoneal macrophages (SPM; expressing lower levels of F4/80)[72]. LPMs are the tissue-resident macrophages of the peritoneal cavity derived from the fetal yolk sac, and constitute the overwhelming majority of peritoneal macrophages in naïve mice[73-75]. In contrast, SPMs are constantly derived throughout life from blood monocytes, which are recruited to the peritoneal cavity in response to inflammatory signals, and represent a minority of peritoneal macrophages in naïve mice[50,75]. To rule out the possibility that female-specific changes in phagocytosis with aging could be trivial byproducts of LPM/SPM proportion shifts with aging, we analyzed F4/80 surface protein levels in MACS-purified peritoneal macrophages (**Supplementary Figure S4C-E**). Intriguingly, although there were no aging differences in LPM/SPM abundance for macrophages purified from C57BL/6JNia mice, shifts were observed in aged female C57BL/6J mice (**Supplementary Figure S4D, E**). Despite provider/substrain differences in LPM/SPM proportion with aging, female-specific phagocytosis decreases were observed consistently, ruling out the fact that shifts in macrophage subtypes is enough explain female-specific age-related remodeling (**Supplementary Figure S4D, E**). We also examined whether differential expression

of pattern recognition receptors involved in Zymosan recognition may explain decreased phagocytosis in aging females specifically. Zymosan is recognized by both Tlr2 and Dectin-1 (encoded by *Clec7a*)[76]. There was no evidence of differential regulation of Zymosan receptors *Tlr2* and *Clec7a* in our RNA-seq datasets (**Supplementary Figure S4F**). Using flow cytometry quantification, we observed no change in Tlr2 protein expression with aging or sex (**Supplementary Figure S4G, H**). Dectin-1 abundance showed a significant reduction during aging in female macrophages, although Dectin-1 levels in aged females matched those of males regardless of age (**Supplementary Figure S4G**), despite comparable phagocytosis in young animals (**Figure 4C**).

To identify potential mechanistic mediators of the specific phagocytosis phenotype in aged female macrophages, we compared female-specific aging downregulated genes (RNA-seq) with phagocytosis regulators from CRISPR/Cas9 phagocytosis screens[64,65] (**Figure 4E, Supplementary Table S4A-B**). This revealed 9 candidate genes mediating female-specific changes in phagocytosis with aging (6 at FDR < 5%: *B4galt1*, *Dpy19l3*, *Man1a2*, *Rps6ka3*, *Tbl1xr1*, and *Tm9sf3;* 3 at FDR < 10%: *Gna13*, *Hmgcs1*, *Magt1*; **Figure 4E**). To validate whether candidate regulators could indeed impact Zymosan phagocytosis in murine macrophages, we performed a mini lentiviral short hairpin RNA (shRNA)-mediated knockdown screen in RAW264.7 cells (**Figure 4F**; **Supplementary Figure S4I**). Interestingly, knockdown of *Rps6ka3* and *Magt1* resulted in significantly decreased Zymosan phagocytosis capability (**Figure 4G**), consistent with a potential mechanistic role in female-specific age-related decreased phagocytosis.

Next, we evaluated the metabolic preference of primary macrophages with aging and sex. Macrophage function in both homeostasis and disease conditions relies on metabolic reprogramming[77], whereby increased reliance on glycolysis is characteristic of pro-inflammatory states and increased preference of mitochondrial respiration is associated to tissue remodeling[63]. We took advantage of the Agilent Seahorse platform to metabolically phenotype primary macrophages[78]. Due to required yields for this method, we leveraged BMDMs to measure oxygen consumption rate [OCR] and extracellular acidification rate [ECAR], using a protocol designed to evaluate glycolytic and mitochondrial activity[78] (**Figure 4H-J, Supplementary Figure S4J, K**). Contrary to expectations from 'omic' analysis, no metabolic differences were observed in aging male BMDMs (**Figure 4I, J, Supplementary Figure S4J, K**). However, we

observed a significant increase in glycolytic activity specifically in aging female BMDMs (**Figure 4I, J**). We independently validated this phenotype in peritoneal macrophages using a luminescence-based assay with much lower cell number requirements. Consistent with our BMDM findings, we also observed a female-specific glycolytic shift in aging peritoneal macrophages (**Figure 4K**).

Finally, we set out to validate our 'omic' findings of sex-dimorphic activation of polarization pathways (**Figure 3H**) using flow cytometry quantification of cell surface markers known to be associated to M1-like (CD80, CD86) and M2-like (CD163, CD206) macrophage phenotypes[79-81]. We found that cell surface markers CD80 and CD86 increased with age in both sexes (**Supplementary Figure S4L**), indicating a general shift toward a more inflammatory phenotype with aging regardless of sex, consistent with previous studies in the field. In contrast, markers CD163 and CD206 showed inconsistent age-related changes; notably, CD206—but not CD163—significantly increased with age specifically in female macrophages (**Supplementary Figure S4M**).

Our functional validation analyses revealed robust female-specific age-related remodeling related to primary macrophage phagocytosis and metabolic preference.

Impact of ovarian hormone signaling on macrophage phenotypes with female-specific age-related remodeling

Our functional analyses revealed two phenotypes with strong female-specific age-related remodeling: (i) phagocytosis and (ii) glycolytic capacity. Notably, female mammals undergo drastic age-related decreases in ovarian hormones (*e.g.* estradiol, progesterone)[82]. In addition, previous work suggested that ovarian hormones may impact macrophage function, including phagocytosis[83,84] and metabolic reprogramming[85]. Hence, we asked whether the known age-related decrease in circulating ovarian hormones in female mice[82] may drive female-specific age-related peritoneal macrophages remodeling. Consistent with the ability to respond to variations in circulating sex hormones, our RNA-seq dataset showed that peritoneal macrophages express sex hormone receptors, with *Esr1* (encoding estrogen receptor a) being most robustly expressed (**Supplementary Figure S5A**). Therefore, we reasoned that decreased circulating levels of 17β-estradiol [E2] (the major form of estrogen in females) with age could drive female-specific macrophage remodeling.

We combined analyses of macrophages (i) from young females across the estrus cycle (experiencing endogenous changes in E2) and (ii) from young female ovariectomized [OVX] vs. sham control mice. First, we characterized cohorts of 4 month old C57BL/6NTac mice and identified animals actively cycling using vaginal cytology[86] to obtain peritoneal macrophages exposed to different endogenous levels of E2[87] (proestrus/estrus: high E2, metestrus/diestrus: low E2; **Supplementary Figure S5C; Supplementary Table S1B, C**). Interestingly, peritoneal macrophages isolated from females in low E2 phases of the estrus cycle showed significantly lower phagocytosis rates compared to those from females in high E2 phases (p-value = 1.3×10^{-2}; **Supplementary Figure S5D**). However, metabolic profiling of BMDMs from naturally cycling mice did not reveal E2-dependent differences in metabolic preference (**Supplementary Figure S5E, F**). We next used an OVX vs. sham surgery approach on young C57BL/6J females at 3 months of age and allowed the mice to recover for one month before euthanasia (**Figure 5A; Supplementary Table S1D**). We then evaluated 4 phenotypes: (i) peritoneal lavage composition, (ii) peritoneal macrophage transcriptomes, (iii) peritoneal macrophage phagocytosis, and (iv) peritoneal macrophage glycolytic activity (**Figure 5A**). Relative abundances and total quantities of peritoneal immune cell types were unaffected in OVX animals (**Supplementary Figure S5G**,**H**). However, the transcriptional landscape of peritoneal macrophages was strongly remodeled in OVX vs. sham animals (**Figure 5B;** samples with > 90% purity; **Supplementary Figure S5I; Supplementary Table S5A**). To evaluate whether OVX impacts macrophage transcriptomes similarly to aging, we next performed GSEA of genes differentially regulated upon OVX in macrophages (FDR < 5%) in the aging female peritoneal macrophage transcriptome (**Figure 5C**). Importantly, genes upregulated/downregulated upon OVX were significantly upregulated/downregulated in aging female macrophages (**Figure 5C**), showing that OVX mimics transcriptional effects of aging in female macrophages. We next evaluated the functional impact of OVX on peritoneal macrophages. Peritoneal macrophages from OVX mice had significantly decreased phagocytosis capacity when compared to sham mice (p-value = 2.2×10^{-3}; **Figure 5D**), similar to aging. However, lactate secretion (and by proxy glycolysis) was unaffected by OVX (**Figure 5E**). Together, our findings support the notion that lower levels of E2 are sufficient to recapitulate aspects of female macrophage aging (*i.e.* transcriptome, phagocytosis), but not others (*i.e.* metabolic preference).

Next, we reasoned that because decreased E2 conditions phenocopied aspects of female macrophage aging, supplementation of E2 in post-estropausal female mice may rescue aspects of aging. For this purpose, we treated 3 months and 19 months old female C57BL/6J mice with E2 (440ng/mL) or vehicle (*i.e.* ethanol 0.1%) in their drinking water[88,89] for one month before euthanasia (**Figure 5F; Supplementary Table S1E**). This method provides a minimally invasive framework for hormone supplementation, which still leads to robustly increased systemic E2 levels (with significant increase in uterine dry weight in aged E2-treated animals; p-value = 1.1×10^{-2} in Wilcoxon rank-sum test; **Supplementary Table S1E**). We then phenotyped the peritoneal cavity and purified peritoneal macrophages as above. While we observed expected age-related changes in B-cells and macrophages relative abundances, E2 supplementation did not significantly impact relative cell abundances nor overall cell numbers in the peritoneal cavity (**Supplementary Figure S5J,K**). Interestingly, the transcriptional landscape of peritoneal macrophages was strongly remodeled in response to aging and E2 supplementation (**Figure 5G**; samples with > 90% purity; **Supplementary Figure S5L; Supplementary Table S5B-C**). Interestingly, the transcriptomes of macrophages from E2-supplemented aged mice clustered in between those of young vehicle-treated mice and old vehicle-treated mice (**Figure 5G**), consistent with a "younger" transcriptomic signature. Indeed, GSEA using genes significantly regulated in response to E2 supplementation in old mice (FDR < 5%) on female macrophage aging transcriptomes revealed that genes upregulated in response to E2 were downregulated during aging, whereas genes downregulated in response to E2 were significantly during aging (**Figure 5H**), consistent with partial transcriptional rejuvenation. Next, we evaluated whether E2 supplementation would also functionally reprogram female macrophage toward a more youthful state. While we observed an expected age-related decrease in phagocytosis with vehicle treated animals (p-value = 1.9×10^{-2}), there was no significant rescue upon E2 supplementation (p-value = 0.56; **Figure 5I**). Glycolytic output, as measured by lactate production, was increased with aging as expected (p-value = 1.9×10^{-2}), but did not show significant changes upon E2 treatment (**Figure 5J**). Therefore, short-term post-estropausal *in vivo* E2 supplementation, while showing significant rescue of macrophage transcriptional aging markers, did not significantly rescue functional phenotypes. Since post-menopausal hormonal therapy has a limited window for efficacy in humans[90] and C57BL/6 mice undergo estropause between 12-15 months of age[91], it is

likely that short-term post-estropausal exposure cannot fully rescue the effects of age-related E2 loss.

Our results suggest that age-related decline in circulating E2 in females may explain aspects of female-specific macrophage aging. Since *Esr1* was the highest expressed receptor for E2 in our peritoneal macrophage bulk RNA-seq data (**Supplementary Figure S5A**), we next evaluated potential changes in expression or activity aging peritoneal macrophages. To note, there was a non-significant trend for increased *Esr1* expression in aging female (but not male) macrophages by bulk RNA-seq (p-value = 7.1×10^{-2}; **Supplementary Figure S5B**), consistent with the known negative feedback loop of Esr1 regulation[92]. *Esr1* expression levels were too low for robust detection in scRNA-seq (as expected for genes encoding transcription factors[93]). To determine whether Esr1 may mediate the impact of reduced E2 levels with aging in peritoneal macrophages, we leveraged existing *Esr1* full body knockout mice[94] (**Figure 5K**). We isolated and characterized cells from 3-4 months old *Esr1* knockout and wild-type littermate female mice, similarly as above (**Figure 5K; Supplementary Table S1F**). Interestingly, we found that *Esr1* knockout mice showed a significantly increased B-cell proportion (p-value = 4.1×10^{-2}) and a trend for decreased proportion of macrophages within the peritoneal cavity (p-value = 0.056; **Supplementary Figure S5M**), consistent with a prematurely aged immune phenotype. There was a change in the numbers of peritoneal macrophages, but not other cell types (p-value = 4.9×10^{-3}; **Supplementary Figure S5N**), which could stem from the impact of E2 on cell cycle in young macrophages[95]. Next, we evaluated the transcriptomic impact of constitutive *Esr1* knockout. Although *Esr1* knockout led to substantial transcriptional remodeling (**Figure 5L**; samples with > 90% purity; **Supplementary Figure S5O; Supplementary Table S5D**), GSEA analysis of *Esr1* knockout-regulated genes surprisingly showed a pattern consistent with transcriptional rejuvenation (**Figure 5M**). However, consistent with cycling and OVX functional results, *Esr1* knockout peritoneal macrophages exhibited significantly decreased ability to perform phagocytosis, as determined by flow-cytometry (p-value = 3.7×10^{-3}; **Figure 5N**), but showed no difference in glycolytic output (p-value = 0.23; **Figure 5O**).

Together, our results support the notion that sustained E2 exposure, at least in part through Esr1 signaling, is required to maintain youthful transcriptomic signatures and phagocytosis levels, but not low glycolytic dependence, in female peritoneal macrophages throughout life.

Identifying non hormonal mechanisms driving aspects of female-specific macrophage aging

Since decreased E2 signaling could only account for limited aspects of female-specific age-related remodeling in peritoneal macrophages (*i.e*. phagocytosis, transcriptome), we next sought to identify potential molecular mediators contributing to female-specific age-related macrophage remodeling. To do so, we leveraged our comprehensive 'omic' datasets (**Figure 1, 2**) as *in silico* screening tools to pinpoint candidate regulators (**Figure 6A; Supplementary Table S6B**). We prioritized genes encoding transcription factors [TFs], given their broad regulatory influence over the expression of hundreds to thousands of other genes[96].

First, we leveraged our bulk RNA-seq dataset to identify candidate TF-encoding genes that significantly changed in expression with aging in female, but not male, peritoneal macrophages (**Figure 6A; Supplementary Table S6B**). We then examined evidence for disrupted TF signaling specifically in aging female macrophages using: (i) TF binding motif analysis in ATAC-seq regions remodeled specifically in aging female macrophages and (ii) TF binding motif analysis in H3K4me3 CUT&RUN regions remodeled specifically in aging female macrophages (**Figure 6A; Supplementary Table S6B**). Mouse TF-encoding genes were obtained from the AnimalTFDB3.0 database[97] and overlapped to genes with significant age-regulation in females only, revealing 20 candidate TF-encoding genes (**Figure 6A, B; Supplementary Table S6B**). To note, 14 of these TFs were upregulated with age, and 6 of them were downregulated with age **(Figure 6A, B, Supplementary Figure S6A; Supplementary Table S6B**). We then performed TF motif analysis in the genomic regions with ATAC-seq and H3K4me3 CUT&RUN signal remodeled specifically in female macrophages with aging using HOMER[98]. Significantly enriched motifs in peaks with female-specific increased or reduced signals were then filtered based on correspondence with our 20 candidate TFs (**Figure 6C**,**D**), which led to the identification of 4 TF candidates with age-related <u>decreased</u> expression (*i.e. Irf2, Mef2C, Meis1, Tal1*), and 3 TF candidates with age-related <u>increased</u> expression (*i.e. Nr2f2, Sox7, Tead1*). For experimental simplicity, we focused on TFs specifically downregulated with aging in female macrophages (*i.e. Irf2, Mef2C, Meis1, Tal1*). Interestingly, all of these candidate TFs had also been identified as nodes of the predicted PPI network of aging female macrophages (**Figure 3A**), consistent with potentially central regulatory roles. In parallel, we leveraged our scRNA-seq datasets to predict differential TF activity across sex and ages in macrophage single

cell transcriptomes using SCENIC[99], which revealed significant predicted decrease in Irf2 activity and significant predicted increase in Mef2c activity in aging female macrophages (**Supplementary Figure S6B-C; Supplementary Table S6A**), providing another layer of evidence that age-related disruption of these TFs may impact female macrophages. Additionally, *Tbl1xr1*, a candidate phagocytosis regulator (**Figure 4F-G**) that functions as a transcriptional co-regulator[100], was also identified by SCENIC as showing significant age-related predicted activity decrease (**Supplementary Figure S6B, C; Supplementary Table S6A**). In analyses thereafter, we considered a set of 4 TFs and 1 TF co-regulator (*i.e. Irf2, Mef2c, Meis1, Tal1, Tbl1xr1*; hereafter referred to as "TFs") as candidate regulators of female macrophage aging (**Figure 6A; Supplementary Table S6B**). The impact of candidate TFs on macrophage phenotypes (*i.e.* transcriptome, phagocytic capacity, metabolic preference) was evaluated using RAW264.7 macrophages using a mini lentiviral shRNA knockdown screen (**Figure 6F**; **Supplementary Figure S6D;** see **Methods**).

We first analyzed the impact of decreased TF expression on macrophage transcriptomes by mRNA-seq (**Supplementary Figure S6E-G**), which revealed that TF knockdown led to clear remodeling of macrophage transcriptomes (**Supplementary Figure S6F**,**G; Supplementary Table S6C-G**). Robust/consistent transcriptional targets of candidate TFs were then used as gene sets for GSEA to evaluate whether transcriptional changes elicited by decreased TF expression were consistent with female macrophage aging (**Figure 6G**). Interestingly, knockdown of *Irf2* and *Tal1* showed patterns colinear with female macrophage aging, with upregulated genes being significantly upregulated (and downregulated genes being downregulated) in aging female macrophages. Importantly, *Irf2* targets showed substantially stronger colinearity than those of *Tal1* (**Figure 6G**). In the case of *Mef2c* and *Meis1* knockdown, downregulated genes showed strong downregulation in aging female macrophages, whereas upregulated genes showed weak downregulation opposite of aging (**Figure 6G**). *Tbl1xr1* knockdown led to transcriptional changes in macrophages inconsistent with aging (**Figure 6G**). Intriguingly, when investigating whether candidate TFs may belong to a regulatory network of their own, we observed that *Mef2c* knockdown led to significantly reduced *Irf2* expression (**Supplementary Figure S6H, I**), suggesting that concomitant downregulation of *Irf2* and *Mef2c* may act synergistically to shape the female aging peritoneal macrophage transcriptome.

We next evaluated whether decreased expression of candidate TFs may recapitulate female-specific age-related macrophage functional remodeling in phagocytosis and metabolic preferences (**Figure 6H-J**). We observed no significant recapitulation of age-related phagocytosis decreases in response to TF knockdown, with the notable exception of *Meis1* (**Figure 6H**). Interestingly, *Rps6ka3*, the top hit from our mini-shRNA knockdown screen for candidate regulators of phagocytosis is significantly downregulated after *Meis1* knockdown (FDR = 0.004; **Supplementary Figure S6J; Supplementary Table S6E**), supporting the notion that *Meis1* downregulation in aged female macrophages occurs upstream of *Rps6ka3* downregulation to promote reduced phagocytosis. In contrast to phagocytosis, using both the Agilent Seahorse and Promega Lactate-Glo assays, there was a widespread impact of TF candidate knockdown on glycolytic output (**Figure 6I, J**). Specifically, knockdown of *Irf2*, *Tal1*, and *Tb11xr1* led to significantly increased macrophage glycolytic activity in both assays, consistent with the female aging macrophage phenotype (**Figure 6I, J**).

Thus, our mini-shRNA screen showed that downregulation of *Irf2* led to the strongest (i) transcriptional and (ii) metabolic remodeling consistent with female macrophage aging. Consequently, its age-related downregulation represents the best candidate mechanism to explain observations of female-specific glycolytic shift in aging macrophages, which could not be explained by age-related estrogen deprivation (**Figure 5, Supplementary Figure S5**).

Age-related downregulation of Irf2 expression may promote female macrophage metabolic reprogramming by lifting *Hk3* transcriptional repression

To note, *Irf2* transcriptional levels, as assessed by RNA-seq, was unaffected by ovarian hormone signaling, with no significant change in expression in response to OVX (DESeq2 FDR = 0.69; **Figure S7A upper panel**), late-life E2 supplementation (DESeq2 FDR = 1; **Figure S7A middle panel**) or *Esr1* knock-out (DESeq2 FDR = 0.91; **Figure S7A lower panel**), consistent with *Irf2* downregulation occurring independently of estrogen signaling and/or ovarian aging.

We next set out to independently validate Irf2 regulation at the RNA and protein levels in aging primary peritoneal macrophages (**Figure 7A-D**, **Supplementary Figure S7A-C**). RT-qPCR analysis of *Irf2* RNA expression in peritoneal macrophages from independent aging mouse cohorts confirmed significant transcriptional downregulation of *Irf2* with aging, albeit in both sexes (**Figure 7B**). Next, we asked whether protein levels of Irf2 were impacted in aging

peritoneal macrophages using intracellular immunolabeling and quantification by flow cytometry (**Figure 7C-D**; **Supplementary Figure S7B-C**). Consistent with our predictions, we observed a significant decrease in Irf2 protein levels in peritoneal macrophages with aging in female (but not male) maice (**Figure 7D**). Importantly, Irf2 labeling was specific, as RAW264.7 and J774.1 macrophages expressing *Irf2* shRNAs showed decreased labeling (**Supplementary Figure S7D, E**). Thus, Irf2 is downregulated in aging female peritoneal macrophages at the transcriptional and protein levels.

To better understand the impact of Irf2 in young female macrophages (and thus the impact of decreased expression with aging), we evaluated the Irf2 chromatin binding landscape in primary female macrophages from young female C57BL/6JNia mice (**Figure 7E**). To note, since TF ChIP-seq profiling requires 10 million cells, we leveraged abundant BMDMs to map the Irf2 macrophage regulome. We identified 339 robust ChIP-seq peaks across 2 biological replicates, which showed expected significant enrichment for DNA binding motifs recognized by interferon regulatory factors (IRFs; **Supplementary Figure S7F; Supplementary Table S7A,B**). Irf2-bound regions were mostly found near promoters (≤ 3kb from annotated transcription start sites [TSSs]) and distal intergenic regions (likely enhancers; **Supplementary Figure S7G**). To gain insights about the regulatory network of Irf2 in primary macrophages, we leveraged the Genomic Regions Enrichment of Annotations Tool (GREAT)[101], which revealed enrichments of GO terms related to immune response and metabolism (*e.g*, GO:0006955 "immune response", GO:0003950 "NAD+ ADP-ribosyltransferase activity"; **Figure 7F**; **Supplementary Table S7C, D**). Similar enrichments were observed when using the gene-centric ChIPseeker tool[102] (*e.g*, GO:0045088 "regulation of innate immune response", GO:0046320 "regulation of fatty acid oxidation"; **Supplementary Table S7E, F**).

We next investigated how Irf2 *bona fide* target genes were regulated with aging at the transcriptional and epigenomic levels. Importantly, GSEA revealed that Irf2 <u>direct</u> targets (regardless of distance to TSSs) were significantly upregulated in aging female macrophages (**Supplementary Figure S7H**), consistent with its primary role as a transcriptional repressor[103,104]. Notably, even with a less sensitive overlap-based approach, the majority of direct Irf2 targets overlapping with genes significantly regulated in aging female macrophages (FDR < 5%) were upregulated (**Supplementary Figure S7H**). Interestingly, 3 of the upregulated genes in this overlap, *Tm6sf1*, *Usp18*, and *Ifit3*, have been previously reported to be linked to cell

metabolism[105-107]. Consistent with increased activation of Irf2 targets in aging female peritoneal macrophages, Irf2-bound chromatin regions showed slightly increased chromatin accessibility by ATAC-seq (**Supplementary Figure S7I-J,** left panel) and H3K4me3 CUT&RUN signal (**Supplementary Figure S7I-J**, right panel). Together, these results support the notion that decreased Irf2 expression with aging leads to reactivation of its target gene network.

Next, we manually inspected the list of Irf2 *bona fide* direct targets to gain further insights into how Irf2 downregulation impacts aging female macrophages (**Supplementary Table S7A**). Intriguingly, there was robust Irf2 binding in the promoter of the *Hk3* gene, which encodes an isoform of hexokinase – the enzyme that catalyzes the initial rate-limiting step of glycolysis (**Figure 7H**). There was a trend for increased *Hk3* expression with aging in our peritoneal macrophage RNA-seq dataset, likely non-significant due to an outlier value in the young female group (**Supplementary Figure S7K**). However, RT-qPCR analysis of peritoneal macrophages from 3 independent cohorts of animals revealed a significant increase in *Hk3* RNA levels (p-value = $1.6x10^{-2}$; **Figure 7I**). Thus, age-related downregulation of Irf2 in female peritoneal macrophages likely leads to *Hk3* upregulation and increased glycolytic activity.

To complement mechanistic insights downstream of Irf2 downregulation from our screen in RAW264.7 macrophages (**Figure 6**), we performed shRNA knockdown in J774A.1 macrophages (**Figure 7J, Supplementary Figure S7L-N**). There was good agreement in the transcriptional remodeling following *Irf2* knockdown across both macrophage cell lines as measured by mRNAseq (**Supplementary Figure S7L, M; Supplementary Table S6G**). Consistent our RAW264.7 screen results, *Irf2* knockdown did not impact phagocytic capacity in J774A.1 macrophages (p-value = 0.51; **Supplementary Figure S7N**). In contrast, as expected from the status of *Hk3* as a strong direct target of Irf2 and observations in female aging macrophages, *Irf2* knockdown led to robust *Hk3* transcriptional upregulation in both macrophage lines according to RNA-seq (RAW264.7 p-value = $2.6x10^{-37}$; J774A.1 p-value = $3.9x10^{-9}$; **Figure 7K**). Consistent with *Hk3* expression acting as a limiting factor for glycolytic potential of macrophages, *Hk3* upregulation was accompanied by significantly increased glycolytic activity both RAW264.7 (p-value = $1.2x10^{-3}$, $7.3x10^{-3}$ respectively) and J774A.1 macrophages (p-value = $1.7x10^{-3}$, $2.6x10^{-2}$ respectively; **Figure 6I-J, 7L-M**).

Together, our data suggests that decreased *Irf2* expression with aging in female peritoneal macrophages leads to an upregulation of *Hk3*, which then leads to an aberrant age-related increase in glycolytic output (**Figure 7N**).

Discussion

A multi-omic resource to study murine tissue-resident macrophages as a function of age and biological sex.

To understand how sex may influence aging of the immune system, specifically macrophages, we generated a multi-omic resource focusing on primary resident peritoneal macrophages from young and old, female and male C57BL/6J[Nia] mice, with high quality transcriptomic (single-cell and bulk RNA-seq) and epigenomic (chromatin accessibility by ATAC-seq and H3K4me3 genomic distribution by CUT&RUN) maps. To our knowledge, our dataset is the largest multi-omic dataset for the study of primary macrophages during aging, and we believe it will be a rich resource to the scientific community in understanding the influence of biological sex on age-related immune remodeling. Analysis of these datasets revealed that, not only is there a baseline difference in genomic regulation of primary macrophages at young age, but also that aging differentially impacts 'omic' profiles in female *vs*. male animals. Specifically, although there were shared features of molecular aging in female and male macrophages, we observed much larger sex-dimorphic age-related changes in gene expression and chromatin organization (**Figure 2; Supplementary Figure S2**).

Importantly, genes and genomic regions showing age-related sex-dimorphic regulation were enriched for processes key to macrophage function, including phagocytosis regulation, metabolic wiring and inflammatory phenotypes (**Figure 3; Supplementary Figure S3**). Although aging phenotypes of macrophages across various niches have been reported (*e.g*. visceral adipose macrophages, alveolar macrophages, Kupffer cells, *etc*.), previous studies largely focused on using animals of one sex, or mostly reported results combining sexes (reviewed in[36]). A notable exception includes a series of recent studies on aging murine microglia, the brain resident macrophage, which also reported large sex-differences in molecular landscapes with aging[39,108].

Peritoneal macrophages show female-specific age-related remodeling in phagocytosis and metabolic wiring.

To determine whether sex-differential regulation of molecular landscapes with aging yielded functional consequences, we assessed phagocytic capacity, metabolic preference, and polarization surface markers in isolated peritoneal macrophages (**Figure 4; Supplementary**

Figure S4). Intriguingly, this revealed two significant female-specific age-related remodeling in primary peritoneal macrophages: (i) a decrease in phagocytic capacity, and (ii) a metabolic shift to increased glycolytic output. Different populations of tissue-resident macrophages have previously been observed to show age-related decreases in phagocytosis across a range of cargo types, but with no insights on the potential influence of sex on these phenotypes[36]. Our data suggests that age-related remodeling in macrophage functions is sex-dimorphic.

To understand the molecular mechanism driving female-specific regulation of phagocytosis, we tested candidate regulator genes of phagocytosis from CRISPR/Cas9 screens that were specifically downregulated in aged female macrophages through a mini shRNA knockdown screen (**Figure 4G**). Our results identified two phagocytosis regulators (*Magt1* and *Rps6ka3*) whose knockdown mimicked the age-related decrease in phagocytosis of female macrophages, consistent with the notion that their downregulation with aging may explain mechanistically our observed female-specific age-related decrease in macrophage phagocytic capacity. Although its impact during aging has not been evaluated before, *Magt1* is a Magnesium transporter located to the endoplasmic reticulum involved in protein glycosylation with critical function in immune cells[109,110], which was identified as required for proper phagocytosis of Zymosan in a whole genome CRISPR/Cas9 screen of human phagocytes[64]. Interestingly, *Rps6ka3* encodes a member of the S6 kinase family, whose activity is regulated by mTOR[111], which is a key regulator of aging[112], autophagy[113], phagosome maturation[114], and macrophage polarization[115]. *Rps6ka3* was also shown to play a direct role in innate immune responses[116] and was found to be required for phagocytosis of Zymosan in human phagocytes[64]. Thus, downregulation of *Magt1* and *Rps6ka3* in aging female peritoneal macrophages is likely to mechanistically underlie the female-specific age-related phagocytosis defect that we observed.

Interestingly, despite 'omic'-based predictions of male specific metabolic rewiring, we identified a metabolic shift specifically in aging female macrophages (both peritoneal macrophages and BMDMs), leading to increased glycolytic output. Increased glycolytic output is known to support inflammatory phenotypes and ROS-production in macrophages and is a characteristic of disease-associated macrophages[117]. Furthermore, a recent study of aging murine microglia also identified a female-specific increase in glycolytic output, which was driven by increased C3a – C3aR signaling[39]. Thus, our observations are consistent with a potential shift to a more dysfunctional state in female macrophages with aging.

Sustained estrogen signaling is necessary for youthful macrophage phagocytosis.

Since the age-related functional remodeling we uncovered were female specific, we reasoned age-related decreases in circulating ovarian hormones may explain these phenotypes (**Figure 5; Supplementary Figure S5**). Indeed, previous work found that E2 signaling can shape macrophage phenotypes[83,84]. Importantly, decreased exposure to youthful E2 levels by ovariectomy recapitulated aspects of female-specific macrophage aging, including transcriptional remodeling and decreased phagocytosis, but had no impact on glycolytic output of female macrophages (**Figure 5C-F**). Similar functional outcomes were observed in macrophages from mice lacking estrogen receptor gene *Esr1*, the most abundantly expressed estrogen receptor in peritoneal macrophages, suggesting the functional impact of youthful E2 may be mediated through ERa (**Figure 5Q-R**). In contrast, late-life short-term E2 *in vivo* supplementation partially rejuvenated the transcriptional landscape of peritoneal macrophages (**Figure 5I-J**), although there was no significant rescue of the phagocytic or metabolic remodeling (**Figure 5K-L**). Accumulating data has shown that delayed onset of hormone therapy in post-menopausal women leads to decreased efficacy (or even increased risk of adverse side effects)[118-120], suggesting that late-life supplementation, months after the onset of estropause (9-12 months of age in C57BL/6 mice)[121], is likely too late to observe substantial rescue of female-specific age-related macrophage functional remodeling. Thus, our results suggest that youthful E2 levels are necessary (although not sufficient) to maintain (i) aspects of the youthful female macrophage transcriptome, and (ii) youthful phagocytosis capacity in peritoneal macrophages. However, youthful E2 exposures had no influence on glycolytic output, suggesting that the female-specific metabolic shift of peritoneal macrophages occurs independent of circulating levels of sex hormones. Future work should determine whether hormone treatment initiated earlier in life, closer to estropause onset, will lead to at least partial functional rescue of aging female macrophage phenotypes.

TF-encoding genes are involved in female-specific age-related macrophage phenotypes.

We also identified a set of putative TF encoding genes that were specifically downregulated in aging female macrophages and may shape female-specific aging phenotypic remodeling: *Irf2*, *Mef2c*, *Meis1*, *Tal1*, and *Tbl1xr1* (**Figure 6**; **Supplementary Figure S6**).

Interestingly, with the exception of *Tbl1xr1*, knockdown of candidate TF genes recapitulated phenotypic aspects of aging female macrophages, with *Irf2* and *Tal1* knockdown most closely resembling the effect of aging on macrophage transcriptomes (**Figure 6G**). Among candidates, only knockdown of *Meis1* led to aged-like decreased phagocytic capacity, likely due to downregulation of phagocytosis regulator *Rps6ka3*. To note, *Meis1* expression is unaffected in macrophages from OVX mice or in response to late-life short term E2 supplementation (**Supplementary Table S5A, C**), suggesting that its impacy on phagocytosis occurs independently of E2 signaling. In contrast, knockdown of *Irf2*, *Tal1*, and *Tbl1xr1* promoted increased glycolytic output, suggesting that their age-related expression downregulation may underlie the female-specific glycolytic shift we observed in female peritoneal macrophages. How age-related decreased expression of these TFs in female macrophages may synergize together (and with decreased E2 signaling) to shape female-specific aging phenotypes is an interesting avenue for future studies.

Female-specific age-related downregulation of Irf2 leads to increased *Hk3* expression and glycolytic output.

Since *Irf2* knockdown best mimicked the aging female macrophage transcriptome and led to the strongest increase in glycolytic output, we focused on elucidating how it may drive aspects of female-specific peritoneal macrophage phenotypes (**Figure 7**; **Supplementary Figure S7**). Interestingly, Irf2 shares a similar DNA binding domain as Irf1, but works as a competitive antagonist of Irf1-mediated gene expression[122]. Consistent with decreased Irf2 activity driving aspects of aging female macrophage molecular landscapes, ChIP-seq analysis revealed that *bona fide* Irf2 target genes in primary macrophages were significantly upregulated and overlapped with remodeled chromatin regions in aging female macrophages. Most notably, ChIP-seq identified a strong region of Irf2 binding in the promoter of *Hk3* (the gene encoding Hexokinase 3). Both female macrophage aging and *Irf2* knockdown led to significant upregulation of *Hk3*, suggesting that decreased *Irf2* expression with aging is responsible for increased *Hk3* expression. Importantly, hexokinases catalyze the rate-limiting first step of glycolysis (the phosphorylation of glucose on C6)[123], thus gatekeeping cellular glycolytic potential. Thus, our data suggests that the female-specific increase in glycolytic output during peritoneal macrophage aging is driven by downregulation of *Irf2* and derepression of downstream target *Hk3*. Interestingly, this

mechanism that we identified in peritoneal macrophages is distinct from the one previously reported in microglia[39], suggesting that metabolic rewiring of female macrophages is driven by niche-specific mechanisms.

Together, our study provides the first systematic characterization of sex-differences in immune aging in the context of macrophages and provides mechanistic insights into how sex-specific aging phenotypes can be achieved. Intriguingly, our data suggests that both mechanisms involving age-related changes in gonadal hormone levels and mechanisms independent of gonadal hormones can drive sex-dimorphism in the aging trajectories of immune cells. Ultimately, such mechanisms could be leveraged as potential targets to rejuvenate immune responses in a sex-specific manner, the first and easy step towards personalized geroscience.

Material and Methods

Mouse husbandry

All animals were treated and housed in accordance with the Guide for Care and Use of Laboratory Animals. All experimental procedures were approved by the University of Southern California's Institutional Animal Care and Use Committee (IACUC) in accordance with institutional and national guidelines. Experiments described in this manuscript were performed on approved IACUC protocols 20770, 20804, 21004 and 21454. All animals were euthanized between 8-11 am using a "snaking order" to minimize batch-processing confounding factors related to circadian effects and post-mortem interval, by using by CO_2 asphyxiation followed by cervical dislocation.

For intact aging analyses, male and female C57BL/6JNia mice were obtained from the National Institute on Aging (NIA) colony at Charles Rivers, or male and female C57BL/6J mice were obtained from the Jackson Laboratories (3 and 19 months, acclimated at USC for 4-6 weeks) **(Supplementary Table S1A).**

For estrus cycle tracking experiments male and female C57BL/6NTac were obtained from Taconic Biosciences (3 months, acclimated at USC for 2 weeks; **Supplementary Table S1B**). The cycle stage of adult female mice was characterized by vaginal lavage daily for 3 weeks until euthanasia on 3-4 months old mice. Mice that seen at least a full cycle or seen of the different phases during the three weeks of vaginal smear were taken for euthanasia (**Supplementary Table S1C**). To reduce animal waste, non-cycling mice were housed with a mixture of clean and used male bedding to elicit additional cycle to stimulate cycling. Mice were cycled for another two weeks and mice that were cycling were taken for euthanasia.

For ovariectomy (OVX) *vs*. sham surgery experiments, female C57BL/6J mice were obtained from Jackson Laboratories (8 weeks old animals, acclimated at USC for 4 weeks) (**Supplementary Table S1D**). C57BL6/J female mice gone through sham or OVX surgery at 12 weeks of age. All surgery procedures and post-operative care were conducted by University of Southern California Department of Animal Resources veterinarians and veterinarian technicians. Surgery entry point was from the back to preserve the peritoneal cavity as much as possible for post-mortem peritoneal cell collection. Mice went through a recovery period of 4 to 5 weeks before euthanasia.

For late-life short-term E2 supplementation experiments, female C57BL/6J mice were obtained from Jackson Laboratories at age 10 and 80 weeks and acclimated at USC for 2 weeks before treatment initiation (**Supplementary Table S1E**). For supplementation, 17β-estradiol (E2) was used in the purest chemical grade that could be obtained (≥98% purity; Sigma-Aldrich #E8875). We generated our E2 stock solution of 5 ng/mL in pure 100% ethanol (Sigma-Aldrich #E7023). E2 stock solution and 100% ethanol were filtered sterilized on 0.22μm PES filters (VWR #76479-024) and stored at -20°C for no longer than 1 month. Drinking water of C57BL6/J mice was supplemented with either vehicle (0.1% EtOH) or 440 ng/mL of E2 for 4 weeks, corresponding to ~94μg/kg of body weight/day[88,89]. Treatment water was changed every 2-3 days (3 times a week) to maximize treatment potency and limit potential E2 degradation. Water levels and mice were monitored daily. Water supplementation of E2 in this manner was found to be a safe and effective alternative to daily injections[88,89,124]. Mice were euthanized ~4 weeks after treatment initiation for experimental phenotyping.

For B6N(Cg)-*Esr1*$^{tm4.2Ksk}$/J [*Esr1* KO][94] (JAX #026176) experiments, matched female knockout [KO] and wild-type [WT] littermates were obtained from Jackson Laboratories (**Supplementary Table S1F**). After receiving mice at USC, *Esr1* KO/WT mice were acclimated and aged at USC until they reached 12-16 weeks before euthanasia.

Charles Rivers, Jackson Laboratories, and Taconic Biosciences have specific-pathogen-free (SPF) facilities. All animals were acclimated at the SPF animal facility at USC for >2 weeks before any processing or intervention to minimize the impact of travel stress. Some animals had to be euthanized prior to experimental endpoints upon recommendation of USC veterinarians due to welfare concerns and could thus not be included in the study.

Cell hashing, single-cell RNA-seq library preparation & sequencing of peritoneal cells

Single-cell libraries were prepared either using Chromium Single Cell 3’ Library & Gel Bead Kit v2 (10X Genomics #PN-120237) [NIA pooled cohorts 1 & 2], or the Chromium Next GEM Single Cell 3 GEM, Library & Gel Bead Kit v3.1 (10X Genomics #PN-1000121) [JAX and NIA single animal cohorts with HTO labeling] according to manufacturer’s instructions (10x Genomics User Guide Chromium Next GEM Single-cell 3′ Reagent Kits v3.1 (CG000204, Rev D)). For the two experiments using the v2 system, isolated peritoneal cells were pooled from each biological group with equal cell number to ensure equal representation of all animals, based

on cell concentration estimates from a COUNTESS cell counter (Thermo Fisher Scientific # AMQAF1000). This resulted in 4 libraries each (*i.e*. young female, young male, old female, old male) for each of 2 independent cohorts. In this case, cell suspensions were loaded for a targeted cell recovery of 3,000 cells per sample. For the two experiments using the v3.1 system, cell hashing was performed on isolated peritoneal cells from each individual using Biolegend TotalSeq^{TM}-A Antibodies according to the manufacturer's instructions (Biolegend #155801, #155803, #155805, #155807, #155809, #155811, #155813, #155815, #155817, #155819). Specifically, 0.5 million peritoneal cells were first incubated with mouse FcR-blocking Reagent (Miltenyi Biotec #130-092-575) at 4°C for 10 minutes. Then, each blocked sample was incubated with 1µg of specific TotalSeq Cell Hashing antibody (HTOs 1-10) at 4°C for 30 minutes. After incubation, stained cells were washed 3 times, and assessed for viability and yield using the COUNTESS cell counter (JAX) or the DeNovix CellDrop (Denovix #CellDrop FL-UNLTD) (NIA). Making sure no overlapping HTOs were included in a pool, samples were pooled in equicellular mixes for 3 reactions (JAX) or 2 reactions (NIA), with targeted cell recoveries of 14,000 and 30,000 cells, respectively. Samples were run on Chromium Single Cell A Chips (10X Genomics #PN-120236) [v2 reactions] or Chromium Next GEM Chip G (10X Genomics #PN-2000177) [v3.1 reactions] according to the manufacturer's instructions. For the v3.1 reactions, HTO Additive primer v2 (Integrated DNA Technologies) was added to the cDNA amplification reaction to amplify the HTO molecules. The amplified HTOs were recovered in the cleanup step for the cDNA amplification, and HTO libraries were built using the 2x NEBNext PCR Master Mix and Truseq indexing oligos (Integrated DNA Technologies). Partially amplified and final single-cell RNA-seq libraries were quantified by a dsDNA High Sensitivity assay (Invitrogen #Q32854) on a Qubit 3.0 Fluorometer (Thermo Fisher Scientific #Q33216). Quality and size distribution of single-cell libraries were assessed on the 4200 TapeStation system (Agilent Technologies #G2991A) with High Sensitivity D1000 DNA ScreenTapes (Agilent Technologies #5067-5582) and D1000 reagent (Agilent Technologies #5067-5583). Libraries were sequenced on an Illumina Novaseq 6000 generating 150 bp paired-end reads at Novogene USA. Raw FASTQ reads have been deposited to the sequence read archive under accession PRJNA1094925.

Computational processing of 10xGenomics sequencing libraries

Mapping, cell filtering and demultiplexing

For all datasets, raw reads were aligned to the mm10 mouse genome and processed using cellranger 6.0.2[125] to generate gene-barcode matrices. For our hashed v3.1 datasets, HTO quantification was performed using CITE-seq-Count v.1.4.4[126] with parameters "-cbf 1 -cbl 16 -umif 17 -umil 26" to parse UMI/HTO sequences. Gene-barcode matrices and HTO counts were loaded in R 3.6.3[127] for downstream processing using Seurat 3.2.2[128,129]. We used SoupX v1.6.1[130] to correct counts for any interference by ambient RNA in our libraries. Cells that were detected in the cellranger data (NIA v2 library) or in both cellranger and HTO data (NIA v3 and JAX v3 libraries) were filtered for downstream analysis. Dead and low-quality cells were filtered out by selecting for cells that contained between 300-6000 genes and < 25% mitochondrial reads. After removal of low-quality unwanted cells, UMI expression data was normalized for downstream processing using SCTransform(), regressing out the impact of number of genes and mitochondrial read load ("vars.to.regress = c("nFeature_RNA", "percent.mito")").

Cell cycle prediction

A list of mouse cell cycle genes was obtained from the Seurat Vignettes (https://www.dropbox.com/s/3dby3bjsaf5arrw/cell_cycle_vignette_files.zip?dl=1), derived from a mouse study of cell cycling[51]. Cell cycle phase was predicted by these reference cell cycle genes using the function CellCycleSorting() to assign cell cycle scores and most likely phase to each cell. This data was used to determine whether there were age-related changes in proliferation patterns of peritoneal macrophages (**Supplementary Figure S1N**).

Singlet identification, doublet removal and cell demultiplexing

Dataset dimensionality was determined using (i) the dimension where the principal components only contribute 5% of standard deviation, (ii) cumulative PCs contribute 90% of the standard deviation, and (iii) the dimension where the percent change in variation between the consecutive PCs is less than 0.1%, using the smallest value. This was determined to be 16 (NIA v2), 21 (NIA v3) and 16 (JAX v3), respectively.

For all our datasets, potential doublets were annotated using Doubletfinder v2.0.3[131] in each particular library, using the predicted doublet rate based on cell capture provided by 10x

Genomics. For the NIA v2 dataset, all cells annotated as singlets by Doubletfinder were retained for downstream analyses.

In addition, for our NIA v3 and JAX v3 libraries, we took advantage of HTO libraries to add a second layer of doublet identification and removal. Specifically, HTO counts were added to the Seurat object as an independent assay and normalized using centered log-ratio (CLR) transformation. Cells were demultiplexed according to their HTO barcode of origin using the MULTIseqDemux() function into their component samples. For these datasets, cells were considered to be singlets if and only if they were annotated as singlets by Doubletfinder and MULTIseqDemux.

Dimensional reduction and cell clustering

Singlet UMI expression data was normalized and scaled for downstream analyses using SCTransform(), regressing out the impact of number of genes, mitochondrial read load and predicted cell cycle scores (“vars.to.regress = c("nFeature_RNA", "percent.mito", S.Score", "G2M.Score)”). The first N principal components (PCs), where N is the estimated dimensionality of the dataset (see above) were used to compute the UMAP transformation with RunUMAP() and cluster cells using FindNeighbors() and FindClusters().

Cell type annotation using SingleR

To identify the most likely cell type annotation for each cell, singlets were annotated using SingleR v.1.0.1[132], together with the reference ImmGen[133] and the mouse RNAseq[134] expression datasets. To guarantee annotation robustness, only cells annotated to the same cell type using both references were kept and annotated with the consensus prediction for all downstream analyses.

Seurat object merging

After independent pre-processing for each dataset, the 3 cohort datasets were also merged into a single Seurat object for analysis. Reciprocal PCA was used to integrate data from the 3 datasets and mitigate batch effects, using the top 3000 most variable genes and k = 10 anchors.

Cell type prioritization using AUGUR and cell type proportion analysis

We used the R package AUGUR v1.0.3[135] to determine which peritoneal cell types were most transcriptionally impacted by age and sex, in the combined and separated objects (**Figure 1C, Supplementary Figure S1A-H**).

We calculated a per library cell type proportion using annotations and analyzed changes in proportions for the most abundant cell types (B-cells, Macrophages and T-cells) across biological groups (**Figure 1D**). In addition, as an orthogonal approach, we computed changes in cell type proportions from the combined and dataset-specific Seurat objects using 'scProportionTest' v0.0.0.9000[46], which runs a permutation test on two different single-cell groups for each cell type and returns the relative change in cell type abundance between groups with a confidence interval (**Supplementary Figure S1I-L**).

Peritoneal lavage immune cell proportion

Flow cytometry analysis was used to validate changes in proportions of immune cell types within the peritoneal cavity from at least two independent cohorts of aged C57BL/6JNia mice, aged C57BL/6J, OVX *vs*. sham C57BL/6J mice, E2-supplemented C57BL/6J mice, and *Esr1* KO mice. A panel of antibodies was used to evaluate differences in the proportion of B-cells, macrophages, and T cells (see below). Specifically, among live cell singlets, B-cells were defined as $CD19^+$, T-cells were defined as $CD3^+$, and macrophages were defined as $F4/80^+$.

Cells were isolated from the peritoneal cavity using a peritoneal lavage. Then, 200,000 peritoneal cells were washed once by adding 1mL of PBS and 2mM EDTA pH 7.2 (Miltenyi Biotec #130-091-222) supplemented with 0.5% BSA (Miltenyi Biotec #130-091-376; MACS resuspension buffer) in a 5mL polystyrene round bottom tube (Falcon #352054), then centrifuged 300g for 10 minutes at 4°C. Cells were resuspended in MACS resuspension buffer in the presence of FcR-blocking solution (concentration following manufacturer recommended dilution) for 10 minutes at 4°C. Afterwards, cells were stained with antibodies for 10 minutes at 4°C protected from light, and excess antibody was washed away using MACS resuspension buffer. Stained cells were then analyzed by flow cytometry on a MACSQuant Analyzer 10 (Miltenyi Biotec #130-096-343), and flow cytometry data was analyzed using FlowLogic V8. Gating was determined using fluorescence-minus-one [FMO] controls for each color used in the experiment to ensure that positive populations were solely associated with the antibody for that specific marker. Raw cytometry data, including FMO controls, were deposited for naïve aging,

sham vs. OVX, E2 supplementation, and *Esr1* KO to Figshare under 10.6084/m9.figshare.28934213, 10.6084/m9.figshare.29169674, 10.6084/m9.figshare.29169737, and 10.6084/m9.figshare.29169707, respectively.

Peritoneal lavage immune cell yield

To assess the age-related impact to immune cell number within the peritoneal cavity, we took total peritoneal lavage cell counts from the DeNovix CellDrop and the identified the fraction of each immune cell types (B-cell, macrophage, T-cell; **Figure 1E**) to calculate original immune cell numbers in the peritoneal cavity. To calculate the number of immune cell types (B-cell, macrophage, and T-cell), the total peritoneal lavage cell counts were multiplied by the fraction of immune cell obtained from flow cytometry (**Figure 1F**).

Isolation of primary peritoneal macrophages

Isolation of primary peritoneal macrophages was performed on aged C57BL/6JNia, aged C57BL/6J, estrus cycle tracking C57BL/6NTac, OVX *vs*. sham C57BL/6J, E2-supplemented C57BL/6J, and *Esr1* KO mice following a protocol from Lu et al. 2020[71] with modifications to remove excess T-cells and B-cells in old animals. Briefly, peritoneal cells were obtained by using a 25G needle (BD #305125) to inject 10mL of filtered sterilized 3% bovine serum albumin (BSA) (VWR #0332-500G) in DPBS (Corning, 21-031-CV) into the peritoneal cavity of euthanized mice. Using a 20-gauge needle (BD #305175), the BSA solution was then harvested back from the peritoneum, now referred to as “peritoneal lavage”. Peritoneal lavages were centrifuged 300g for 10 minutes at 4°C, and cells were resuspended in 1mL of MACS resuspension buffer. To remove any potential contaminating red blood cells, samples were treated with 10mL of 1x Red Blood Cell [RBC] lysis solution (Biolegend #420301) inverted to mix and incubated at 2 minutes at room temperature, then centrifuged 300g for 10minutes at 4°C. To obtain single cell suspension and removal of cell clumps from RBC lysis, macrophages were filtered on 30µm MACS SmartStrainers (Miltenyi Biotec #130-110-915).

Peritoneal macrophages were then isolated using Miltenyi Biotec peritoneal isolation kit (Miltenti Biotec #130-110-434), with modifications to the magnetic labeling step improve purity of macrophage isolation regardless of age, treatment, and genotype. Indeed, while using the unmodified manufacturer’s protocol, we found that aged mice exhibited poor macrophage purity,

with large contamination of B-cells (likely due to B-cell population expansion with aging; **Figure 1D, E**). To improve peritoneal macrophage purity, we routinely added additional biotin labelled antibodies during the "macrophage (peritoneum) biotin-antibody cocktail" labeling step to help deplete potential excess B-cells, T-cells and monocytes from peritoneal lavages. Specifically, 5µL of biotinylated anti-CD19 (Miltenyi Biotec #130-119-757), anti-CD79b (Miltenyi Biotec #130-105-832), anti-CD3e (Miltenyi Biotec #130-093-179) and anti-Ly6c (Miltenyi Biotec #130-111-776) antibodies were added during incubation for 10 minutes at 4°C. After primary antibody incubation, all other steps in isolating peritoneal macrophages were performed according to the manufacturer's instructions. This allowed us to routinely achieve high purity for isolated peritoneal macrophages. Magnetic Activated Cell Sorting (MACS)-purified peritoneal macrophages were used for downstream experiments, including 'omic' and functional profiling.

Purity and identify of MACS-purified peritoneal macrophages

Potential phenotypic differences in MACS-purified peritoneal macrophage purity were assessed from independent cohorts of aged C57BL/6JNia, aged C57BL/6J, OVX vs. sham C57BL/6J, E2-supplemented C57BL/6J, and *Esr1* KO mice. Briefly, 100,000 MACS-purified peritoneal macrophages were used for flow cytometry labeling. After FcR-blocking, macrophages were stained using F4/80-APC (1:50; Miltenyi Biotec #130-116-547) and CD11b-Vioblue (1:50; Miltenyi Biotec #130-113-238) antibodies according to the manufacturer's instructions. Stained cells were analyzed by flow cytometry on the Miltenyi Biotec MACSQuant Analyzer 10. Flow cytometry results were processed using the FlowLogic V8 software. Pure macrophages were designated as double positive F4/80^{+} CD11b^{+} cells. From these, large peritoneal macrophages were defined as F4/80^{+high}, and small peritoneal macrophages were defined as F4/80^{+low}. The raw flow cytometry data for naïve aging, sham vs. OVX, E2 supplementation, and *Esr1* KO analyses has been deposited to Figshare under 10.6084/m9.figshare.28934198, 10.6084/m9.figshare.29169578, 10.6084/m9.figshare.29169581, and 10.6084/m9.figshare.29169587, respectively.

RNA purification from primary macrophages and macrophage cell lines

For RNA isolation of primary peritoneal macrophages, frozen cell pellets were resuspended in 500µL of TRIzol reagent (Thermo-Fisher #15596018), and total RNA was purified following the manufacturer's instructions. RNA quality was assessed using the Agilent Technologies 4200 TapeStation system using High Sensitivity RNA ScreenTapes (Agilent Technologies #5067-5579) together with RNA ScreenTape Sample Buffer (Agilent Technologies #5067-5577).

For RNA isolation of modified RAW264.7 and J774A.1 cells (see below), 60-80% confluency in a 6-well plate were lysed using 1mL of TRIzol reagent, and RNA was extracted using DirectZol columns (Zymo #R2052) following manufacturer's protocol.

RNA-seq library preparations for primary peritoneal macrophages and macrophage cell lines

For primary peritoneal macrophages, we constructed ribosomal RNA depleted strand-specific bulk RNA-sequencing libraries in house as previously described Lu et al. 2021[24]. Briefly, 450ng of total RNA was subjected to ribosomal-RNA depletion using the NEBNext rRNA Depletion Kit v2 (New England Biolabs #E705X), according to the manufacturer's protocol. Strand specific RNA-seq libraries were then constructed using the SMARTer Stranded RNA-seq Kit (Clontech #634841, #634863), according to the manufacturer's protocol. Libraries were quality controlled on the Agilent Technologies 4200 TapeStation system with Agilent Technologies D1000 ScreenTape and Agilent Technologies D1000 reagent, before multiplexing the libraries for sequencing. Paired-end 150bp reads were generated on the Illumina Novaseq X or Novaseq 6000 platforms at Novogene USA. Raw FASTQ sequencing reads were deposited to SRA under Bioprojects accession PRJNA1095555 and PRJNA1101936.

For macrophage cell line derived samples, total RNA samples were sent to the Novogene corporation for unstranded mRNA-sequencing. Briefly, the company performed mRNA selection using poly (A) capture, RNA fragmentation, cDNA reverse transcription and then unstranded RNA sequencing library preparation. RNA libraries were sequenced as paired-end 150bp reads on the Illumina Novaseq X or Novaseq 6000 platforms. Raw FASTQ sequencing reads were deposited to SRA under Bioprojects accession PRJNA1096052 and PRJNA1222371.

RNA-seq analysis pipeline

Paired end 150bp FASTQ reads were hard-trimmed to 100bp at their 3' end to improve mapping rates and the first 9bp at the 5' end were trimmed to eliminate priming biases[136]. This was done using Fastx Trimmer 0.0.13 (https://github.com/agordon/fastx_toolkit), or Trimgalore 0.6.6 (github.com/FelixKrueger/TrimGalore) after a system upgrade made it impossible to use Fastx Trimmer. For Trimgalore, additional required stringency filters were added to eliminate any bases with phred score < 15 (corresponding to < 1% of bases). Trimmed reads were mapped to the mm10 genome reference using STAR 2.7.7a[137]. Read counts were assigned to genes from the UCSC mm10 reference using featureCounts from subread 1.5.3[138], using either the stranded or unstranded option based on library construction (see above). Read count tables were imported into R 3.6.3[127] for downstream processing. Based on general RNA-seq processing guidelines, only genes with mapped reads in at least half of the samples in each analysis were considered to be expressed and retained for analysis.

The 'DESeq2' R package v1.26.0 was used for normalization and differential gene expression analysis of the RNA-seq data in R[139] using appropriate analytical covariates (*e.g.* sex, age, treatment, etc.). Genes with a false discovery rate < 5% in any analysis were considered statistically significant. For analysis of sex-specific age-regulation of genes, we considered a gene to be specifically regulated with age in females (males) if the DESeq2 FDR was < 5% in females (males) and > 10% in males (females). DESeq2 results are reported in **Supplementary Table S2A**.

ATAC-seq library generation for primary peritoneal macrophages

A second independent cohort of C57BL/6JNia mice was used to assess the impact of age and sex on peritoneal macrophage chromatin accessibility (**Supplementary Table S1A**). We constructed ATAC-seq libraries in house as described Lu et al. 2021[24], using the omni-ATAC protocol and starting from 50,000 MACS-purified peritoneal macrophages[53]. Libraries were quality controlled using the Agilent Technologies 4200 TapeStation system with Agilent Technologies High Sensitivity D1000 DNA ScreenTape and reagent before multiplexing the libraries for sequencing. Paired-end 150bp reads were generated on the Illumina Novaseq 6000 platform at Novogene USA. Raw FASTQ sequencing reads were deposited to SRA under Bioproject accession PRJNA1095555.

ATAC-seq preprocessing pipeline

Paired-end ATAC-seq reads were adapter-trimmed using NGmerge 0.3[140], a tool recommended for use in ATAC-seq preprocessing which clips overhanging reads in a sequence-independent fashion. Trimmed paired-end were mapped to the mm10 genome reference using bowtie2 v2.5.1[141]. After alignment, PCR duplicates were removed using the 'rmdup' function of samtools 0.1.19[142]. Reads from all samples were pooled define "meta-peaks" for robust differential accessibility analysis using samtools 'merge'. We used MACS2 v2.2.7.1 to identify ATAC-seq accessible regions[143]. A normalized read count matrix was then obtained using our mapped read bam files over MACS2 meta-peaks using R package 'Diffbind' 2.14[144], which was used for downstream analyses. 'DESeq2' 1.26.0 was used for normalization and differential gene expression analysis of ATAC-seq data in R[139] using appropriate analytical covariates (*e.g.* sex, age). Peaks with a false discovery rate < 5% in any analysis were considered statistically significant. For analysis of sex-specific age-regulation of chromatin region accessibility, we considered a chromatin region to be specifically remodeled with age in females (males) if the DESeq2 FDR was < 5% in females (males) and > 10% in males (females). DESeq2 results are reported in **Supplementary Table S2B**.

H4K4me3 CUT&RUN library generation for primary peritoneal macrophages

A third independent cohort of C57BL/6JNia mice was used to assess the impact of age and sex on peritoneal macrophage H3K4me3 landscapes (**Supplementary Table S1A**). We used a CUT&RUN protocol adapted from the kit manual from EpiCypher, with modifications to account for the use of immune cells (*i.e.* to avoid unscheduled immune activation from ConA signaling on cells). All buffers were made in-house.

Nuclei isolation

250,000 MACS-purified peritoneal macrophages were harvested and resuspended in 100µL of 1X DPBS. Samples were centrifuged for 3 min at 600g at room temperature and supernatant was discarded. Cells were resuspended in 100µL of ice-cold Nuclear Extraction Buffer (20mM HEPES [Sigma-Aldrich #H3375], pH 7.9, 10mM KCl [Sigma-Aldrich # P9541], 0,1% Triton X-100 [VWR # M143], 20% Glycerol [VWR # BDH1172], 0.5mM Spermidine [EMD Millipore # 56766] and 1x Protease Inhibitor [Roche #11873580001]) and incubated on

ice for 10 min. Samples were centrifuged for 3 min at 600g at 4 °C and supernatant was removed. Samples were resuspended in 100µL of ice-cold Nuclear Extraction Buffer and kept on ice until further processing.

Concanavalin A bead activation

11µL per sample of gently resuspended Concanavalin A (ConA) beads were transferred to fresh 1.5mL tubes. Tubes were placed on a magnetic separation rack until slurry cleared and supernatant was removed. 100µL of ice-cold Bead Activation Buffer (20 mM HEPES, pH 7.9, 10 mM KCl, 1 mM $CaCl_2$ and 1 mM $ManCl_2$) was added to each tube and pipetted 10 times to mix and wash the beads for a total of two washes. Washed beads were resuspended in 11µL of ice-cold Bead Activation Buffer. 10µL of activated bead slurry was transferred into fresh 1.5mL tubes. Beads were kept on ice until further processing.

Immunolabeling of chromatin

Isolated nuclei were collected by centrifugation at for 3 min at 600g at 4 °C and supernatant was discarded. Nuclei were resuspended in 100µL of Wash Buffer (20mM HEPES, pH 7.5, 150mM NaCl, 0.5mM Spermidine and 1x Protease Inhibitor) and transferred to the tubes containing the activated Concanavalin A beads. Samples were incubated at room temperature for 10 min. Tubes were placed on a magnetic separation rack until slurry cleared and supernatant was removed. 50µL of ice-cold Antibody Buffer (20mM HEPES, pH 7.5, 150mM NaCl, 0.5mM Spermidine, 1x Protease Inhibitor, 0.01% Digitonin and 2mM EDTA) was added to each sample. 0.5µL of anti-H3K4me3 antibody (Active Motif #39159) was added to each sample. Samples were incubated on a nutator overnight at 4°C. Tubes were placed on a magnetic separator rack until slurry cleared and supernatant was removed. While keeping the tubes on the magnetic separator, 250µL of ice-cold Digitonin Buffer (20mM HEPES, pH 7.5, 150mM NaCl, 0.5mM Spermidine and 1x Protease Inhibitor and 0.01% Digitonin) was added to the tubes and supernatant was removed without disturbing the tubes. Digitonin Buffer wash step was repeated once more for a total of two washes. 50µL of ice-cold Digitonin Buffer was added.

pAG-MNase binding and DNA purification

2.5µL of CUTANA pAG-MNase (EpiCypher # 15-1016) was added to each sample and gently mixed by vortexing. Samples were incubated at room temperature for 10 min and placed on a magnetic separator. Supernatant was removed by pipetting. While the tubes were on the magnet separator, 250µL of ice-cold Digitonin Buffer was added to each sample and removed. Digitonin Buffer wash step was repeated once more for a total of two washes. 50µL of ice-cold Digitonin Buffer was added to the tubes and gently mixed by vortexing. 1µL of 100mM $CaCl_2$ was added to each sample and gently mixed by vortexing. Samples were incubated on a nutator for 2 hours at 4°C. 33µL of Stop Buffer (340mM NaCl, 20mM EDTA, 4mM EGTA, 50µg/mL RNaseA, 50µg/mL GlycoBlue Coprecipitant) was added to each sample. Samples were incubated at 37 °C for 10 min in a thermocycler. Samples were placed on a magnetic separator until slurry cleared and the supernatant was collected to new 1.5 ml tubes. DNA purification was performed using the DNA Clean & Concentration-5 kit (Zymo Research #D4013) according to the manufacturer's instructions.

Sequencing library preparation and sequencing

CUT&RUN sequencing libraries were prepared using the NEBNext Ultra II Library Prep Kit for Illumina kit (NEBNext #E7645), according to the manufacturer's instructions. H4K4me3 CUT&RUN libraries were multiplexed and sent for sequencing on the Illumina NovaSeq 6000 platform to Novogene USA. De-multiplexed FASTQ files were provided by Novogene for data analysis. Raw FASTQ sequencing reads were deposited to SRA under Bioproject accession PRJNA1095555.

H4K4me3 CUT&RUN preprocessing pipeline

Paired-end H4K4me3 CUT&RUN reads were adapter-trimmed using NGmerge 0.3[140]. Trimmed paired-end were mapped to the mm10 genome reference using bowtie2 v2.5.1[141]. After alignment, PCR duplicates were removed using the 'rmdup' function of samtools 0.1.19[142]. Reads from sequenced samples were pooled in order to define "meta-peaks" for robust differential accessibility analysis using samtools 'merge'. We used MACS2 v2.2.7.1 to identify H4K4me3 modified regions[143]. A normalized read count matrix was then obtained using our mapped read bam files over MACS2 meta-peaks using R package 'Diffbind' 2.14[144], which was

used for downstream analyses. 'DESeq2' 1.26.0 was used for normalization and differential gene expression analysis of H4K4me3 CUT&RUN data in R[139] using appropriate analytical covariates (*e.g.* sex, age). Peaks with a FDR < 5% in any analysis were considered statistically significant. For analysis of sex-specific age-regulation of H4K4me3 signal intensity, we considered a chromatin region to be specifically remodeled with age in females (males) if the DESeq2 FDR was < 5% in females (males) and > 10% in males (females). DESeq2 results are reported in **Supplementary Table S2C**.

Multidimensional Scaling analysis

To perform Multidimensional Scaling (MDS) analysis, we used a simple distance metric between samples based on the Spearman's rank correlation value (1-Rho), which was then provided to the core R command 'cmdscale'. Dimensionality reduction was applied to DESeq2-normalized data, obtained as described in relevant sections above.

Putative Protein-Protein Interaction [PPI] network analysis with NetworkAnalyst

Genes with significant regulation with aging in female or male peritoneal macrophages (DESeq2 FDR < 5%; **Supplementary Table S2A**) were used as input for network analysis with NetworkAnalyst 3.0[60]. Significant age-regulated genes in each sex and their corresponding DESeq2 computed $\log_2$(fold-change) were used as input. In both cases, we had NetworkAnalyst use PPI information derived from IMEx/InnateDB data, a knowledgebase specifically geared for analyses of innate immune networks[61], to construct putative PPI networks. In each case, the largest subnetwork determined by NetworkAnalyst was used in our analyses (**Figure 3A, B**).

Functional enrichment analysis by Gene Set Enrichment Analysis

We used the Gene Set Enrichment Analysis (GSEA) paradigm[145] through the 'phenotest' v1.34.0 package. Significance was calculated using 10,000 permutations.

GSEA analysis using Gene Ontology and Reactome gene sets

Gene Ontology term annotation were obtained from ENSEMBL through Biomart (Ensembl 108; downloaded on 2022-12-21), and gene-term association with only author statement support (GO evidence codes 'TAS' and 'NAS') or unclear evidence (GO evidence

code ‘ND’) was filtered out. The Reactome annotations were obtained from the Molecular Signature Database mouse v2022.1[66]. For RNA-seq GSEA analysis, differential gene regulation information and gene-centric statistics were obtained directly from the DESeq2 result table without further processing. For ATAC-seq and H3K4me3 CUT&RUN GSEA analyses, the peak-centric DESeq2 result tables were first processed to generate gene-centric results compatible with GSEA. Specifically, only peaks with 10kb of annotated TSSs according to HOMER v5.1 ‘annotatePeaks.pl’ script[98] were retained. For ATAC-seq, to capture the most strongly remodeled regulatory elements, the gene-centric data was obtained by capturing the DESeq2 statistics for the peak with the most significant DESeq2 FDR, and in the case of peaks tied for FDR, with the largest absolute $\log_2$(fold change) with aging among tied peaks for each annotated gene. For H3K4me3 CUT&RUN, to capture the peak most representative of gene promoters (since H3K4me3 is a modification typical of promoters), the gene-centric data was obtained by capturing the DESeq2 statistics for the peak closest to each annotated gene.

In all cases, from gene-centric result tables, the DESeq2 t-statistic was used to generate the ranked list of genes for functional enrichment analysis with aging in female and male macrophages separately. The ‘gsea’ function from phenotest’ was run on gene sets with a size of 20 to 5000 genes, filtering too small or too large gene sets, so as to improve biological robustness. For ease of reading, only the top 5 most significant sex-specific gene sets or top 10 most significant sex independent gene sets are shown in figures, with all shown gene sets passing FDR < 5%. All significantly regulated gene sets are reported in **Supplementary Tables S3**.

GSEA analysis of curated gene sets for top functional processes

For curated gene set analyses (**Figure 3F-H**), we used curated gene sets for validation of important top curated processes. Specifically, we curated candidate regulators of phagocytosis from CRISPR/Cas9 screens based on results reported by Haney et al. 2018 and Pluvinage et al. 2019[64,65]. We obtained mouse Hallmark curated gene sets “Glycolysis” and “Oxidative Phosphorylation” from the Molecular Signature Database mouse v2022.1[66]. We obtained a set of genes upregulated in M1 and M2 *in vitro* polarized BMDMs, by reanalyzing a publicly available RNA-seq dataset (accession number GSE103958)[67]. Briefly, downloaded FASTQ reads were mapped using STAR, a count table generated using featureCounts from subread, and differential gene expression analysis was performed using DESeq2 comparing M0 (untreated) vs. M1 (IFNg

LPS treated) BMDMs, and M0 (untreated) vs. M1 (IL4 or IL13 treated) BMDMs. Genes with FDR < 5% and upregulated upon M1/M2 treatments were used as signatures of polarization for analysis (M1: 1392 genes; M2: 760 genes; **Supplementary Table S4C**).

GSEA analysis of macrophage-regulated gene sets

To compare the impact of various interventions on macrophage transcriptomes to that of aging in peritoneal macrophage from female mice, we also leveraged a GSEA approach. Specifically, we used our various RNA-seq experiments to identify genes significantly regulated in response to *in vivo* interventions (*i.e.* OVX vs. Sham, E2-supplementation vs. Vehicle, *Esr1* KO) or *in vitro* modulation (*i.e.* TF gene shRNA knockdown; see below).

In all cases, we performed DESeq2 differential gene expression analysis of our datasets to identify genes with significant regulation across our conditions (see above). For RNA-seq datasets measuring the impact of *in vivo* interventions on primary peritoneal macrophage transcriptomes, we obtained gene sets corresponding to genes significantly upregulated or downregulation in response to the intervention at FDR < 5%. These lists were then used as gene sets for GSEA analysis with phenotest (**Figure 5D, J, P**). For *in vitro* modulation of TF gene expression datasets, we used a more stringent definition for target gene sets to limit the impact of hairpin-specific off-target effects. Specifically, for each candidate TF, we performed differential expression analysis comparing control (i.e. non mammalian and luciferase hairpins) to each hairpin separately. To identify robust and consistent transcriptional targets, we then performed Fisher combination of adjusted p-values across both hairpins (analytical tables provided in **Supplementary Table S6C-G**). Genes were considered to be significant transcriptional targets of a candidate TF if and only if (i) they showed consistent direction of transcriptional regulation across both hairpins, and (ii) if their Fisher combined adjusted p-values were $< 10^{-4}$ as a stringent filter. Heatmaps showing consistent regulation for the chosen gene sets to be used for GSEA analysis are reported in **Supplementary Figure S6G**, showing that our approach identifies consistent transcriptional targets. These lists were then used as gene sets for GSEA analysis with phenotest (**Figure 6G**).

Growth and maintenance of cell lines

All cell lines were cultured in a humidified incubator under 5% CO_2-95% air at 37°C. L929 cell line (ATCC CCL-1) were cultured with Dulbecco's Modified Eagle's Medium/ Hams F-12 50/50 mix (DMEM/F-12 50/50; Corning #10-090-CV) supplemented with 10% fetal bovine serum (FBS) (Sigma-Aldrich #F0926), and 1x penicillin streptomycin L-glutamine (Corning # 30-009-Cl). L929 cells were seeded in vented T175 tissue culture flasks (VWR #10062-864) at 10% confluency. Once cells reached around 80% confluency, conditioned media was collected and filtered through a 0.45µM filter (GenClone #25-246). Conditioned media was stored at -20°C until use (see below). HEK293T (ATCC CRL-3216), RAW264.7 (ATCC TIB71), and J774A.1 (ATCC TIB-67) were cultured with Dulbecco's Modified Eagle's Medium (DMEM) (Corning #15-013-CV) supplemented with 10% FBS, and 1x penicillin streptomycin L-glutamine. Media was changed every 2-3 days. To passage cell lines, L929, HEK293T, and RAW264.7 cells were detached using 0.05% trypsin (Coring #25-052-Cl) for 5 minutes at 37°C. After incubation, trypsin was neutralized by adding double the volume of complete media to the trypsin used. Cells were pelleted by centrifugation at 300g for 5 minutes at room temperature. For passaging of J774A.1 cells, cells were detached using a cell lifter (VWR #76036-006). Cells were collected and pelleted at 300g for 5 minutes at room temperature. Supernatant was discarded and cells were resuspended with 1mL of complete media. Cells were seeded at lower densities in a new tissue culture plate as needed based on experimental needs. All cell lines were re-authenticated after establishing culture in the laboratory using the ATCC cell line STR profiling service to confirm their identity in presented experiments.

Culture of primary peritoneal macrophages and BMDMs

All primary macrophages were cultured in a humidified incubator under 5% CO_2-95% air at 37°C. MACS-purified peritoneal macrophages were cultured in macrophage media (DMEM/F-12 50/50 supplemented with 10% FBS, 1x antibiotic antimycotic (Gibco #15240-062), 10% L929 conditioned media and 2ng/mL M-CSF (Miltenyi Biotec #130-101-706)) in non-treated tissue culture plates. Bone marrow cells were obtained from the hind legs of aged C57BL/6JNia, aged C57BL/6J and estrus cycle tracked C57BL/6NTac mice following as before[71]. Briefly, after bone marrow harvest following Amend et al. 2016 protocol[71,146], cells were resuspended in 1mL of MACS resuspension buffer and treated with 1x RBC lysis solution for 2 minutes at room temperature, then centrifuged at 300g for 10minutes at 4°C. Resuspended

RBC-lysed bone marrow cells were then filtered on a 70μM filter to remove debris and clumps (Miltenyi Biotec #130-110-916). Cells were then transferred to macrophage media for culture in T75 vented untreated tissue culture flasks (Greiner Bio-One #658195) for differentiation into bone marrow derived macrophages. After 3 days, the media was replaced with fresh macrophage media and differentiation continued for a total of seven days after euthanasia and bone marrow harvest. Obtained BMDMs were then used for downstream experiments (*i.e.* phagocytosis assay (**Supplementary Figure S4B**) and Agilent Seahorse metabolic profiling (**Figure 4I, J, Supplementary Figure S4J, K**).

Analysis of macrophage phagocytic capacity

We used our previously described microscopy-based phagocytosis assay protocol[71] and a new streamlined flow cytometry-based phagocytosis assay protocol to quantify the phagocytic capacity of primary macrophages and macrophage cell lines.

Briefly, for the microscopy protocol, 75,000 macrophages were seeded in a 24-well plate with a 12mm glass coverslip (Electron Microscopy Sciences #72231-01), with technical duplicates for each animal. Macrophages were allowed to attach overnight, before treatment for 1 hour with 1mg/mL Alexa Fluor 488-labelled Zymosan bioparticles (Invitrogen #Z23373) diluted in macrophage media. After 1-hour, Zymosan particles were washed three times with ice-cold DPBS, and cells were fixed with 4% formaldehyde (Macron #H121-05) for 10 minutes at room temperature. After fixation, coverslips were washed three times with DPBS and mounted on microscope slides (VWR #48311-703) with prolong diamond antifade mounting medium with DAPI (Invitrogen #P36962). Images of phagocytosis were acquired using the Keyence microscope (Keyence #BZ-X710) with the 10x objective. Stitched images of a 3 by 3 field were then counted by blinded experimenters. To quantify Zymosan-internalized (green fluorescent) cells and total cell number, images were analyzed using ImageJ software[147]. Total cell counts were determined by identifying DAPI-stained nuclei using the “Analyze Particles” function following appropriate thresholding. Due to the possibility of multiple phagosomes within a single cell, Zymosan-positive cells were manually counted to ensure accurate identification of individual phagocytic cells The phagocytosis index was determined by calculating the ratio of Alexa Fluor 488–positive cells to the total number of cells. Phagocytosis images for aging and

estrus cycling has been deposited to Figshare under 10.6084/m9.figshare.29286194 and 10.6084/m9.figshare.29286206, respectively.

For our new flow cytometry-based protocol, 100,000 macrophages were first blocked with FcR-blocking reagent for 10 minutes at 37°C. For primary MACS-purified peritoneal macrophages, we also included an additional staining step with F4/80-APC (Miltenyi Biotec #130-116-547) for downstream data filtering. For both primary and immortalized macrophages, cells were then treated with Alexa Fluor 488-labelled Zymosan bioparticles as above, targeting with a multiplicity of infection (MOI) of 2 per macrophage for 30 minutes at 37°C. After treatment, macrophages were fixed with a final concentration of ice cold 2% formaldehyde solution (Macron #H121-05) at 4°C protected from light. Macrophages were washed twice and resuspended in 500uL of MACS resuspension buffer, then analyzed on the MACSQuant Analyzer 10 to phagocytosis capacity. Gating was determined using fluorescence-minus-one [FMO] controls for each color used in the experiment to ensure that positive populations were solely associated with the antibody/particle Analysis was performed in Flowlogic V8 software. Flow cytometry data for aging, sham vs. OVX, E2 supplementation, *Esr1* KO, RAW264.7 phagocytosis regulator knockdown, RAW264.7 transcription factor candidate knockdown, and J774A.1 Irf2 knockdown phagocytosis has been deposited to Figshare under 10.6084/m9.figshare.29161955, 10.6084/m9.figshare.29169836, 10.6084/m9.figshare.29169821, 10.6084/m9.figshare.29169860, 10.6084/m9.figshare.29169821, 10.6084/m9.figshare.29169872, 10.6084/m9.figshare.29169899, and 10.6084/m9.figshare.29286278, respectively.

Cell surface marker protein level quantification by flow cytometry

To estimate potential differences in peritoneal macrophage surface markers (*i.e*. Zymosan pattern recognition receptors, M1/M2 markers) with respect to sex and age, 100,000 MACS-purified peritoneal macrophages were subjected to Fc receptor blocking (Miltenyi Biotec #130-092-575) and stained with corresponding antibodies according to the manufacturer's instructions. For analysis of pattern recognition receptors, cells were stained with F4/80-Brilliant Violet 421 (1:20) (Biolegend #123131), Dectin-1-PE (1:10) (Miltenyi Biotec #130-102-284), and CD282 (Tlr2)-APC (1:50) (Miltenyi Biotec #130-120-052). For M1 marker detection, cells were stained with CD80-FITC (1:20) (Biolegend #104705) and CD86-APC (1:20) (Biolegend #105011). For M2 marker detection, cells were stained with CD163-PE (1:20) (Biolegend #111803) and

CD206-APC (1:20) (Biolegend #141707). After gating on F4/80 positive cells, we obtained median fluorescent intensity (MFI) of stained cells for surface proteins of interest using flow cytometry quantification on the Milteni Biotec MACSQuant Analyzer 10. Flow cytometry results were processed using the FlowLogic V8 software. Flow cytometry data has been deposited to Figshare under 10.6084/m9.figshare.29162144.

Metabolic profiling of macrophages using the Agilent Seahorse platform

50,000 BMDMs or transduced macrophage cell lines (RAW264.7, J774A.1) cells were seeded in a 96-well Seahorse assay plate with macrophage media (or appropriate culture media) and incubated overnight for cells to attach. To characterize the bioenergetics of cells, a XF–96 Flux Analyzer (Agilent Technologies) was used. Growth media was replaced with 175µL of XF assay medium (specially formulated, unbuffered Dulbecco's modified Eagle's medium for XF assay; Agilent Technologies #103575-100) supplemented with 1mM sodium pyruvate at pH 7.4 (Agilent Technologies #103578-100). The cells were kept in a non-CO_2 incubator for 60 minutes at 37°C before placing in the analyzer. Oxygen consumption rate [OCR] and extracellular acidification rate [ECAR] were measured using 3 cycles of 3 minutes wait and 4 minutes measure time. Each biological replicate had three technical replicates and the results obtained were averaged. Injection of compounds and calculating metabolic parameters were obtained by following an established protocols for macrophages[78].

To normalize OCR and ECAR values to actual live/seeded cell number, the cell media was removed from 96-well plates at the end of the assay and air died for around 10 minutes before storage at -80°C at least overnight to initiate cell lysis. To finalize cell lysis, 100µL of nuclease-free water was added to each well and incubated at 37°C for 1 hour, and plates were refrozen for > 1 hour at -80°C. Plates were thawed at room temperature, and 200µg/mL Hoechst (Thermo Scientific #H1399) in TNE buffer (10mM Tris [Thermo scientific #J22675-A1], 1mM EDTA [VWR #BDH7830-1], 2M NaCl [Sigma-Aldrich #S5150-1L], pH 7.4) was added to each well. Plates were read at excitation 346 and emission 460 on Molecular Devices SpectraMAX M3. Fluorescent values were then used to divide the OCR and ECAR values to obtain normalized, comparable values. Seahorse data for aging, estrus cycling, transcription factor candidate knockdown in RAW264.7, and *Irf2* knockdown in J774A.1 has been deposited under

10.6084/m9.figshare.29169911, 10.6084/m9.figshare.29169920, 10.6084/m9.figshare.29169926, and 10.6084/m9.figshare.29169938, respectively.

Measurement of macrophage glycolytic function using Lactate-Glo

30,000 MACS-purified peritoneal macrophages or RAW264.7/J774A.1 cells were seeded into a 96-well plate tissue culture plate (GenClone #25-109) with 100µL of fresh media. Then, 48 hours after seeding (primary peritoneal macrophages) or 24 hours (macrophage cell lines), the conditioned media was collected and stored at -20°C until further processing. To note, for this experiment, transduced RAW264.7/J774A.1 cells were cultured without puromycin (see below) to avoid metabolic abnormalities due to the impact of puromycin on mitochondrial function[148]. To measure the amount of lactate in the condition media, Lactate-Glo (Promega #J5021) was used following to the manufacturer's protocol and luminescence values were collected using Promega GLOMAX (Promega #GM3500) plate reader. Luminescence values were normalized to actual live/seeded cell numbers using the same method as for the Seahorse assay (see above).

Lentiviral particle production for shRNA-mediated gene knockdown

In all cases, plasmid DNA was isolated from overnight cultures using mini-preps from the Macherey-Nagel NucleoSpin Plasmid kit (Macherey-Nagel #740588.250) according to the manufacturer's protocol, and DNA was sent to GENEWIZ or Plasmidsaurus for sequence validation before use in any experiment.

We used a lentiviral shRNA particle approach to mediate gene-specific RNA interference and evaluate the impact of decreased gene expression of candidate phagocytosis regulators or TF-mediators on macrophage phenotypes. We obtained 3rd generation of lentiviral vector packaging backbones from Addgene: pMDLg/pRRE (Addgene #12251), pRSV-Rev (Addgene #12253), VSV.G (Addgene #14888). To guarantee single clone origin of laboratory isolates, bacteria were re-streaked on a 100µg/mL carbenicillin (Sigma-Aldrich #C3416) Luria broth (LB; Thermo Scientific #J75852-A1) 1% agar (Invitrogen #30391-023) plates and incubated overnight at 37°C. For plasmid preparation, single colonies were isolated and inoculated into culture tube containing 100µg/mL carbenicillin in LB media for culture at 37 °C with shaking for 16-20 hours for each construct. Plasmid DNAs were obtained using the NucleoBond Xtra midi plus EF kit (Macherey-Nagel #740422.50) following manufacturer's recommendation.

MISSION® shRNA control and target bacterial glycerol stocks were obtained from Sigma-Aldrich (**Supplementary Table S1G-H**). To obtain single bacteria colonies, frozen glycerol stocks were inoculated into sterile culture tubes (Genesee Scientific #21-129) containing 0.5mL terrific broth (TB) (Sigma-Aldrich #T0918-1KG) without antibiotics and incubated at 37 °C with shaking for 30 minutes. Next, 50µL of bacteria pre-cultures was spread on prewarmed 100µg/mL carbenicillin TB 1% agar plate, and incubated for 16 hours at 37 °C. For plasmid preparation, a single colony was isolated from the plate and inoculated into a culture tube containing 100µg/mL TB, incubated at 37 °C with shaking for 16-20 hours for each construct. To produce a large quantity and endotoxin free plasmid DNA, 200mL of 100µg/mL TB bacteria culture was inoculated and incubated at 37°C with shaking for 20 hours. Plasmid DNAs were obtained using the NucleoBond Xtra midi plus EF kit (Macherey-Nagel #740422.50) following manufacturer's recommendation.

Lentiviral particles were produced by transfection of HEK293T cells using the calcium phosphate transfection method[149]. Transfection mixtures were prepared by combining plasmid DNA (contained pMDLg/pRRE (1,000 ng), VSV.G (500 ng), pRSV-Rev (500 ng), and the pLKO shRNA plasmid of interest (1000ng)), with 2.5 M calcium chloride (Sigma-Aldrich #C1016-500G) and mixing with 0.22µM filter sterilized 2xHEPES-buffered saline ([HBS] 140mM NaCl, 1.5mM $Na_2HPO_4 \cdot 2H_2O$ (VWR #0348-500G), 50mM HEPES)) to form DNA-calcium phosphate complexes. The DNA-calcium phosphate complexes were formed for 2 minutes at room temperature and then added dropwise on HEK293T cells at 60-80% confluency. HEK293T were incubated with DNA-calcium phosphate complexes for 16 hours, then media was changed to fresh complete media. After 24 hours, supernatants containing viral particles were collected and filtered using a 0.45µM filter to remove cells.

To concentrate lentiviral particles before use, supernatant was carefully layered on top of a layer of 20% sucrose (Sigma-Aldrich #S0389-1KG) in DPBS solution in a Beckman Coulter polypropylene quick-seal centrifuge tube (Beckman Coulter #343414). Viral preps were centrifuged at 70,000 x g for 2 hours at 4°C in an Optima XPN-100 Ultracentrifuge (Beckman Coulter #B10053). After centrifugation, the layered supernatant was removed, and viral pellets were resuspended and concentrated 100x in ice cold DPBS. Lentiviral particles were aliquoted and stored at -80°C until experiments.

Lentiviral transduction of macrophage cell lines

Macrophage cell lines were seeded at a density of 30,000 cells per well in a 96-well tissue culture plate (GenClone #25-109) and incubated for 48 hours. During this period, cells were treated with various concentrations of puromycin in complete media (10, 8, 6, 4, 2,1µg/mL) (Sigma-Aldrich #P8833), to assess cytotoxicity. On the second day, 100µL of the culture medium in each well was replaced with fresh medium containing the corresponding concentration of puromycin. Following the manufacturer's instructions, CyQUANT™ XTT Cell Viability (Invitrogen #X12223) assay reagents were added to each well to assess cell viability. The plates were then incubated for 4 hours at 37 °C. Absorbance was measured at 450 nm and 660 nm using a microplate reader. Specific absorbance values were calculated by subtracting the 660 nm reference readings from the 450 nm readings.

For transduction, 200,000 cells from macrophage cell lines (RAW264.7, J774A.1) were seeded in a 12-well tissue culture plate (GenClone #25-109) one day before infection. The next day, cells were infected with viral particles at a MOI of 1 in the presence of 8µg/mL polybrene (Sigma-Aldrich #TR-1003-G). After 24 hours, the media was replaced with fresh complete media. 48 hours after infection, cells were selected using complete media with addition of 10µg/mL of puromycin (Sigma-Aldrich #P8833), as determined with our in house kill curve for these cells (see above). Molecular and/or functional profiling of modified cells was performed on puromycin-selected macrophage cells cultured in complete media supplemented with 10µg/mL puromycin, expect for metabolic assays where 24 hours prior, media was changed to complete media without puromycin.

Reverse transcription quantified PCR verification of shRNA gene knockdown

Total RNA was reverse transcribed into complementary DNA (cDNA) using the Thermo Scientific™ Maxima H Minus First Strand cDNA Synthesis Kit (Thermo scientific #K1682), according to the manufacturer's instructions. Quantitative PCR was performed using the SensiFAST SYBR No-ROX Kit (Bioline #BIO-98020) with gene-specific primers (For sequences see **Supplementary Table S1I**) to assess relative gene expression. cDNA, primers, and SYBR master mix were first combined in a PCR tube to ensure a homogeneous mixture, then transferred into Mic qPCR-specific tubes (QuantaBio #95910-20) for amplification using the Mic qPCR Cycler (Bio Molecular Systems #MIC-2). Gene expression levels were quantified

using the ΔΔCt method and normalized to the geometric mean of three housekeeping genes (*18s*, *Hprt*, and *Ubc*).

Vaginal cytology determination of estrus cycling

Vaginal lavages were obtained using a standard protocol[150]. Lavages were deposited to glass slides (VWR #48311-703) and left to dry for at least 24 hours. Vaginal cytology slides were stained for 30 seconds 1% Thionin (Alfa Aesar #A18192), in 20mM acetic acid (Sigma-Aldrich #695092-2.5L-GL), 0.36mM Sodium Hydroxide (Sigma-Aldrich #221465-500G) at pH 4.0. Excess thionin staining was washed twice in MilliQ water. Slides were dehydrated for 30 seconds in 70%, 95%, and 100% ethanol, then air dried overnight before microscopic analysis. Slides were viewed under a microscope at 20x magnification identify the estrus phase each mouse was in at the time of sample collection (**Supplementary Table S1C**).

Motif analysis in remodeled chromatin regions

To identify potential TFs regulating sex-specific aging phenotypes in macrophages, ATAC-seq and H3K4me3 peaks with age-related remodeling in only one sex were obtained (see above for criteria). Motif finding was performed using HOMER v5.1 'findMotifsGenome.pl' script[98], using all robustly detected metapeaks as enrichment background and the mm10 reference genome. We focused on results for enrichment of known motifs reported in "knownResults.txt". Top TF motifs corresponding to TF genes significantly regulated with female aging are shown in **Figure 6C, D**. All enriched motifs from our analyses are reported in **Supplementary Table S7A.** To confirm enrichment of Irf2-related binding motifs, Irf2 peaks (see below) were used with the same pipeline, and selected motifs are reported in **Supplementary Figure S6F**.

SCENIC analysis of regulon activity in single cell RNA-seq analysis

As an orthogonal method to evaluate candidate TF activity in aging female and male macrophages, we took advantage of macrophages identified in our scRNA-seq datasets (see above) and applied the SCENIC algorithm to our data[99]. We applied the SCENIC pipeline using R packages SCENIC v1.1.2-01, RcisTarget v1.6.0, GENIE3 v1.8.0 and AUCell v1.8.0 following the package tutorial. Specifically, SCT normalized UMI counts from a combined Seurat object

with macrophages transcriptomes from our 3 datasets were used as the input expression matrix. Mouse feather datasets for the mm10 assembly were downloaded from the SCENIC website (*i.e.* mm10__refseq-r80__500bp_up_and_100bp_down_tss.mc9nr.feather and mm10__refseq-r80__10kb_up_and_down_tss.mc9nr.feather). Computed TF regulon activities were obtained for 82 TFs in every cell, and we used a Wilcoxon rank-sum test approach to determine whether regulon activity was significantly impacted by aging in female or male macrophages (**Supplementary Table S6A**). Dot plots and violin plots were generated for TFs also identified from our bulk 'omic' data (**Supplementary Figure S6B, C**).

Irf2 protein level quantification using intracellular labeling and flow cytometry quantification

Cells were resuspended in 90µL of staining buffer and incubated with 10µL of FcR blocking reagent (Miltenyi Biotec #130-092-575) at 4 °C for 20 minutes. For MACS-purified peritoneal macrophage analysis, surface F4/80 staining was performed (to guarantee quantification of Irf2 expression solely on macrophages) by adding 2µL of anti-F4/80 antibody per sample, followed by a 10-minute incubation at 4 °C. Then, 2mL of resuspension buffer was added, and cells were centrifuged at 300g for 10 minutes to remove unbound antibodies. Supernatant were then removed, and cells were resuspended in 1mL of Foxp3 Fixation/Permeabilization working solution (Invitrogen #00-5523-00), pulse-vortexed, and incubated at 4 °C for 1 hour protected from light. Following fixation, 2 mL of 1x Permeabilization Buffer (Invitrogen #00-5523-00) was added, and samples were centrifuged at 600g for 5 minutes at room temperature. Supernatants were carefully decanted, leaving approximately 200µL, and cells were gently resuspended. To block nonspecific binding, 10µL normal rat serum was added, and samples were incubated at room temperature for 15 minutes. Each sample was split into 98µL aliquots for intracellular staining with 2µL of directly conjugated PE-IgG isotype control (Abcam #ab209478) or PE-Irf2 (Abcam #ab318372) antibodies, and incubated at 4 °C for 1 hour, protected from light. After staining, cells were washed twice with 2mL of 1x Permeabilization Buffer by centrifugation at 600g for 5 minutes at room temperature. Finally, cells were resuspended in eBioscience Flow Cytometry Staining Buffer (Invitrogen #00-4222-26). Stained cells median fluorescent intensity (MFI) was analyzed by flow cytometry on the Miltenyi Biotec MACSQuant Analyzer 10, and flow cytometry results

were processed using the FlowLogic V8 software. To obtain the TF expression level, non-specific background signal was removed by subtracting the MFI of IgG isotype control from the MFI of Irf2 for each specific cell sample (i.e. isolate for a single animal, or transduced cell aliquot)[151]. TF levels were then normalized dividing the median entire cohort per value to mitigate the impact of cohort-specific variation in fluorescence intensity. Raw flow cytometry data for aging, RAW264.7 *Irf2* KD, J774A.1 has been deposited to Figshare under 10.6084/m9.figshare.29285708, 10.6084/m9.figshare.29169947, and 10.6084/m9.figshare.29169959 respectively.

Active Motif FactorPath Irf2 ChIP-seq

Red-blood cell lysed bone marrow cells from 4 months old female C57BL/6JNia mice were differentiated into BMDMs in two independent biological replicates (pool of 2 animals per replicate) as above. For each replicate ChIP experiment, we plated 10 million BMDMs from an independent primary culture, which were fixed by adding 1:20 (v/v) ratio of freshly prepared formaldehyde solution (11% formaldehyde (Sigma-Aldrich #F8775-25ML), 100 mM NaCl,1 mM EDTA pH 8.0 (EMD Millipore #324506), and 50 mM HEPES pH = 8) to the cell culture media, followed by incubation for 15 min at room temperature. Fixation was stopped by adding 2.5 M glycine (Sigma-Aldrich #G7403-100G) solution at a 1:20 (v/v) ratio and incubating for 5 min at room temperature. Cells were collected by scraping on ice and spun down at 4°C 800g for 10 minutes. All subsequent steps were performed on ice. Cells were collected and washed twice with chilled PBS (Sigma-Aldrich #P4474-500ML) with 0.5% Igepal (Sigma-Aldrich #I8896-50ML). 1mM of phenylmethylsulfonyl fluoride (PMSF) (Sigma-Aldrich #P7626-250MG) was added to the second wash before pelleting. Cell pellets were snap-frozen on dry ice and sent to Active Motif for further processing.

Subsequent processing steps including chromatin extraction, fragmentation, antibody precipitation, input, and library preparation were performed by Active Motif using a ChIP validated antibody to IRF2 (Abcam #ab124744). Active motif generated ChIP-seq libraries from the ChIP-DNA and a pooled Input control library using a custom Illumina library type protocol on an automated system (Apollo 342, Wafergen Biosystems/Takara). ChIP-seq libraries were sequenced on Illumina NovaSeq 6000 as 75 nucleotides single-end reads. Demultiplexed FASTQ

files were provided by Active Motif, and the ChIP-seq FASTQ reads were deposited to SRA under Bioproject PRJNA1126274.

BMDM Irf2 ChIP-seq analysis

Single-end Irf2 ChIP-seq reads were mapped to the mm10 genome reference using bowtie1 v1.2.3[152]. After alignment, PCR duplicates were removed using the FIXSeq algorithm[153], as previously described[134]. We used MACS2 v2.2.7.1 to identify Irf2-bound regions in each of our 2 biological replicates[143]. Consensus peaks were then calculated using MSPC v5.5.0[154], which identified 339 reproducibly bound regions (**Supplementary Table S7A**). Peaks were annotated to the closest TSS using the HOMER 'annotatePeaks.pl' script[98] (**Supplementary Table S7B**). To compute functional enrichment for Irf2 target genes, we leveraged the 'GREAT' 4.0.4 tool[101], a tool specifically optimized to identify functional enrichment starting from genomic regions. We used the mm10 genome as the background for enrichment and all other options were left to default parameters. Results were exported as 'tsv', processed in R to filter significant enrichments with FDR < 5% and are reported in **Supplementary Table S7C, D**. We also used R packages ChIPSeeker v1.22.1[155] and TxDb.Mmusculus.UCSC.mm10.knownGene v3.10.0 to perform genomic distribution annotation of peaks (**Supplementary Figure S7G**), together with clusterProfiler v3.14.3 as an orthogonal approach for functional enrichment analysis of Irf2-bound regions (see results in **Supplementary Table S7E, F**).

To determine whether chromatin remodeling (*i.e.* changes in ATAC-seq or H3K4me3 CUT&RUN signal) may occur in female peritoneal macrophages with aging at Irf2 bound sites, we used R packages ChIPpeakAnno v3.20.1[156] to perform overlap analyses (**Supplementary Figure S7H**) and NGSplot v2.61[157] to generate signal plots (**Figure 7I**).

Data availability

Sequencing data has been deposited to the Sequence Read Archive, under Bioprojects PRJNA1094925, PRJNA1095555, PRJNA1096052, PRJNA1101936, PRJNA1126274, PRJNA1222371.

Raw flow cytometry data (10.6084/m9.figshare.28934213, 10.6084/m9.figshare.29169674, 10.6084/m9.figshare.29169737, 10.6084/m9.figshare.29169707,

10.6084/m9.figshare.28934198, 10.6084/m9.figshare.29169578, 10.6084/m9.figshare.29169581, 10.6084/m9.figshare.29169587, 10.6084/m9.figshare.29161955, 10.6084/m9.figshare.29169836, 10.6084/m9.figshare.29169821, 10.6084/m9.figshare.29169860, 10.6084/m9.figshare.29169821, 10.6084/m9.figshare.29169872, 10.6084/m9.figshare.29169899, 10.6084/m9.figshare.29285708, 10.6084/m9.figshare.29169947,10.6084/m9.figshare.29169959, and 10.6084/m9.figshare.29286278), microscopy images (10.6084/m9.figshare.29286194, 10.6084/m9.figshare.29286206), and Agilent Seahorse data (10.6084/m9.figshare.29169911, 10.6084/m9.figshare.29169920, 10.6084/m9.figshare.29169926) have been deposited to Figshare.

Code Availability

All R code for this study was run using R version 3.6.3. Genomic data processing scripts have been made available on the Benayoun lab GitHub repository at https://github.com/BenayounLaboratory/ Macrophage_SexDim_Aging.

Acknowledgements

We are grateful to Dr. Caleb Finch, Dr. Raphael Williams, Clayton Baker, Dr. Marc Vermulst, Sarah Shemtov, Allison Chae, Courtney Shen, Wyatt Web, Evelyn Navar, Emily K. Wang, Prakroothi S. Danthi, Amy Huang, Rochelle W. Lai, Guan J. Lai and Claire Chung for scientific insights and assistance during the preparation of this manuscript. We thank USC DAR veterinarians Dr. Lynlee M. Stevey-Rindenow and Dr. Bradley Ahrens for performing the ovariectomy and sham surgeries. We thank Hemal Mehta at the USC Leonard Davis school of Gerontology Seahorse core facility for helping run Seahorse experiments. We thank Dr. Didier Trono for providing the pMDLg/pRRE (Addgene #12251) and pRSV-Rev (Addgene #12253) plasmids. We thank Dr. Tannishtha Reya for providing VSV.G (Addgene #14888) plasmid. We thank Dr. Kenneth S. Korach for providing the B6N(Cg)-Esr1$^{tm4.2Ksk}$/*J* (*Esr1* KO) mice[94] (JAX #026176).

This work was supported by a Diana Jacobs Kalman/AFAR Scholarships for Research in the Biology of Aging, NIA T32 AG052374, and AthenaDAO student leader award to R.J.L.; USC Provost's Undergrad Research Fellowships to E.E.W., E.H.L., and C.R.; GCRLE-2020 post-doctoral fellowship from the Global Consortium for Reproductive Longevity and Equality at the Buck Institute, made possible by the Bia-Echo Foundation to M.K.; NIAID R01 AI134987 to H.S.G.; core vouchers from the USC Leonard Davis School of Gerontology, NIA R00 AG049934, Pew Biomedical Scholar award #00034120, an innovator grant from the Rose Hills foundation, the Kathleen Gilmore Biology of Aging research award, a generous gift from Dr. Eric Hennigan, and Hevolution grant HF-GRO-23-1199072-28 to B.A.B. The authors acknowledge the Center for Advanced Research Computing [CARC] at the University of Southern California for providing computing resources that contributed to the research results reported within this publication (URL: https://carc.usc.edu). The funders had no role in study design, data collection and analysis, decision to publish, or preparation of the manuscript.

Author contributions

R.J.L., N.S.K., and B.A.B. designed the study. R.J.L., N.S.K, A.P., performed live animal experiments. A.P. read vaginal cytology slides. R.J.L., S.C., M.K., L.A., I.Y.L., K.M., N.S.K., and B.A.B. dissected mouse tissues. R.J.L. and M.K. generated omics libraries. B.A.B. performed computational analyses. R.J.L. performed flow cytometry experiments. R.J.L.,

E.E.W., I.Y.L., C.R., J.J., and S.B. imaged and analyzed microscopy phagocytosis data. R.J.L., S.C., and A.X. performed phagocytosis flow cytometry and quantification analysis. R.J.L., S.C., and E.H.L. performed metabolic profiling experiments. R.J.L., A.X., and B.A.B analyzed Seahorse experiments. R.J.L., E.H.L, S.P., C.R., I.Y.L. performed RT-qPCR analyses. R.J.L., and S.C. perform intracellular Irf2 quantification. C.D.L. and H.S.G. contributed scientific insights to the project. R.J.L., S.C., and B.A.B. wrote the manuscript with input from all authors. All authors edited and commented on the final manuscript.

References

1 Shi, Y. *et al.* Sex difference in human diseases: mechanistic insights and clinical implications. *Signal Transduct Target Ther* **9**, 238, doi:10.1038/s41392-024-01929-7 (2024).

2 Lopez-Otin, C., Blasco, M. A., Partridge, L., Serrano, M. & Kroemer, G. Hallmarks of aging: An expanding universe. *Cell* **186**, 243-278, doi:10.1016/j.cell.2022.11.001 (2023).

3 Ostan, R. *et al.* Gender, aging and longevity in humans: an update of an intriguing/neglected scenario paving the way to a gender-specific medicine. *Clin Sci (Lond)* **130**, 1711-1725, doi:10.1042/CS20160004 (2016).

4 Kulminski, A. M. *et al.* Sex-specific health deterioration and mortality: the morbidity-mortality paradox over age and time. *Exp Gerontol* **43**, 1052-1057, doi:10.1016/j.exger.2008.09.007 (2008).

5 in *Sociality, Hierarchy, Health: Comparative Biodemography: A Collection of Papers The National Academies Collection: Reports funded by National Institutes of Health* (eds M. Weinstein & M. A. Lane) (2014).

6 Gordon, E. H. *et al.* Sex differences in frailty: A systematic review and meta-analysis. *Exp Gerontol* **89**, 30-40, doi:10.1016/j.exger.2016.12.021 (2017).

7 Appt, S. E. & Ethun, K. F. Reproductive aging and risk for chronic disease: Insights from studies of nonhuman primates. *Maturitas* **67**, 7-14, doi:10.1016/j.maturitas.2010.03.028 (2010).

8 Franceschi, C. & Campisi, J. Chronic inflammation (inflammaging) and its potential contribution to age-associated diseases. *J Gerontol A Biol Sci Med Sci* **69 Suppl 1**, S4-9, doi:10.1093/gerona/glu057 (2014).

9 Santoro, A., Bientinesi, E. & Monti, D. Immunosenescence and inflammaging in the aging process: age-related diseases or longevity? *Ageing Res Rev* **71**, 101422, doi:10.1016/j.arr.2021.101422 (2021).

10 Klein, S. L. & Flanagan, K. L. Sex differences in immune responses. *Nat Rev Immunol* **16**, 626-638, doi:10.1038/nri.2016.90 (2016).

11 Dunn, S. E., Perry, W. A. & Klein, S. L. Mechanisms and consequences of sex differences in immune responses. *Nat Rev Nephrol* **20**, 37-55, doi:10.1038/s41581-023-00787-w (2024).

12 McGill, C. J., White, O. S., Lu, R. J., Sampathkumar, N. K. & Benayoun, B. A. Sex-dimorphic gene regulation in murine macrophages across niches. *bioRxiv*, 2024.2012.2020.629843, doi:10.1101/2024.12.20.629843 (2024).

13 Flanagan, K. L., Fink, A. L., Plebanski, M. & Klein, S. L. Sex and Gender Differences in the Outcomes of Vaccination over the Life Course. *Annu Rev Cell Dev Biol* **33**, 577-599, doi:10.1146/annurev-cellbio-100616-060718 (2017).

14 Thompson, W. W. *et al.* Influenza-associated hospitalizations in the United States. *JAMA* **292**, 1333-1340, doi:10.1001/jama.292.11.1333 (2004).

15 Perrotta, F. *et al.* COVID-19 and the elderly: insights into pathogenesis and clinical decision-making. *Aging Clin Exp Res* **32**, 1599-1608, doi:10.1007/s40520-020-01631-y (2020).

16 Fairweather, D., Beetler, D. J., McCabe, E. J. & Lieberman, S. M. Mechanisms underlying sex differences in autoimmunity. *J Clin Invest* **134**, doi:10.1172/JCI180076 (2024).

17 Pang, W. W. *et al.* Human bone marrow hematopoietic stem cells are increased in frequency and myeloid-biased with age. *Proc Natl Acad Sci U S A* **108**, 20012-20017, doi:10.1073/pnas.1116110108 (2011).

18 Zhang, C. *et al.* Sex-dependent differences in hematopoietic stem cell aging and leukemogenic potential. *Oncogene* **44**, 64-78, doi:10.1038/s41388-024-03197-9 (2025).

19 Marquez, E. J. *et al.* Sexual-dimorphism in human immune system aging. *Nat Commun* **11**, 751, doi:10.1038/s41467-020-14396-9 (2020).

20 Qu, K. *et al.* Individuality and variation of personal regulomes in primary human T cells. *Cell Syst* **1**, 51-61, doi:10.1016/j.cels.2015.06.003 (2015).

21 Gal-Oz, S. T. *et al.* ImmGen report: sexual dimorphism in the immune system transcriptome. *Nat Commun* **10**, 4295, doi:10.1038/s41467-019-12348-6 (2019).

22 Huang, Z. *et al.* Effects of sex and aging on the immune cell landscape as assessed by single-cell transcriptomic analysis. *Proc Natl Acad Sci U S A* **118**, doi:10.1073/pnas.2023216118 (2021).

23 Barman, P. K. *et al.* Production of MHCII-expressing classical monocytes increases during aging in mice and humans. *Aging Cell* **21**, e13701, doi:10.1111/acel.13701 (2022).

24 Lu, R. J. *et al.* Multi-omic profiling of primary mouse neutrophils predicts a pattern of sex and age-related functional regulation. *Nat Aging* **1**, 715-733, doi:10.1038/s43587-021-00086-8 (2021).

25 Lavin, Y. *et al.* Tissue-resident macrophage enhancer landscapes are shaped by the local microenvironment. *Cell* **159**, 1312-1326, doi:10.1016/j.cell.2014.11.018 (2014).

26 Ginhoux, F. & Guilliams, M. Tissue-Resident Macrophage Ontogeny and Homeostasis. *Immunity* **44**, 439-449, doi:10.1016/j.immuni.2016.02.024 (2016).

27 Ross, E. A., Devitt, A. & Johnson, J. R. Macrophages: The Good, the Bad, and the Gluttony. *Front Immunol* **12**, 708186, doi:10.3389/fimmu.2021.708186 (2021).

28 Barrett, J. P., Costello, D. A., O'Sullivan, J., Cowley, T. R. & Lynch, M. A. Bone marrow-derived macrophages from aged rats are more responsive to inflammatory stimuli. *J Neuroinflammation* **12**, 67, doi:10.1186/s12974-015-0287-7 (2015).

29 Dube, C. T. *et al.* Age-Related Alterations in Macrophage Distribution and Function Are Associated With Delayed Cutaneous Wound Healing. *Front Immunol* **13**, 943159, doi:10.3389/fimmu.2022.943159 (2022).

30 Linehan, E. *et al.* Aging impairs peritoneal but not bone marrow-derived macrophage phagocytosis. *Aging Cell* **13**, 699-708, doi:10.1111/acel.12223 (2014).

31 Wong, C. K. *et al.* Aging Impairs Alveolar Macrophage Phagocytosis and Increases Influenza-Induced Mortality in Mice. *J Immunol* **199**, 1060-1068, doi:10.4049/jimmunol.1700397 (2017).

32 Li, Z. *et al.* Aging-Impaired Filamentous Actin Polymerization Signaling Reduces Alveolar Macrophage Phagocytosis of Bacteria. *J Immunol* **199**, 3176-3186, doi:10.4049/jimmunol.1700140 (2017).

33 Fix, D. K. *et al.* Disrupted macrophage metabolic reprogramming in aged soleus muscle during early recovery following disuse atrophy. *Aging Cell* **20**, e13448, doi:10.1111/acel.13448 (2021).

34 Kim, O. H. *et al.* Impaired phagocytosis of apoptotic cells causes accumulation of bone marrow-derived macrophages in aged mice. *BMB Rep* **50**, 43-48, doi:10.5483/bmbrep.2017.50.1.167 (2017).

35 Peradinovic, J. *et al.* Ageing-Induced Decline in Primary Myeloid Cell Phagocytosis Is Unaffected by Optineurin Insufficiency. *Biology (Basel)* **12**, doi:10.3390/biology12020240 (2023).

36 Lu, R. J., Wang, E. K. & Benayoun, B. A. Functional genomics of inflamm-aging and immunosenescence. *Brief Funct Genomics* **21**, 43-55, doi:10.1093/bfgp/elab009 (2022).

37 Mondal, S. & Rai, U. Sexual dimorphism in phagocytic activity of wall lizard's splenic macrophages and its control by sex steroids. *Gen Comp Endocrinol* **116**, 291-298, doi:10.1006/gcen.1999.7370 (1999).

38 Scotland, R. S., Stables, M. J., Madalli, S., Watson, P. & Gilroy, D. W. Sex differences in resident immune cell phenotype underlie more efficient acute inflammatory responses in female mice. *Blood* **118**, 5918-5927, doi:10.1182/blood-2011-03-340281 (2011).

39 Kang, S. *et al.* Microglia undergo sex-dimorphic transcriptional and metabolic rewiring during aging. *J Neuroinflammation* **21**, 150, doi:10.1186/s12974-024-03130-7 (2024).

40 Baker, C., Kim, M. & Benayoun, B. A. A researcher's guide to studying sex differences in immune aging. *Trends Mol Med*, doi:10.1016/j.molmed.2025.01.005 (2025).

41 Liu, M., Silva-Sanchez, A., Randall, T. D. & Meza-Perez, S. Specialized immune responses in the peritoneal cavity and omentum. *J Leukoc Biol* **109**, 717-729, doi:10.1002/JLB.5MIR0720-271RR (2021).

42 Okabe, Y. Immune Niche Within the Peritoneal Cavity. *Curr Top Microbiol Immunol* **434**, 123-134, doi:10.1007/978-3-030-86016-5_6 (2021).

43 Saris, J. *et al.* Peritoneal resident macrophages constitute an immunosuppressive environment in peritoneal metastasized colorectal cancer. *Nat Commun* **16**, 3669, doi:10.1038/s41467-025-58999-6 (2025).

44 Aliaghaei, M. & Haun, J. B. Optimization of Mechanical Tissue Dissociation Using an Integrated Microfluidic Device for Improved Generation of Single Cells Following Digestion. *Front Bioeng Biotechnol* **10**, 841046, doi:10.3389/fbioe.2022.841046 (2022).

45 Skinnider, M. A. *et al.* Cell type prioritization in single-cell data. *Nat Biotechnol* **39**, 30-34, doi:10.1038/s41587-020-0605-1 (2021).

46 Miller, S. A. *et al.* LSD1 and Aberrant DNA Methylation Mediate Persistence of Enteroendocrine Progenitors That Support BRAF-Mutant Colorectal Cancer. *Cancer Res* **81**, 3791-3805, doi:10.1158/0008-5472.CAN-20-3562 (2021).

47 Gautier, E. L. *et al.* Gata6 regulates aspartoacylase expression in resident peritoneal macrophages and controls their survival. *J Exp Med* **211**, 1525-1531, doi:10.1084/jem.20140570 (2014).

48 Mogilenko, D. A., Shchukina, I. & Artyomov, M. N. Immune ageing at single-cell resolution. *Nat Rev Immunol* **22**, 484-498, doi:10.1038/s41577-021-00646-4 (2022).

49 Davies, L. C. *et al.* A quantifiable proliferative burst of tissue macrophages restores homeostatic macrophage populations after acute inflammation. *Eur J Immunol* **41**, 2155-2164, doi:10.1002/eji.201141817 (2011).

50 Louwe, P. A. *et al.* Recruited macrophages that colonize the post-inflammatory peritoneal niche convert into functionally divergent resident cells. *Nat Commun* **12**, 1770, doi:10.1038/s41467-021-21778-0 (2021).

51 Kowalczyk, M. S. *et al.* Single-cell RNA-seq reveals changes in cell cycle and differentiation programs upon aging of hematopoietic stem cells. *Genome Res* **25**, 1860-1872, doi:10.1101/gr.192237.115 (2015).

52 Buenrostro, J. D., Giresi, P. G., Zaba, L. C., Chang, H. Y. & Greenleaf, W. J. Transposition of native chromatin for fast and sensitive epigenomic profiling of open chromatin, DNA-binding proteins and nucleosome position. *Nat Methods* **10**, 1213-1218, doi:10.1038/nmeth.2688 (2013).

53 Corces, M. R. *et al.* An improved ATAC-seq protocol reduces background and enables interrogation of frozen tissues. *Nat Methods* **14**, 959-962, doi:10.1038/nmeth.4396 (2017).

54 Skene, P. J. & Henikoff, S. An efficient targeted nuclease strategy for high-resolution mapping of DNA binding sites. *Elife* **6**, doi:10.7554/eLife.21856 (2017).

55 Ferraye, L., Nieucel, M., Savignac, M., Chaumeil, J. & Guery, J. C. The Inactive X Chromosome: A Genetic Driver of Female-Biased Rheumatic Autoimmune Disorders? *Eur J Immunol* **55**, e202451331, doi:10.1002/eji.202451331 (2025).

56 Zylicz, J. J. *et al.* The Implication of Early Chromatin Changes in X Chromosome Inactivation. *Cell* **176**, 182-197 e123, doi:10.1016/j.cell.2018.11.041 (2019).

57 Loda, A. & Heard, E. Xist RNA in action: Past, present, and future. *PLoS Genet* **15**, e1008333, doi:10.1371/journal.pgen.1008333 (2019).

58 Hajdarovic, K. H. *et al.* Single-cell analysis of the aging female mouse hypothalamus. *Nat Aging* **2**, 662-678, doi:10.1038/s43587-022-00246-4 (2022).

59 Gadek, M. *et al.* Aging activates escape of the silent X chromosome in the female mouse hippocampus. *Sci Adv* **11**, eads8169, doi:10.1126/sciadv.ads8169 (2025).

60 Zhou, G. *et al.* NetworkAnalyst 3.0: a visual analytics platform for comprehensive gene expression profiling and meta-analysis. *Nucleic Acids Res* **47**, W234-W241, doi:10.1093/nar/gkz240 (2019).

61 Breuer, K. *et al.* InnateDB: systems biology of innate immunity and beyond--recent updates and continuing curation. *Nucleic Acids Res* **41**, D1228-1233, doi:10.1093/nar/gks1147 (2013).

62 Lee, K. A., Flores, R. R., Jang, I. H., Saathoff, A. & Robbins, P. D. Immune Senescence, Immunosenescence and Aging. *Front Aging* **3**, 900028, doi:10.3389/fragi.2022.900028 (2022).

63 Russell, D. G., Huang, L. & VanderVen, B. C. Immunometabolism at the interface between macrophages and pathogens. *Nat Rev Immunol* **19**, 291-304, doi:10.1038/s41577-019-0124-9 (2019).

64 Haney, M. S. *et al.* Identification of phagocytosis regulators using magnetic genome-wide CRISPR screens. *Nat Genet* **50**, 1716-1727, doi:10.1038/s41588-018-0254-1 (2018).

65 Pluvinage, J. V. *et al.* CD22 blockade restores homeostatic microglial phagocytosis in ageing brains. *Nature* **568**, 187-192, doi:10.1038/s41586-019-1088-4 (2019).

66 Liberzon, A. *et al.* Molecular signatures database (MSigDB) 3.0. *Bioinformatics* **27**, 1739-1740, doi:10.1093/bioinformatics/btr260 (2011).

67 Das, A. *et al.* High-Resolution Mapping and Dynamics of the Transcriptome, Transcription Factors, and Transcription Co-Factor Networks in Classically and Alternatively Activated Macrophages. *Front Immunol* **9**, 22, doi:10.3389/fimmu.2018.00022 (2018).

68 Martin, C. J., Peters, K. N. & Behar, S. M. Macrophages clean up: efferocytosis and microbial control. *Curr Opin Microbiol* **17**, 17-23, doi:10.1016/j.mib.2013.10.007 (2014).

69 Hirayama, D., Iida, T. & Nakase, H. The Phagocytic Function of Macrophage-Enforcing Innate Immunity and Tissue Homeostasis. *Int J Mol Sci* **19**, doi:10.3390/ijms19010092 (2017).

70 Murray, P. J. Macrophage Polarization. *Annu Rev Physiol* **79**, 541-566, doi:10.1146/annurev-physiol-022516-034339 (2017).

71 Lu, R., Sampathkumar, N. K. & Benayoun, B. A. Measuring Phagocytosis in Bone Marrow-Derived Macrophages and Peritoneal Macrophages with Aging. *Methods Mol Biol* **2144**, 161-170, doi:10.1007/978-1-0716-0592-9_14 (2020).

72 Ghosn, E. E. *et al*. Two physically, functionally, and developmentally distinct peritoneal macrophage subsets. *Proc Natl Acad Sci U S A* **107**, 2568-2573, doi:10.1073/pnas.0915000107 (2010).

73 Cassado Ados, A., D'Imperio Lima, M. R. & Bortoluci, K. R. Revisiting mouse peritoneal macrophages: heterogeneity, development, and function. *Front Immunol* **6**, 225, doi:10.3389/fimmu.2015.00225 (2015).

74 Goswami, D. G. *et al*. Large Peritoneal Macrophages and Transitional Premonocytes Promote Survival during Abdominal Sepsis. *Immunohorizons* **5**, 994-1007, doi:10.4049/immunohorizons.2100086 (2021).

75 Jayakumar, P., Laganson, A. & Deng, M. GATA6(+) Peritoneal Resident Macrophage: The Immune Custodian in the Peritoneal Cavity. *Front Pharmacol* **13**, 866993, doi:10.3389/fphar.2022.866993 (2022).

76 Dillon, S. *et al*. Yeast zymosan, a stimulus for TLR2 and dectin-1, induces regulatory antigen-presenting cells and immunological tolerance. *J Clin Invest* **116**, 916-928, doi:10.1172/JCI27203 (2006).

77 Viola, A., Munari, F., Sanchez-Rodriguez, R., Scolaro, T. & Castegna, A. The Metabolic Signature of Macrophage Responses. *Front Immunol* **10**, 1462, doi:10.3389/fimmu.2019.01462 (2019).

78 Van den Bossche, J., Baardman, J. & de Winther, M. P. Metabolic Characterization of Polarized M1 and M2 Bone Marrow-derived Macrophages Using Real-time Extracellular Flux Analysis. *J Vis Exp*, doi:10.3791/53424 (2015).

79 Chavez-Galan, L., Olleros, M. L., Vesin, D. & Garcia, I. Much More than M1 and M2 Macrophages, There are also CD169(+) and TCR(+) Macrophages. *Front Immunol* **6**, 263, doi:10.3389/fimmu.2015.00263 (2015).

80 Yao, Y., Xu, X. H. & Jin, L. Macrophage Polarization in Physiological and Pathological Pregnancy. *Front Immunol* **10**, 792, doi:10.3389/fimmu.2019.00792 (2019).

81 Furgiuele, S. *et al*. Dealing with Macrophage Plasticity to Address Therapeutic Challenges in Head and Neck Cancers. *Int J Mol Sci* **23**, doi:10.3390/ijms23126385 (2022).

82 Kim, Y. J., Tamadon, A., Park, H. T., Kim, H. & Ku, S. Y. The role of sex steroid hormones in the pathophysiology and treatment of sarcopenia. *Osteoporos Sarcopenia* **2**, 140-155, doi:10.1016/j.afos.2016.06.002 (2016).

83 Loiola, R. A., Wickstead, E. S., Solito, E. & McArthur, S. Estrogen Promotes Pro-resolving Microglial Behavior and Phagocytic Cell Clearance Through the Actions of Annexin A1. *Front Endocrinol (Lausanne)* **10**, 420, doi:10.3389/fendo.2019.00420 (2019).

84 Sun, Z. *et al*. 17beta-Estradiol promotes LC3B-associated phagocytosis in trained immunity of female mice against sepsis. *Int J Biol Sci* **17**, 460-474, doi:10.7150/ijbs.53050 (2021).

85 Ribas, V. *et al*. Myeloid-specific estrogen receptor alpha deficiency impairs metabolic homeostasis and accelerates atherosclerotic lesion development. *Proc Natl Acad Sci U S A* **108**, 16457-16462, doi:10.1073/pnas.1104533108 (2011).

86 Cora, M. C., Kooistra, L. & Travlos, G. Vaginal Cytology of the Laboratory Rat and Mouse: Review and Criteria for the Staging of the Estrous Cycle Using Stained Vaginal Smears. *Toxicol Pathol* **43**, 776-793, doi:10.1177/0192623315570339 (2015).

87 Zysow, B. R., Kauser, K., Lawn, R. M. & Rubanyi, G. M. Effects of estrus cycle, ovariectomy, and treatment with estrogen, tamoxifen, and progesterone on apolipoprotein(a) gene expression in transgenic mice. *Arterioscler Thromb Vasc Biol* **17**, 1741-1745, doi:10.1161/01.atv.17.9.1741 (1997).

88 Gordon, M. N., Osterburg, H. H., May, P. C. & Finch, C. E. Effective oral administration of 17 beta-estradiol to female C57BL/6J mice through the drinking water. *Biol Reprod* **35**, 1088-1095, doi:10.1095/biolreprod35.5.1088 (1986).

89 Kohama, S. G., Anderson, C. P., Osterburg, H. H., May, P. C. & Finch, C. E. Oral administration of estradiol to young C57BL/6J mice induces age-like neuroendocrine dysfunctions in the regulation of estrous cycles. *Biol Reprod* **41**, 227-232, doi:10.1095/biolreprod41.2.227 (1989).

90 Rossouw, J. E. *et al.* Risks and benefits of estrogen plus progestin in healthy postmenopausal women: principal results From the Women's Health Initiative randomized controlled trial. *JAMA* **288**, 321-333, doi:10.1001/jama.288.3.321 (2002).

91 Frick, K. M. Estrogens and age-related memory decline in rodents: what have we learned and where do we go from here? *Horm Behav* **55**, 2-23, doi:10.1016/j.yhbeh.2008.08.015 (2009).

92 Lung, D. K., Reese, R. M. & Alarid, E. T. Intrinsic and Extrinsic Factors Governing the Transcriptional Regulation of ESR1. *Horm Cancer* **11**, 129-147, doi:10.1007/s12672-020-00388-0 (2020).

93 Saliba, A. E., Westermann, A. J., Gorski, S. A. & Vogel, J. Single-cell RNA-seq: advances and future challenges. *Nucleic Acids Res* **42**, 8845-8860, doi:10.1093/nar/gku555 (2014).

94 Hewitt, S. C. *et al.* Biological and biochemical consequences of global deletion of exon 3 from the ER alpha gene. *FASEB J* **24**, 4660-4667, doi:10.1096/fj.10-163428 (2010).

95 Pepe, G. *et al.* Self-renewal and phenotypic conversion are the main physiological responses of macrophages to the endogenous estrogen surge. *Sci Rep* **7**, 44270, doi:10.1038/srep44270 (2017).

96 Lee, T. I. & Young, R. A. Transcriptional regulation and its misregulation in disease. *Cell* **152**, 1237-1251, doi:10.1016/j.cell.2013.02.014 (2013).

97 Hu, H. *et al.* AnimalTFDB 3.0: a comprehensive resource for annotation and prediction of animal transcription factors. *Nucleic Acids Res* **47**, D33-D38, doi:10.1093/nar/gky822 (2019).

98 Heinz, S. *et al.* Simple combinations of lineage-determining transcription factors prime cis-regulatory elements required for macrophage and B cell identities. *Mol Cell* **38**, 576-589, doi:10.1016/j.molcel.2010.05.004 (2010).

99 Aibar, S. *et al.* SCENIC: single-cell regulatory network inference and clustering. *Nature Methods* **14**, 1083-1086, doi:10.1038/nmeth.4463 (2017).

100 Mastrototaro, G. *et al.* TBL1XR1 Ensures Balanced Neural Development Through NCOR Complex-Mediated Regulation of the MAPK Pathway. *Front Cell Dev Biol* **9**, 641410, doi:10.3389/fcell.2021.641410 (2021).

101 McLean, C. Y. *et al.* GREAT improves functional interpretation of cis-regulatory regions. *Nat Biotechnol* **28**, 495-501, doi:10.1038/nbt.1630 (2010).

102 Wang, Q. *et al.* Exploring Epigenomic Datasets by ChIPseeker. *Curr Protoc* **2**, e585, doi:10.1002/cpz1.585 (2022).

103 Yamamoto, H., Lamphier, M. S., Fujita, T., Taniguchi, T. & Harada, H. The oncogenic transcription factor IRF-2 possesses a transcriptional repression and a latent activation domain. *Oncogene* **9**, 1423-1428 (1994).

104 Nguyen, H., Mustafa, A., Hiscott, J. & Lin, R. Transcription factor IRF-2 exerts its oncogenic phenotype through the DNA binding/transcription repression domain. *Oncogene* **11**, 537-544 (1995).

105 Huang, S. *et al.* TM6SF1 suppresses the progression of lung adenocarcinoma and M2 macrophage polarization by inactivating the PI3K/AKT/mtor pathway. *Biochem Biophys Res Commun* **718**, 149983, doi:10.1016/j.bbrc.2024.149983 (2024).

106 Lai, J. H. *et al.* USP18 induction regulates immunometabolism to attenuate M1 signal-polarized macrophages and enhance IL-4-polarized macrophages in systemic lupus erythematosus. *Clin Immunol* **265**, 110285, doi:10.1016/j.clim.2024.110285 (2024).

107 Chen, G., Chen, X., Duan, X., Zhang, R. & Bai, C. Unraveling the roles of IFIT3 gene and immune-metabolic pathways in psoriasis: a bioinformatics exploration for diagnostic markers and therapeutic targets. *Front Mol Biosci* **11**, 1439837, doi:10.3389/fmolb.2024.1439837 (2024).

108 Ocanas, S. R. *et al.* Microglial senescence contributes to female-biased neuroinflammation in the aging mouse hippocampus: implications for Alzheimer's disease. *J Neuroinflammation* **20**, 188, doi:10.1186/s12974-023-02870-2 (2023).

109 Blommaert, E. *et al.* Mutations in MAGT1 lead to a glycosylation disorder with a variable phenotype. *Proc Natl Acad Sci U S A* **116**, 9865-9870, doi:10.1073/pnas.1817815116 (2019).

110 Matsuda-Lennikov, M. *et al.* Magnesium transporter 1 (MAGT1) deficiency causes selective defects in N-linked glycosylation and expression of immune-response genes. *J Biol Chem* **294**, 13638-13656, doi:10.1074/jbc.RA119.008903 (2019).

111 He, J. *et al.* Multi-targeted kinase inhibition alleviates mTOR inhibitor resistance in triple-negative breast cancer. *Breast Cancer Res Treat* **178**, 263-274, doi:10.1007/s10549-019-05380-z (2019).

112 He, L., Cho, S. & Blenis, J. mTORC1, the maestro of cell metabolism and growth. *Genes Dev* **39**, 109-131, doi:10.1101/gad.352084.124 (2025).

113 Panwar, V. *et al.* Multifaceted role of mTOR (mammalian target of rapamycin) signaling pathway in human health and disease. *Signal Transduct Target Ther* **8**, 375, doi:10.1038/s41392-023-01608-z (2023).

114 Krajcovic, M., Krishna, S., Akkari, L., Joyce, J. A. & Overholtzer, M. mTOR regulates phagosome and entotic vacuole fission. *Mol Biol Cell* **24**, 3736-3745, doi:10.1091/mbc.E13-07-0408 (2013).

115 Byles, V. *et al.* The TSC-mTOR pathway regulates macrophage polarization. *Nat Commun* **4**, 2834, doi:10.1038/ncomms3834 (2013).

116 Kakugawa, S. *et al.* Mitogen-activated protein kinase-activated kinase RSK2 plays a role in innate immune responses to influenza virus infection. *J Virol* **83**, 2510-2517, doi:10.1128/JVI.02416-08 (2009).

117 Wculek, S. K., Dunphy, G., Heras-Murillo, I., Mastrangelo, A. & Sancho, D. Metabolism of tissue macrophages in homeostasis and pathology. *Cell Mol Immunol* **19**, 384-408, doi:10.1038/s41423-021-00791-9 (2022).

118 Cho, L. *et al.* Rethinking Menopausal Hormone Therapy: For Whom, What, When, and How Long? *Circulation* **147**, 597-610, doi:10.1161/CIRCULATIONAHA.122.061559 (2023).

119 Lobo, R. A. Menopause and stroke and the effects of hormonal therapy. *Climacteric* **10 Suppl 2**, 27-31, doi:10.1080/13697130701550903 (2007).

120 Baker, C. & Benayoun, B. A. Menopause Is More Than Just Loss of Fertility. *Public Policy Aging Rep* **33**, 113-119, doi:10.1093/ppar/prad023 (2023).

121 Finch, C. E. The menopause and aging, a comparative perspective. *J Steroid Biochem Mol Biol* **142**, 132-141, doi:10.1016/j.jsbmb.2013.03.010 (2014).

122 Wang, L. *et al.* The multiple roles of interferon regulatory factor family in health and disease. *Signal Transduct Target Ther* **9**, 282, doi:10.1038/s41392-024-01980-4 (2024).

123 Zuo, J. *et al.* Glycolysis Rate-Limiting Enzymes: Novel Potential Regulators of Rheumatoid Arthritis Pathogenesis. *Front Immunol* **12**, 779787, doi:10.3389/fimmu.2021.779787 (2021).

124 Kohama, S. G., Brown, S. A., Finch, C. E. & McNeill, T. H. Chronic estradiol administration did not cause loss of hypothalamic LHRH or TIDA neurons in young or middle-aged C57BL/6J mice. *Brain Res* **574**, 341-344, doi:10.1016/0006-8993(92)90838-z (1992).

125 Zheng, G. X. *et al.* Massively parallel digital transcriptional profiling of single cells. *Nat Commun* **8**, 14049, doi:10.1038/ncomms14049 (2017).

126 Roelli, P., Flynn, B. & Gui, G. Hoohm/CITE-seq-Count: 1.4.2. *Zenodo*, doi:10.5281/zenodo.2590196 (2019).

127 Team, R. C. *R: A language and environment for statistical computing.*, <https://www.R-project.org/> (2022).

128 Satija, R., Farrell, J. A., Gennert, D., Schier, A. F. & Regev, A. Spatial reconstruction of single-cell gene expression data. *Nat Biotechnol* **33**, 495-502, doi:10.1038/nbt.3192 (2015).

129 Hao, Y. *et al.* Integrated analysis of multimodal single-cell data. *Cell* **184**, 3573-3587 e3529, doi:10.1016/j.cell.2021.04.048 (2021).

130 Young, M. D. & Behjati, S. SoupX removes ambient RNA contamination from droplet-based single-cell RNA sequencing data. *Gigascience* **9**, doi:10.1093/gigascience/giaa151 (2020).

131 McGinnis, C. S., Murrow, L. M. & Gartner, Z. J. DoubletFinder: Doublet Detection in Single-Cell RNA Sequencing Data Using Artificial Nearest Neighbors. *Cell Syst* **8**, 329-337 e324, doi:10.1016/j.cels.2019.03.003 (2019).

132 Aran, D. *et al.* Reference-based analysis of lung single-cell sequencing reveals a transitional profibrotic macrophage. *Nat Immunol* **20**, 163-172, doi:10.1038/s41590-018-0276-y (2019).

133 Heng, T. S., Painter, M. W. & Immunological Genome Project, C. The Immunological Genome Project: networks of gene expression in immune cells. *Nat Immunol* **9**, 1091-1094, doi:10.1038/ni1008-1091 (2008).

134 Benayoun, B. A. *et al.* Remodeling of epigenome and transcriptome landscapes with aging in mice reveals widespread induction of inflammatory responses. *Genome Res* **29**, 697-709, doi:10.1101/gr.240093.118 (2019).

135 Squair, J. W., Skinnider, M. A., Gautier, M., Foster, L. J. & Courtine, G. Prioritization of cell types responsive to biological perturbations in single-cell data with Augur. *Nat Protoc* **16**, 3836-3873, doi:10.1038/s41596-021-00561-x (2021).

136 Hansen, K. D., Brenner, S. E. & Dudoit, S. Biases in Illumina transcriptome sequencing caused by random hexamer priming. *Nucleic Acids Res* **38**, e131, doi:10.1093/nar/gkq224 (2010).

137 Dobin, A. *et al.* STAR: ultrafast universal RNA-seq aligner. *Bioinformatics* **29**, 15-21, doi:10.1093/bioinformatics/bts635 (2013).

138 Liao, Y., Smyth, G. K. & Shi, W. featureCounts: an efficient general purpose program for assigning sequence reads to genomic features. *Bioinformatics* **30**, 923-930, doi:10.1093/bioinformatics/btt656 (2014).

139 Love, M. I., Huber, W. & Anders, S. Moderated estimation of fold change and dispersion for RNA-seq data with DESeq2. *Genome Biol* **15**, 550, doi:10.1186/s13059-014-0550-8 (2014).

140 Gaspar, J. M. NGmerge: merging paired-end reads via novel empirically-derived models of sequencing errors. *BMC Bioinformatics* **19**, 536, doi:10.1186/s12859-018-2579-2 (2018).

141 Langmead, B. & Salzberg, S. L. Fast gapped-read alignment with Bowtie 2. *Nat Methods* **9**, 357-359, doi:10.1038/nmeth.1923 (2012).

142 Li, H. *et al.* The Sequence Alignment/Map format and SAMtools. *Bioinformatics* **25**, 2078-2079, doi:10.1093/bioinformatics/btp352 (2009).

143 Gaspar, J. M. Improved peak-calling with MACS2. *bioRxiv*, 496521, doi:10.1101/496521 (2018).

144 Ross-Innes, C. S. *et al.* Differential oestrogen receptor binding is associated with clinical outcome in breast cancer. *Nature* **481**, 389-393, doi:10.1038/nature10730 (2012).

145 Subramanian, A. *et al.* Gene set enrichment analysis: A knowledge-based approach for interpreting genome-wide expression profiles. *Proceedings of the National Academy of Sciences* **102**, 15545, doi:10.1073/pnas.0506580102 (2005).

146 Amend, S. R., Valkenburg, K. C. & Pienta, K. J. Murine Hind Limb Long Bone Dissection and Bone Marrow Isolation. *J Vis Exp*, doi:10.3791/53936 (2016).

147 Schneider, C. A., Rasband, W. S. & Eliceiri, K. W. NIH Image to ImageJ: 25 years of image analysis. *Nat Methods* **9**, 671-675, doi:10.1038/nmeth.2089 (2012).

148 Price, J. & Verner, K. Puromycin inhibits protein import into mitochondria by interfering with an intramitochondrial ATP-dependent reaction. *Biochim Biophys Acta* **1150**, 89-97, doi:10.1016/0005-2736(93)90125-j (1993).

149 Green, M. R. & Sambrook, J. *Molecular cloning : a laboratory manual*. 4th ed. edn, (Cold Spring Harbor Laboratory Press, 2012).

150 McLean, A. C., Valenzuela, N., Fai, S. & Bennett, S. A. Performing vaginal lavage, crystal violet staining, and vaginal cytological evaluation for mouse estrous cycle staging identification. *J Vis Exp*, e4389, doi:10.3791/4389 (2012).

151 Manso, B. A. & Medina, K. L. Standardized flow-cytometry-based protocol to simultaneously measure transcription factor levels. *STAR Protoc* **2**, 100485, doi:10.1016/j.xpro.2021.100485 (2021).

152 Langmead, B., Trapnell, C., Pop, M. & Salzberg, S. L. Ultrafast and memory-efficient alignment of short DNA sequences to the human genome. *Genome Biology* **10**, R25, doi:10.1186/gb-2009-10-3-r25 (2009).

153 Hashimoto, T. B., Edwards, M. D. & Gifford, D. K. Universal count correction for high-throughput sequencing. *PLoS Comput Biol* **10**, e1003494, doi:10.1371/journal.pcbi.1003494 (2014).

154 Jalili, V., Cremona, M. A. & Palluzzi, F. Rescuing biologically relevant consensus regions across replicated samples. *BMC Bioinformatics* **24**, 240, doi:10.1186/s12859-023-05340-x (2023).

155 Yu, G., Wang, L.-G. & He, Q.-Y. ChIPseeker: an R/Bioconductor package for ChIP peak annotation, comparison and visualization. *Bioinformatics* **31**, 2382-2383, doi:10.1093/bioinformatics/btv145 (2015).

156 Zhu, L. J. *et al*. ChIPpeakAnno: a Bioconductor package to annotate ChIP-seq and ChIP-chip data. *BMC Bioinformatics* **11**, 237, doi:10.1186/1471-2105-11-237 (2010).

157 Shen, L., Shao, N., Liu, X. & Nestler, E. ngs.plot: Quick mining and visualization of next-generation sequencing data by integrating genomic databases. *BMC Genomics* **15**, 284, doi:10.1186/1471-2164-15-284 (2014).

Legends to figures

Figure 1. Peritoneal macrophages are the most impacted cell type in the peritoneal cavity niche as a function of age and biological sex.

(**A**) Experimental scheme illustrating age-based cell profiling in mouse peritoneal lavage. (**B**) Uniform Manifold Approximation and Projection (UMAP) visualization of unsupervised clustering of peritoneal lavage cells. (**C**) UMAP representation of AUGUR area under the curve (AUC) scores for peritoneal lavage immune cell populations. (**D**) Boxplots of peritoneal cell composition quantified by scRNA-seq; n = 8 libraries per sex and age; 4 independent cohorts in 3 independent datasets. (**E**) Boxplots of peritoneal cell composition quantified by flow cytometry; n ≥ 25 per sex and age (6 independent cohorts). (**F**) Boxplots of peritoneal immune lavage cell number calculated by the proportion obtained from flow cytometry and total peritoneal lavage cell count; n ≥ 25 per sex and age (6 independent cohorts). For boxplots in panels (**D-F**), circles/squares represent NIA/JAX mice, respectively. Significance in non-parametric two-sided Wilcoxon rank-sum tests are reported in **D-F**. The center line of the box plots represents the sample median, the box limits consist of the 25th and 75th percentiles, the whiskers span 1.5x the interquartile range.

Figure 2. The peritoneal macrophage transcriptome and epigenome shows sex-dimorphic remodeling with aging.

(**A**) Experimental scheme of murine peritoneal macrophage 'omics' profiling. (**B**) Multidimensional scaling (MDS) plot of transcriptomic profiles, indicating distinct transcriptomic aging patterns between sexes. (**C**) MDS plot of chromatin accessibility profiles by ATAC-seq. (**D**) MDS plot of H3K4me3 profiles. (**E**) Scatterplot of age-related changes in peritoneal macrophage transcriptomes in female vs. males, reported as DESeq2 $\log_2$ fold changes per month. 284 Male-specific (blue) and 234 female-specific (pink) aging-regulated genes (Transcriptome-wide Spearman Rho = 0.288). (**F**) Scatterplot of age-related changes in peritoneal macrophage ATAC-seq accessible regions in female vs. males, reported as DESeq2 $\log_2$ fold changes per month. 1044 Male-specific (blue) and 2825 female-specific (pink) regions (Genome-wide Spearman Rho = 0.232). (**G**) Scatterplot of age-related changes in peritoneal macrophage H3K4me3 signal in female vs. males, reported as DESeq2 $\log_2$ fold changes per month. 131 male-specific (blue) and 1699 female-specific (pink) marks (Genome-wide Spearman Rho = 0.329). (**H**) Heatmap of male-specific aging gene expression changes by RNA-seq. (**I**) Heatmap of female-specific aging gene expression changes by RNA-seq. (**J**) Heatmap of male-specific aging chromatin accessibility changes by ATAC-seq. (**K**) Heatmap of female-specific aging chromatin accessibility changes by ATAC-seq. (**L**) Heatmap of male-specific aging H3K4me3 peak intensity by H3K4me3 CUT&RUN. (**M**) Heatmap of female-specific H3K4me3 peak intensity by H3K4me3 CUT&RUN.

Figure 3. Peritoneal macrophages show sex-dimorphic functional enrichments at the transcriptomic and epigenomic levels.

(**A**, **B**) NetworkAnalyst putative PPI network of genes changing with age in female (**A**) and male (**B**) peritoneal macrophages using IMEx network information. (**C**, **D**, **E**) Top 5 sex-dimorphic GSEA enrichments for aging in each sex for RNA-seq (**C**), ATAC-seq (**D**), and H3K4me3 CUT&RUN (**E**). (**F**) GSEA of CRISPR-Cas9 phagocytosis regulators from screens in aging female and male peritoneal macrophages. (**G**) GSEA of metabolic gene sets from MSigDB Hallmarks in aging female and male peritoneal macrophages. (**H**) GSEA of M1/M2 polarization genes in aging female and male peritoneal macrophages. NES: Normalized Enrichment Score. FDR: False Discovery Rate.

Figure 4. Peritoneal macrophages show female-specific remodeling of phagocytosis capacity and metabolic preferences with aging.

(**A**) Experimental scheme of murine peritoneal macrophage purification and functional analysis. (**B**) Representative microscopy image showing a phagocytosis event by young old male and female MACS-purified peritoneal macrophages engulfing Zymosan bioparticles. Blue = DAPI, Green = Zymosan bioparticles, Scale bar: 200μm. (**C**) Phagocytosis quantification of phagocytosis images from young old male and female peritoneal macrophages. The phagocytosis index is calculated by dividing phagocytosing cells by the total number of imaged cells. Due to cohort-to-cohort variation, values are normalized to the median value of each independent experiment. Animals from 5 independent cohorts (3 from NIA, 2 from JAX). Young females n = 21, old females n = 18, young males n = 22, and old males n = 20 (variation due to animal death prior to experimental day). (**D**) Flow cytometry phagocytosis quantification of peritoneal macrophage. Each point represents one animal. Animals from 6 independent cohorts (3 from NIA, 3 from JAX). Circles/squares represent NIA/JAX mice, respectively Samples with < 5000 F4/80^{+} events or < 75% F4/80^{+} purity were excluded from the analysis. (**E**) Venn diagram for CRISPR-Cas9 phagocytosis regulators and female-specific down-regulated genes according to DESeq2 at FDR < 5% and < 10%. (**F**) Lentiviral shRNA phagocytosis regulator screen experimental scheme. (**G**) Mini shRNA screen of RAW264.7 phagocytosis capacity using flow cytometry. The horizontal red line in the panel shows the median control value in the relative phagocytosis index of the macrophage. Dark green/light green for sh1/sh2 samples. Significance in non-parametric one-sided Wilcoxon rank-sum tests were reported (Hypothesis: same regulation direction as aging). (**H**) Experimental scheme of aging bone marrow-derived macrophage seahorse. (**I**) Representative normalized extracellular acidification rate (ECAR) mpH/min/DNA from 1 cohort of animals. (**J**) Glycolysis quantification using Seahorse (n = 15 for young old females and males; animals from 3 independent NIA cohorts). (**K**) Glycolysis quantification using Lactate-Glo (n = 18 for young males, n = 18 for young females, n = 17 for old males, and n = 17 for old females; animals from 5 independent cohorts (3 from NIA, 2 from JAX). For boxplots in panels (**C-D**, **J-H**), circles/squares represent NIA/JAX mice, respectively. Significance in non-parametric two-sided Wilcoxon rank-sum tests were reported. (**C-D**, **G**, **J-H**) The center line of the box plots represents the sample median, the box limits consist of the 25th and 75th percentiles, the whiskers span 1.5x the interquartile range.

2160

Figure 5. Sustained estrogen signaling is required to maintain youthful peritoneal macrophage transcriptomes and phagocytic capacity, but not metabolic preferences.

(**A**) Experimental scheme outlining the analysis of OVX mice. (**B**) Multi-dimensional scaling (MDS) analysis of gene expression profiles from Sham and OVX mice. (**C**) GSEA of OVX-regulated genes in the aging female peritoneal macrophage transcriptome. (**D**) Boxplot of phagocytosis quantification of peritoneal macrophages in Sham and OVX mice using flow cytometry (n = 11 for Sham, n = 12 for OVX; animals from 3 independent cohorts). (**E**) Boxplot of glycolysis quantification of peritoneal macrophages in Sham and OVX mice (n = 12 for Sham, n = 11 for OVX; 2 independent cohorts). (**F**) Experimental scheme describing late-life short-term 17β-estradiol (E2) supplementation in female mice. (**G**) MDS analysis of gene expression profiles in young females, old females, and E2-treated old females; n = 5 for young females, n = 5 for old females, n = 4 for E2-treated old females. (**H**) GSEA of E2-regulated genes in old female macrophages in the aging female peritoneal macrophage transcriptome. (**I**) Boxplot of phagocytosis of peritoneal macrophages in young females, old females, and E2-treated old females (n = 13 for young females, n = 13 for old females, n = 14 for E2-treated old females; animals from 3 independent cohorts). (**J**) Boxplot of glycolysis quantification of peritoneal macrophages in young females, old females, and E2-treated old females (n = 14 for young females, old females, and E2-treated old females; animals from 3 independent cohorts). (**K**) Experimental scheme for *Esr1* knockout (KO) mice. (**L**) MDS analysis of gene expression profiles in WT and *Esr1* KO mice (n = 5 for WT, n = 6 for *Esr1* KO). (**M**) GSEA of *Esr1* KO-regulated genes in the aging female peritoneal macrophage transcriptome. (**N**) Boxplot of phagocytosis of peritoneal macrophages in WT and *Esr1* KO mice (n = 15 for WT, n = 13 for *Esr1* KO; animals from 4 independent cohorts). (**O**) Boxplot of glycolysis quantification of peritoneal macrophages in WT and Esr1 KO mice (n = 15 for WT and *Esr1* KO; animals from 4 independent cohorts). For boxplots in panels (**D**, **E**, **I**, **J**, **N**, **O**), circles/squares represent NIA/JAX mice, respectively. Significance in non-parametric two-sided Wilcoxon rank-sum tests were reported. The center line represents the sample median, the box limits consist of the 25th and 75th percentiles, and the whiskers span 1.5x the interquartile range.

Figure 6. A mini screen for candidate transcription factors driving female-specific macrophage 'omic' and functional remodeling with aging.

(**A**) Flow chart outlining the steps for the selection of candidate transcription factors (TFs) for screening. (**B**) Heatmap displaying female-specific differential transcription factor gene expression with aging (FDR < 5% in aging female macrophages, FDR > 10% in aging male macrophages based on DESeq2 analysis). (**C**) Selected enriched motifs identified at female-specific differentially accessible ATAC-seq peaks with aging (HOMER; FDR < 5%). (**D**) Selected enriched motifs identified at female-specific differentially marked H3K4me3 peaks with aging (HOMER; FDR < 5%). (**E**) Experimental scheme of shRNA-mediated TF knockdown in RAW264.7 macrophages. (**F**) GSEA of TF shRNA knockdown regulated genes in the aging female peritoneal macrophage transcriptome. (**G**, **H**, **I**) Boxplots showing phagocytosis quantification using flow cytometry (**G**), glycolysis quantification using Agilent Seahorse assays (**H**), and lactate levels measured with Lactate-Glo in RAW264.7 macrophages transduced with lentiviral TF shRNA against (**I**) *Irf2*, *Mef2c*, *Meis1*, *Tal1*, and *Tbl1xr1* (n = 6 independent infections for each hairpin). Dark green/light green for sh1/sh2 samples. Significance in non-parametric one-sided Wilcoxon rank-sum tests were reported (Hypothesis: same direction as aging). The horizontal red line in the panel shows the median control value in the relative phagocytosis index (**G**), relative glycolysis (**H**), and relative lactate secretion (**I**) of macrophages. The center line represents the sample median, the box limits show the 25th and 75th percentiles, and the whiskers span 1.5 times the interquartile range.

Figure 7. Age-related decrease in Irf2 expression impacts Hk3 expression, leading to increased glycolytic reliance.

(**A**) Analysis of Irf2 expression at the RNA and protein levels in aging peritoneal macrophages. (**B**) Boxplot of *Irf2* gene expression in mouse peritoneal macrophages using RT-qPCR (young female n = 12, old female n = 8, young male n = 12, and old male n = 9; animals from 4 independent cohorts). (**C**) Histogram of female and male Irf2 protein expression between young and old peritoneal macrophages based on intracellular immunolabelling and flow cytometry quantification. (**D**) Boxplot of Irf2 protein quantification in peritoneal macrophages between young and old female and male mice (young female n = 13, old female n = 14, young male n = 14, and old male n = 13; animals from 3 independent cohorts). (**E**) Experimental scheme for Irf2 ChIP-seq in young female BMDMs. (**F**) Top GREAT enriched terms of Irf2-bound genomic regions. **(G)** GSEA of direct Irf2 target genes in the aging female peritoneal macrophage transcriptome. Peaks were assigned to target genes based on their absolute distance to transcriptional start sites (500bp-5kb). (**H**) Integrated Genomics Viewer (IGV) snapshot of Irf2 ChIP-seq signal at the *Hk3* gene locus on chromosome 13. (**I**) Quantitative RT-qPCR analysis of *Hk3* mRNA levels in young and old female peritoneal macrophages samples (n = 12 young, n = 8 old female; animals from 4 independent cohorts). (**J**) Experimental design for lentiviral knockdown of *Irf2* in J774A.1 cells. (**K**) Boxplot of *Hk3* expression from RNA-seq after knockdown of *Irf2* in macrophage cells. Circles/squares for RAW264.7/J774A.1 samples; shLuciferase (goldenrod), non-targeting control (light goldenrod), sh1 (dark green), and sh2 (light green); n = 3 infections per hairpin. Significance as FDR from DESeq2. (**L**) Boxplot of glycolysis quantification using Seahorse assays on lentiviral knockdown of *Irf2* RAW264.7 and J774A.1 cell line (n = 6 infections per hairpin). Note that the RAW264.7 data is repeated from **Figure 6I** for comparison convenience. (**M**) Boxplot of glycolysis quantification using Lactate-Glo on lentiviral knockdown *Irf2* in RAW264.7 and J774A.1 cells (n = 6 infections per hairpin). Note that the RAW264.7 data is repeated from **Figure 6J** for comparison convenience. (**N**) Proposed mechanism for Irf2-driven age-related glycolytic shift in aging female peritoneal macrophages. For boxplots in panels (**B**, **D**, **I)**, circles/squares represent NIA/JAX mice, respectively. Significance in non-parametric two-sided Wilcoxon rank-sum tests is reported. For boxplots in panels (**L**, **M**) circles/squares for RAW264.7/J774A.1 samples; dark green/light green for sh1/sh2 samples. Significance in non-parametric one-sided Wilcoxon rank-sum tests

were reported (Hypothesis: same regulation direction as aging). The horizontal red line in the panel shows the median control value of the normalized glycolysis (**L**) and normalized lactate (**M**).

Figure 1

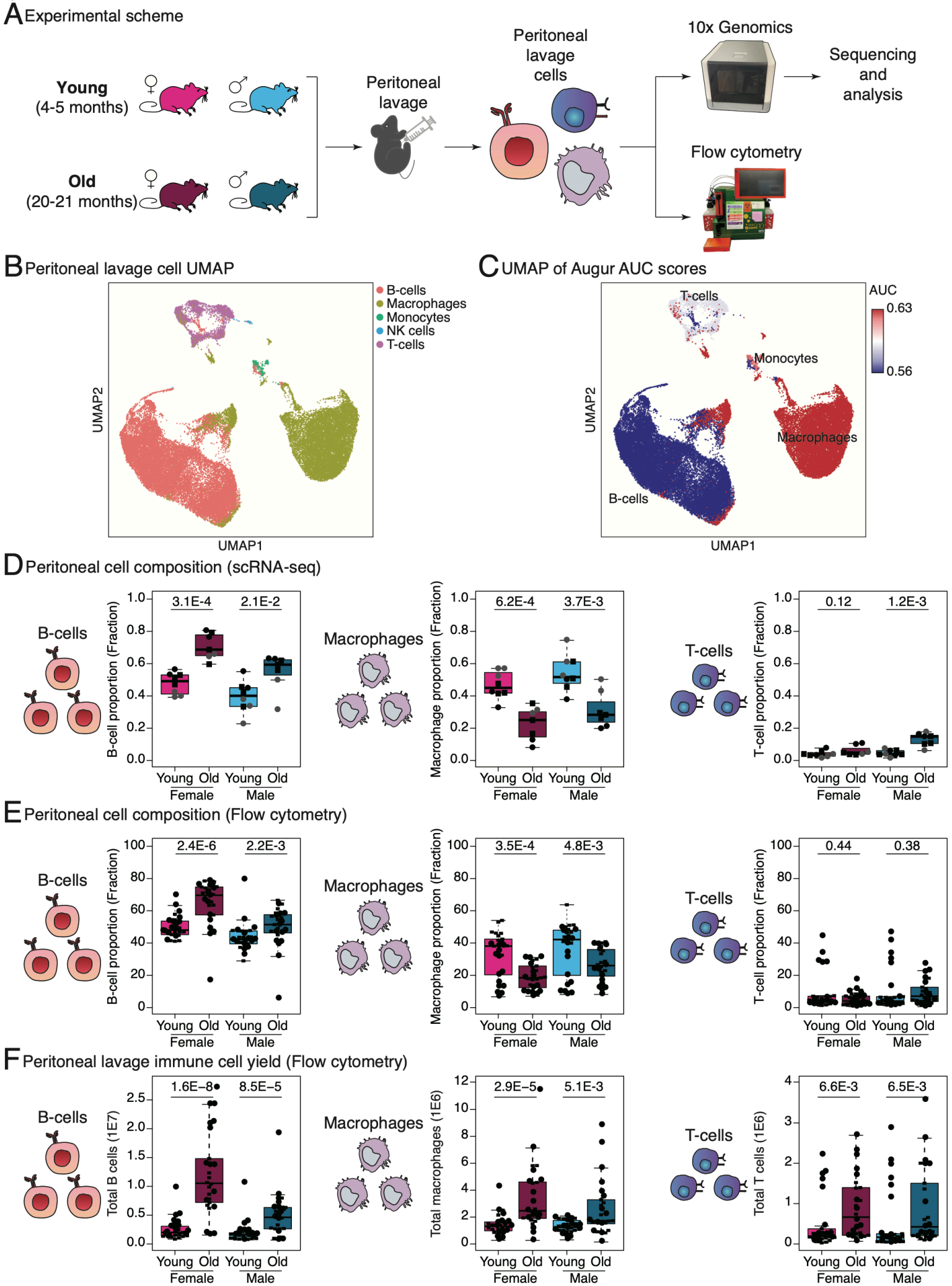
A Experimental scheme
Young
(4-5 months)
Old
(20-21 months)
Peritoneal lavage
Peritoneal lavage cells
10x Genomics
Sequencing and analysis
Flow cytometry
B Peritoneal lavage cell UMAP
B-cells
Macrophages
Monocytes
NK cells
T-cells
UMAP2
UMAP1
C UMAP of Augur AUC scores
AUC
0.63
0.56
T-cells
Monocytes
Macrophages
B-cells
D Peritoneal cell composition (scRNA-seq)
B-cells
B-cell proportion (Fraction)
3.1E-4
2.1E-2
Macrophages
Macrophage proportion (Fraction)
6.2E-4
3.7E-3
T-cells
T-cell proportion (Fraction)
0.12
1.2E-3
Young Old Young Old
Female Male
E Peritoneal cell composition (Flow cytometry)
2.4E-6
2.2E-3
3.5E-4
4.8E-3
0.44
0.38
F Peritoneal lavage immune cell yield (Flow cytometry)
Total B cells (1E7)
1.6E−8
8.5E−5
Total macrophages (1E6)
2.9E−5
5.1E-3
Total T cells (1E6)
6.6E-3
6.5E-3

Figure 2

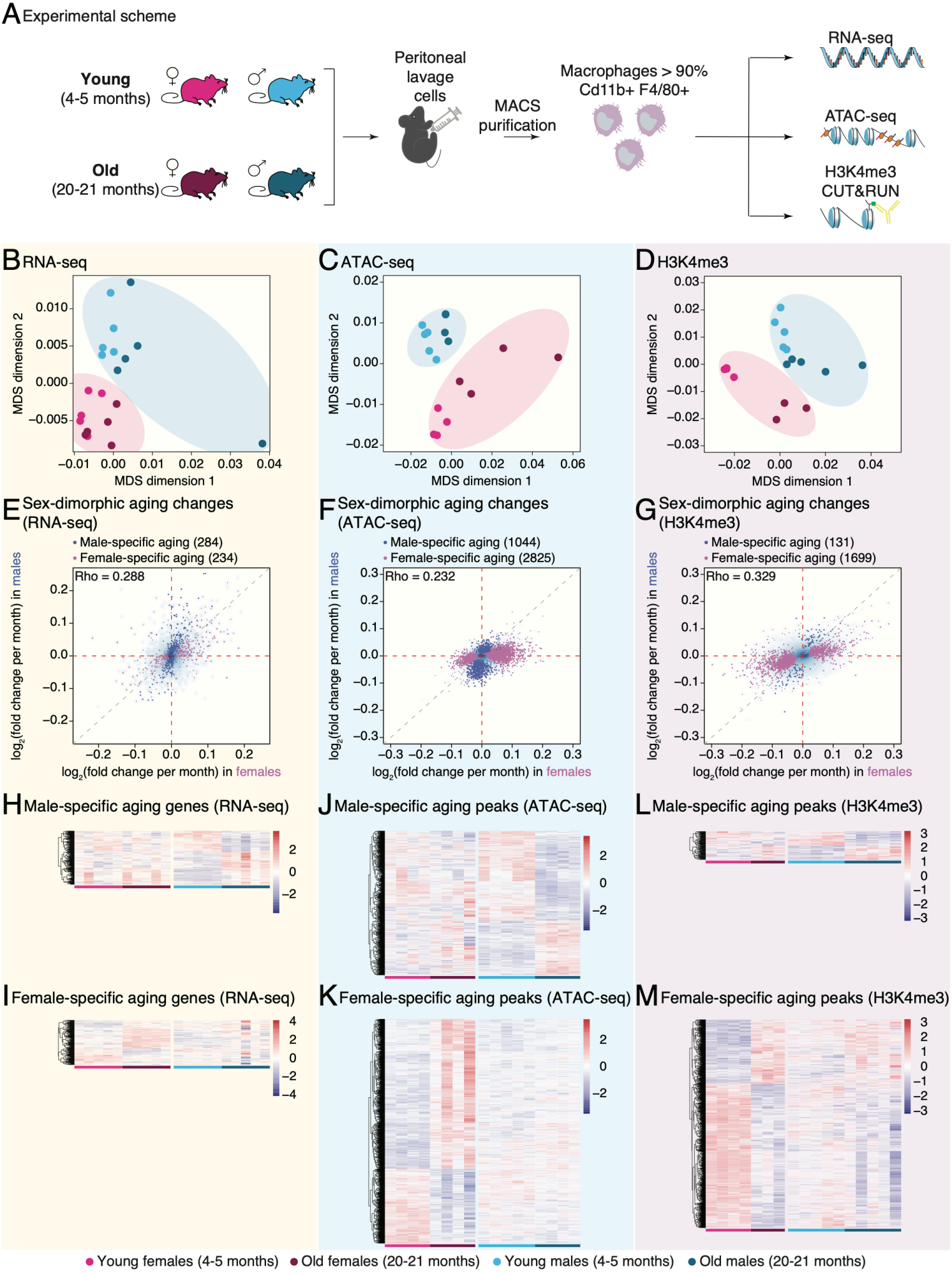
A Experimental scheme
Young
(4-5 months)
Old
(20-21 months)
Peritoneal lavage cells
MACS purification
Macrophages > 90%
Cd11b+ F4/80+
RNA-seq
ATAC-seq
H3K4me3 CUT&RUN
B RNA-seq
C ATAC-seq
D H3K4me3
MDS dimension 1
MDS dimension 2
E Sex-dimorphic aging changes (RNA-seq)
Male-specific aging (284)
Female-specific aging (234)
Rho = 0.288
F Sex-dimorphic aging changes (ATAC-seq)
Male-specific aging (1044)
Female-specific aging (2825)
Rho = 0.232
G Sex-dimorphic aging changes (H3K4me3)
Male-specific aging (131)
Female-specific aging (1699)
Rho = 0.329
log2(fold change per month) in males
log2(fold change per month) in females
H Male-specific aging genes (RNA-seq)
I Female-specific aging genes (RNA-seq)
J Male-specific aging peaks (ATAC-seq)
K Female-specific aging peaks (ATAC-seq)
L Male-specific aging peaks (H3K4me3)
M Female-specific aging peaks (H3K4me3)
Young females (4-5 months)
Old females (20-21 months)
Young males (4-5 months)
Old males (20-21 months)

Figure 3

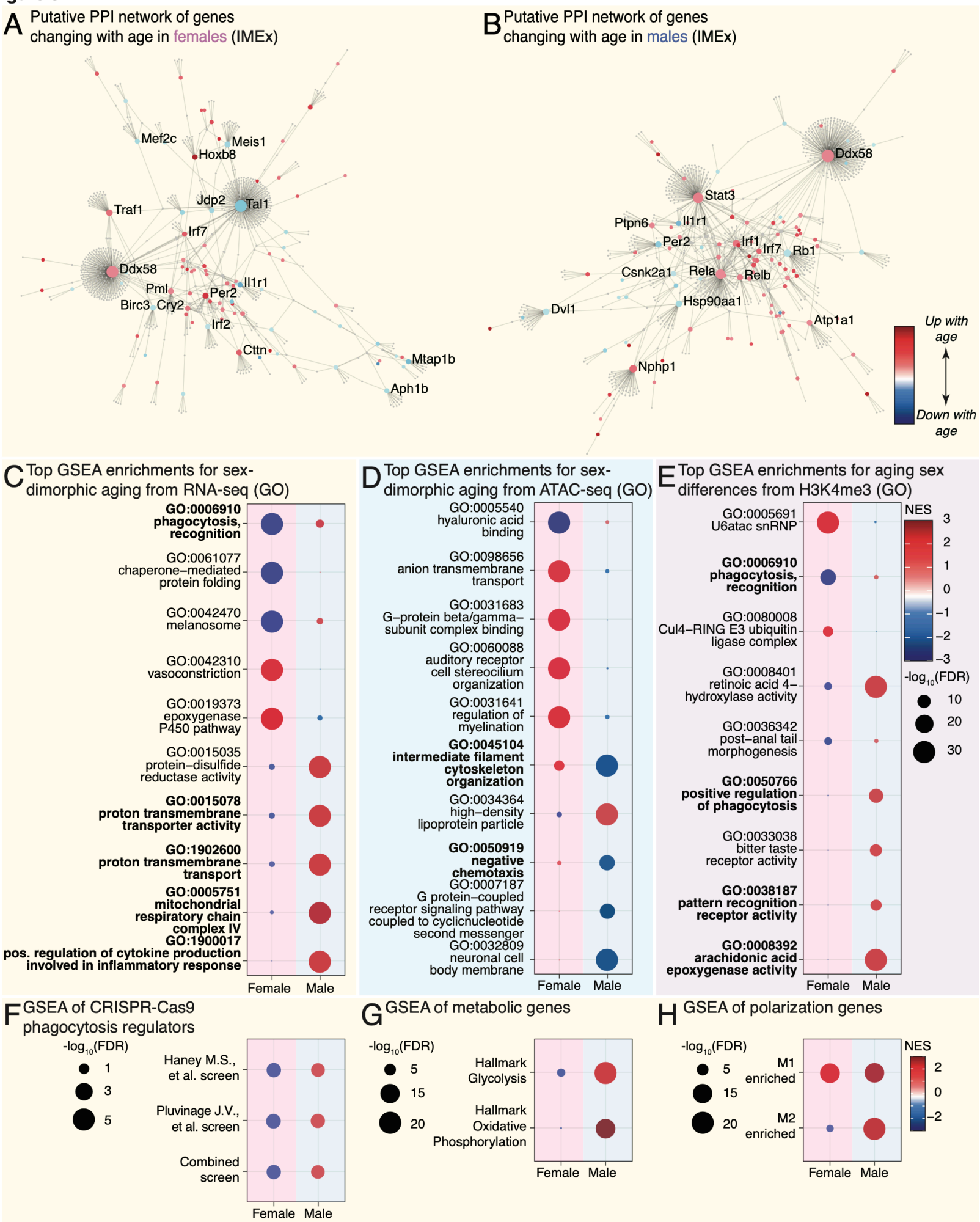
A Putative PPI network of genes changing with age in females (IMEx)
Mef2c
Meis1
Hoxb8
Traf1
Jdp2
Tal1
Irf7
Ddx58
Pml
Il1r1
Per2
Birc3
Cry2
Irf2
Cttn
Mtap1b
Aph1b
B Putative PPI network of genes changing with age in males (IMEx)
Ddx58
Stat3
Ptpn6
Il1r1
Per2
Irf1
Irf7
Rb1
Csnk2a1
Rela
Relb
Hsp90aa1
Dvl1
Atp1a1
Nphp1
Up with age
Down with age
C Top GSEA enrichments for sex-dimorphic aging from RNA-seq (GO)
GO:0006910 phagocytosis, recognition
GO:0061077 chaperone–mediated protein folding
GO:0042470 melanosome
GO:0042310 vasoconstriction
GO:0019373 epoxygenase P450 pathway
GO:0015035 protein–disulfide reductase activity
GO:0015078 proton transmembrane transporter activity
GO:1902600 proton transmembrane transport
GO:0005751 mitochondrial respiratory chain complex IV
GO:1900017 pos. regulation of cytokine production involved in inflammatory response
Female
Male
D Top GSEA enrichments for sex-dimorphic aging from ATAC-seq (GO)
GO:0005540 hyaluronic acid binding
GO:0098656 anion transmembrane transport
GO:0031683 G–protein beta/gamma–subunit complex binding
GO:0060088 auditory receptor cell stereocilium organization
GO:0031641 regulation of myelination
GO:0045104 intermediate filament cytoskeleton organization
GO:0034364 high–density lipoprotein particle
GO:0050919 negative chemotaxis
GO:0007187 G protein–coupled receptor signaling pathway coupled to cyclicnucleotide second messenger
GO:0032809 neuronal cell body membrane
Female
Male
E Top GSEA enrichments for aging sex differences from H3K4me3 (GO)
GO:0005691 U6atac snRNP
GO:0006910 phagocytosis, recognition
GO:0080008 Cul4–RING E3 ubiquitin ligase complex
GO:0008401 retinoic acid 4–hydroxylase activity
GO:0036342 post–anal tail morphogenesis
GO:0050766 positive regulation of phagocytosis
GO:0033038 bitter taste receptor activity
GO:0038187 pattern recognition receptor activity
GO:0008392 arachidonic acid epoxygenase activity
Female
Male
NES
3
2
1
0
−1
−2
−3
-log10(FDR)
10
20
30
F GSEA of CRISPR-Cas9 phagocytosis regulators
-log10(FDR)
1
3
5
Haney M.S., et al. screen
Pluvinage J.V., et al. screen
Combined screen
Female
Male
G GSEA of metabolic genes
-log10(FDR)
5
15
20
Hallmark Glycolysis
Hallmark Oxidative Phosphorylation
Female
Male
H GSEA of polarization genes
-log10(FDR)
5
15
20
M1 enriched
M2 enriched
NES
2
0
−2
Female
Male

Figure 4

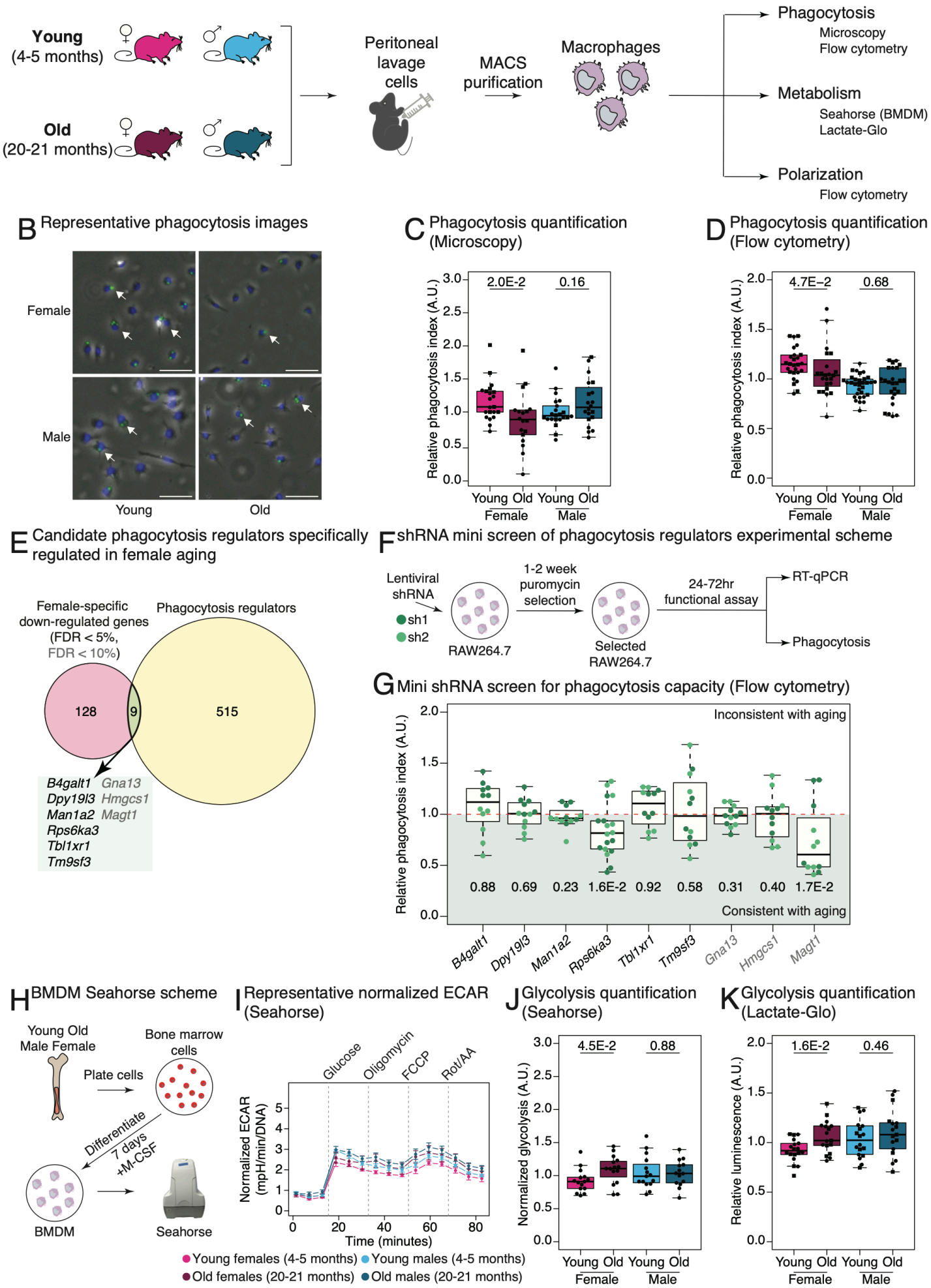
A Experimental scheme
Young
(4-5 months)
Old
(20-21 months)
Peritoneal lavage cells
MACS purification
Macrophages
Phagocytosis
Microscopy
Flow cytometry
Metabolism
Seahorse (BMDM)
Lactate-Glo
Polarization
Flow cytometry
B Representative phagocytosis images
Female
Male
Young
Old
C Phagocytosis quantification (Microscopy)
Relative phagocytosis index (A.U.)
2.0E-2
0.16
Young Old Young Old
Female Male
D Phagocytosis quantification (Flow cytometry)
4.7E−2
0.68
E Candidate phagocytosis regulators specifically regulated in female aging
Female-specific down-regulated genes (FDR < 5%, FDR < 10%)
Phagocytosis regulators
128
9
515
B4galt1 Gna13
Dpy19l3 Hmgcs1
Man1a2 Magt1
Rps6ka3
Tbl1xr1
Tm9sf3
F shRNA mini screen of phagocytosis regulators experimental scheme
Lentiviral shRNA
sh1
sh2
RAW264.7
1-2 week puromycin selection
Selected RAW264.7
24-72hr functional assay
RT-qPCR
Phagocytosis
G Mini shRNA screen for phagocytosis capacity (Flow cytometry)
Inconsistent with aging
Consistent with aging
0.88 0.69 0.23 1.6E-2 0.92 0.58 0.31 0.40 1.7E-2
B4galt1 Dpy19l3 Man1a2 Rps6ka3 Tbl1xr1 Tm9sf3 Gna13 Hmgcs1 Magt1
H BMDM Seahorse scheme
Young Old
Male Female
Bone marrow cells
Plate cells
Differentiate
7 days
+M-CSF
BMDM
Seahorse
I Representative normalized ECAR (Seahorse)
Glucose
Oligomycin
FCCP
Rot/AA
Normalized ECAR (mpH/min/DNA)
Time (minutes)
Young females (4-5 months)
Young males (4-5 months)
Old females (20-21 months)
Old males (20-21 months)
J Glycolysis quantification (Seahorse)
Normalized glycolysis (A.U.)
4.5E-2
0.88
K Glycolysis quantification (Lactate-Glo)
Relative luminescence (A.U.)
1.6E-2
0.46

Figure 5

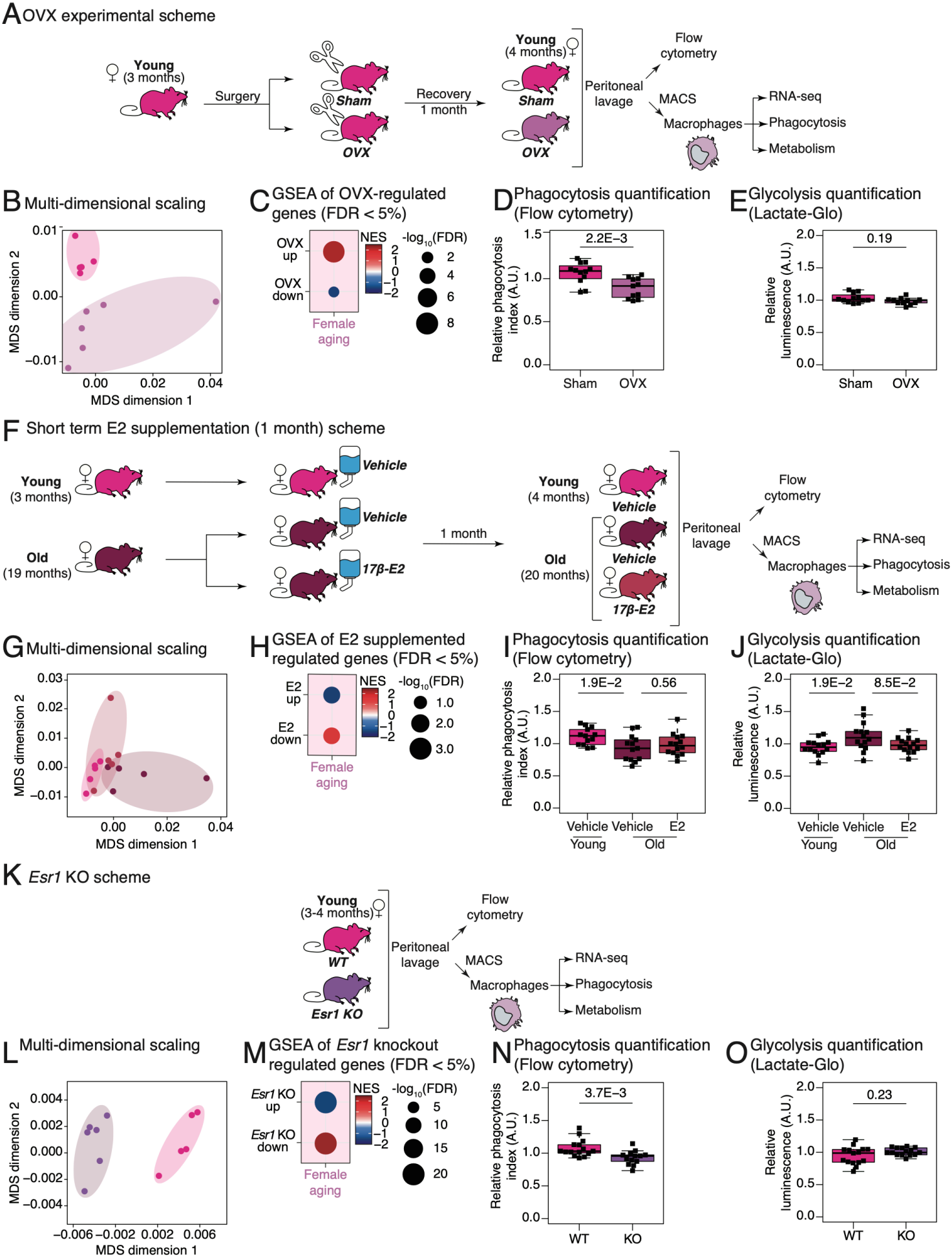
A OVX experimental scheme
Young (3 months)
Surgery
Sham
OVX
Recovery 1 month
Young (4 months)
Sham
OVX
Peritoneal lavage
Flow cytometry
MACS
Macrophages
RNA-seq
Phagocytosis
Metabolism
B Multi-dimensional scaling
MDS dimension 2
MDS dimension 1
C GSEA of OVX-regulated genes (FDR < 5%)
OVX up
OVX down
Female aging
NES
-log10(FDR)
D Phagocytosis quantification (Flow cytometry)
Relative phagocytosis index (A.U.)
2.2E−3
Sham
OVX
E Glycolysis quantification (Lactate-Glo)
Relative luminescence (A.U.)
0.19
Sham
OVX
F Short term E2 supplementation (1 month) scheme
Young (3 months)
Old (19 months)
Vehicle
Vehicle
17β-E2
1 month
Young (4 months)
Old (20 months)
Vehicle
Vehicle
17β-E2
Peritoneal lavage
Flow cytometry
MACS
Macrophages
RNA-seq
Phagocytosis
Metabolism
G Multi-dimensional scaling
MDS dimension 2
MDS dimension 1
H GSEA of E2 supplemented regulated genes (FDR < 5%)
E2 up
E2 down
Female aging
NES
-log10(FDR)
I Phagocytosis quantification (Flow cytometry)
Relative phagocytosis index (A.U.)
1.9E−2
0.56
Vehicle Vehicle E2
Young Old
J Glycolysis quantification (Lactate-Glo)
Relative luminescence (A.U.)
1.9E−2
8.5E−2
Vehicle Vehicle E2
Young Old
K Esr1 KO scheme
Young (3-4 months)
WT
Esr1 KO
Peritoneal lavage
Flow cytometry
MACS
Macrophages
RNA-seq
Phagocytosis
Metabolism
L Multi-dimensional scaling
MDS dimension 2
MDS dimension 1
M GSEA of Esr1 knockout regulated genes (FDR < 5%)
Esr1 KO up
Esr1 KO down
Female aging
NES
-log10(FDR)
N Phagocytosis quantification (Flow cytometry)
Relative phagocytosis index (A.U.)
3.7E−3
WT
KO
O Glycolysis quantification (Lactate-Glo)
Relative luminescence (A.U.)
0.23
WT
KO

Figure 6

A Flowchart for identifying transcription factors (TFs) for screening

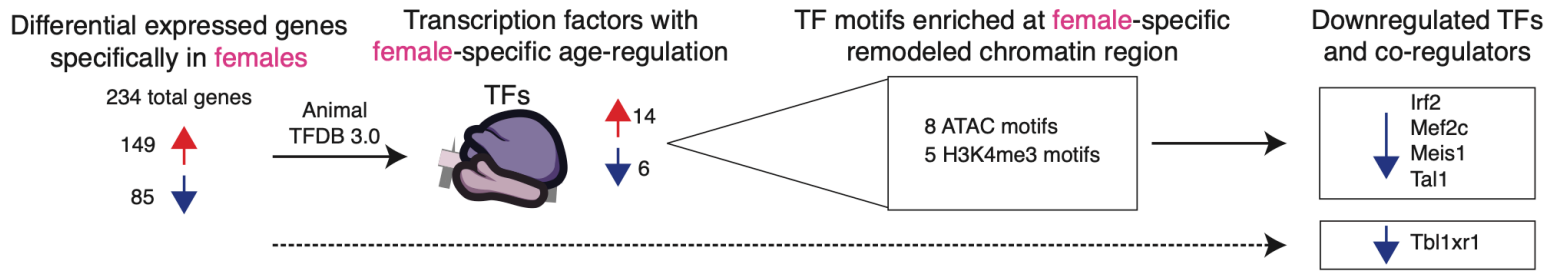

B Female-specific differential TFs gene expression with aging

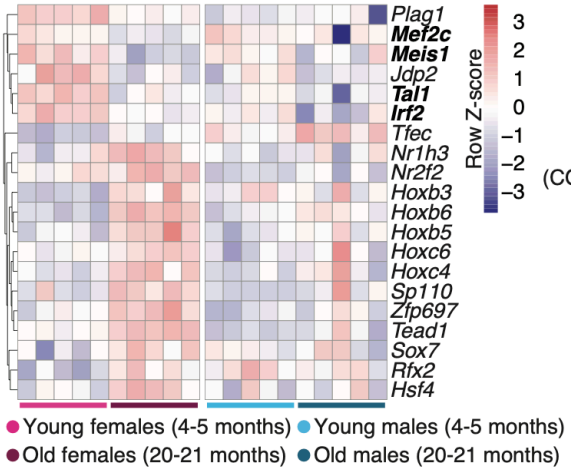

C Selected enriched motifs at female-specific differential ATAC peaks with aging (FDR < 5%)

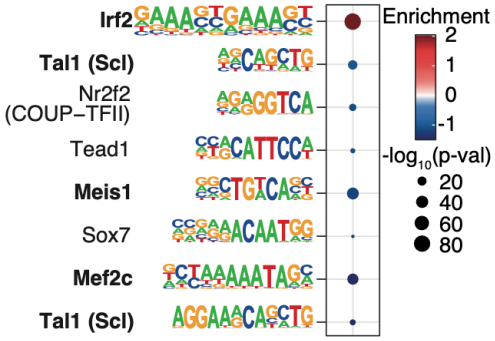

D Selected enriched motifs at female-specific differential H3K4me3 peaks with aging (FDR < 5%)

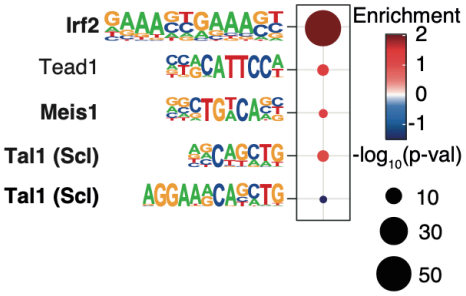

E shRNA mini screen for candidate TF regulators

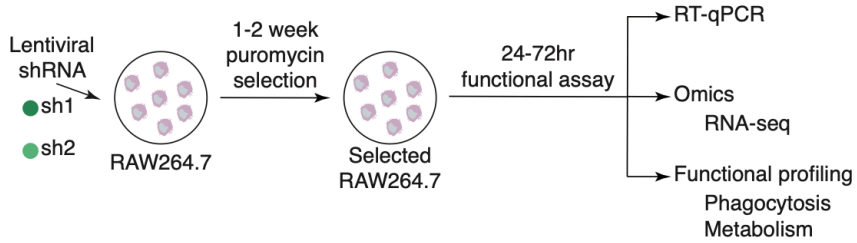

F GSEA of shRNA knockdown compared to female aging

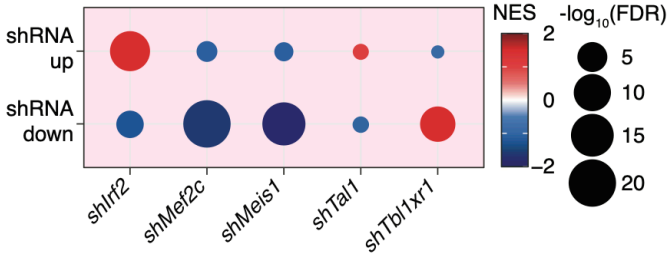

G Phagocytosis quantification (Flow cytometry)

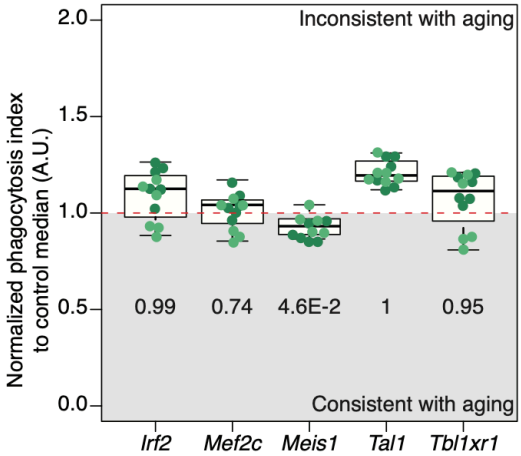

H Glycolysis quantification (Seahorse)

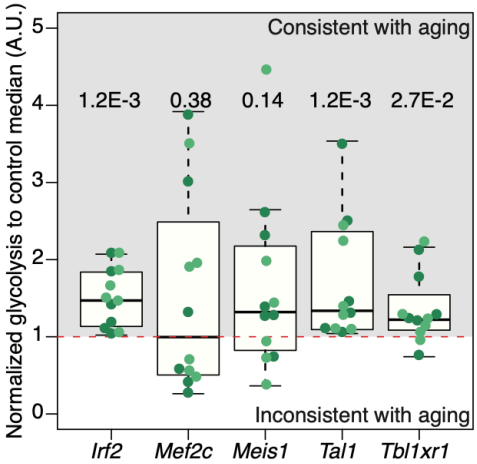

I Glycolysis quantification (Lactate-Glo)

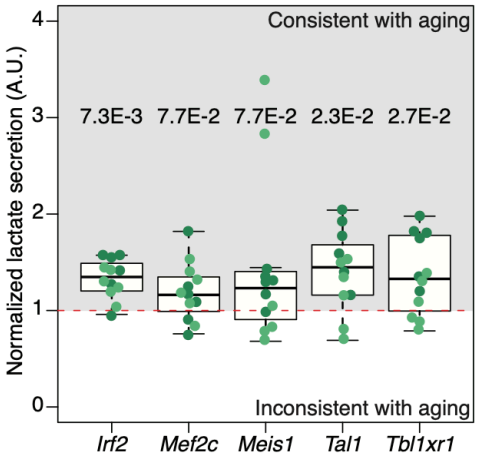

Figure 7

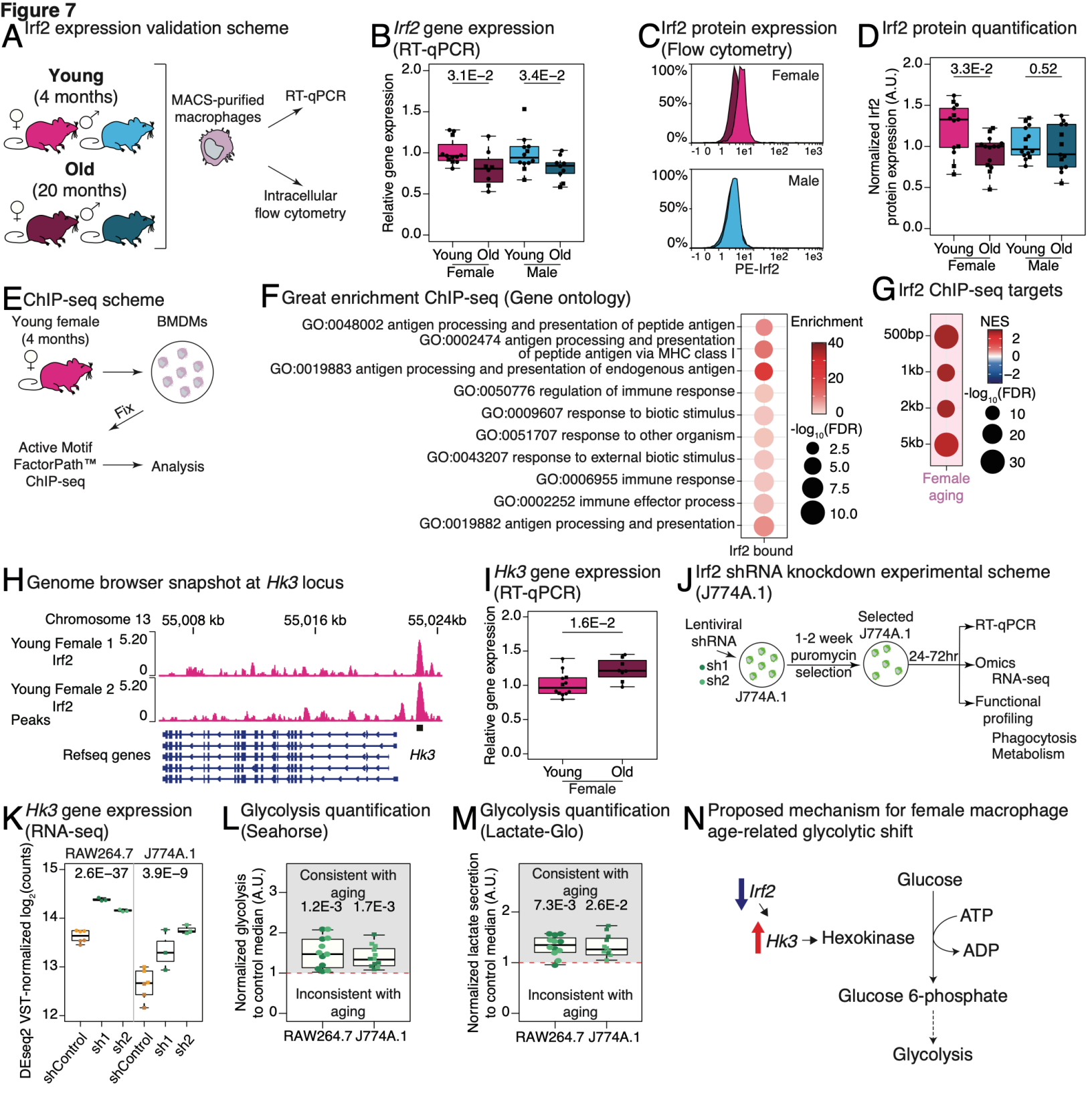
A Irf2 expression validation scheme
Young
(4 months)
Old
(20 months)
MACS-purified macrophages
RT-qPCR
Intracellular flow cytometry
B Irf2 gene expression (RT-qPCR)
Relative gene expression
3.1E−2
3.4E−2
Young Old Young Old
Female Male
C Irf2 protein expression (Flow cytometry)
Female
Male
PE-Irf2
D Irf2 protein quantification
Normalized Irf2 protein expression (A.U.)
3.3E-2
0.52
Young Old Young Old
Female Male
E ChIP-seq scheme
Young female (4 months)
BMDMs
Fix
Active Motif FactorPath™ ChIP-seq
Analysis
F Great enrichment ChIP-seq (Gene ontology)
GO:0048002 antigen processing and presentation of peptide antigen
GO:0002474 antigen processing and presentation of peptide antigen via MHC class I
GO:0019883 antigen processing and presentation of endogenous antigen
GO:0050776 regulation of immune response
GO:0009607 response to biotic stimulus
GO:0051707 response to other organism
GO:0043207 response to external biotic stimulus
GO:0006955 immune response
GO:0002252 immune effector process
GO:0019882 antigen processing and presentation
Irf2 bound
Enrichment
-log10(FDR)
G Irf2 ChIP-seq targets
500bp
1kb
2kb
5kb
Female aging
NES
-log10(FDR)
H Genome browser snapshot at Hk3 locus
Chromosome 13
55,008 kb
55,016 kb
55,024kb
Young Female 1 Irf2
Young Female 2 Irf2
Peaks
Refseq genes
Hk3
I Hk3 gene expression (RT-qPCR)
Relative gene expression
1.6E−2
Young Old
Female
J Irf2 shRNA knockdown experimental scheme (J774A.1)
Lentiviral shRNA
sh1
sh2
J774A.1
1-2 week puromycin selection
Selected J774A.1
24-72hr
RT-qPCR
Omics
RNA-seq
Functional profiling
Phagocytosis
Metabolism
K Hk3 gene expression (RNA-seq)
RAW264.7
J774A.1
2.6E−37
3.9E−9
DEseq2 VST-normalized log2(counts)
shControl
sh1
sh2
L Glycolysis quantification (Seahorse)
Normalized glycolysis to control median (A.U.)
Consistent with aging
1.2E-3
1.7E-3
Inconsistent with aging
RAW264.7 J774A.1
M Glycolysis quantification (Lactate-Glo)
Normalized lactate secretion to control median (A.U.)
Consistent with aging
7.3E-3
2.6E-2
Inconsistent with aging
RAW264.7 J774A.1
N Proposed mechanism for female macrophage age-related glycolytic shift
Irf2
Hk3
Hexokinase
Glucose
ATP
ADP
Glucose 6-phosphate
Glycolysis